

**Single-charge transport
in coupled nanostructures**

Single-charge transport in coupled nanostructures

Proefschrift

ter verkrijging van de graad van doctor
aan de Technische Universiteit Delft,
op gezag van de Rector Magnificus prof.ir. K.F. Wakker,
voorzitter van het College voor Promoties,
in het openbaar te verdedigen op dinsdag 25 september 2001 om 16.00 uur

door

Cornelis Pieter HEIJ

natuurkundig ingenieur
geboren te Amsterdam.

Dit proefschrift is goedgekeurd door de promotor:

Prof.dr.ir. J.E. Mooij

Toegevoegd promotor:

Dr. P. Hadley

Samenstelling promotiecommissie:

Rector Magnificus	voorzitter
Prof.dr.ir. J. E. Mooij	Technische Universiteit Delft, promotor
Dr. P. Hadley	Technische Universiteit Delft, toegevoegd promotor
Prof.dr.ir. G. E. W. Bauer	Technische Universiteit Delft
Prof.dr. K. K. Likharev	SUNY Stony Brook, Verenigde Staten
Prof.dr. T. P. Orlando	Massachusetts Institute of Technology, Verenigde Staten
Prof.dr. M. Tinkham	Harvard University, Verenigde Staten
Dr. M. H. Devoret	C.E.A. Saclay, Frankrijk

Published and distributed by: DUP Science

Dup Science is an imprint of

Delft University Press

P.O. Box 98

2600 MG Delft

The Netherlands

Telephone: +31 15 2785678

Telefax: +31 15 2785706

E-mail: DUP@Library.TUdelft.NL

ISBN 90-407-2217-X

Keywords: Single-electron devices, Josephson effect

Copyright © 2001 by Pieter Heij

Cover: Paul Gerretsen and Pieter Heij

All rights reserved. No part of the material protected by this copyright notice may be reproduced or utilized in any form or by any means, electronic or mechanical, including photocopying, recording or by any information storage and retrieval system, without permission from the publisher: Delft University Press.

Printed in the Netherlands

Preface

This thesis describes the result of four years of research started in August 1997. The motivation for this research were the continuing developments in the area of single-electron devices. In these very small devices the presence or absence of a single electron can regulate the flow of billions of other electrons, yielding devices like the single-electron transistor. The fabrication of more complex circuits with more than one single-electron device required the use of multi-level fabrication techniques. The effort to make these multi-level circuits had already been started at that time, but the techniques were not mature and had to be perfected. Essentially, the multi-level fabrication is required to make a strong capacitive coupling between two different circuit components. Previously, SiO had been used as an insulator to make parallel plate capacitors. As a start we used this technique to make a single-electron switch as described in chapter 2. The use of SiO has a number of crucial disadvantages, that urged us to look for alternatives. Although a very thin layer of aluminum oxide was used to make a crucial component of single-electron devices, the tunnel junction, its use as a truly insulating layer had not been explored. A new oxidation technique was successfully developed to make aluminum oxide layers thicker than the natural oxide thickness of a few nanometers. The samples described in chapters 3-7 are fabricated with this new technique. Instead of merely using this technique to couple single-electron circuits, the last $1\frac{1}{2}$ years of the research we focussed on the development of an on-chip micro-wave generator, coupled to a detector with the same technique. Chapters 6 and 7 describe the design and the performance of this generator.

Completing this thesis would not have been possible without the help of numerous people. First I would like to thank Hans Mooij and Peter Hadley for supervising my PhD work. Within the Quantum Transport group Hans Mooij has been able to create a research environment where everything is possible and money plays no role. The numerous discussions with Peter Hadley were very useful, usually ending with the classical versus quantum mechanics controversy. I really enjoyed working together with all the other people that stayed and worked

in our group over the last four years. I'd specially like to mention my colleagues Michael '6c' Janus, Caspar van der Wal, Alexander ter Haar, Kees Harmans, Jorg Jansen, Wilfred van der Wiel, Onno Mantel, Silvano de Fransushi and David Dixon. My two graduation students, Wessel de Haas and Ewout Eijkelenboom, have both been working in the group for more than a year and did excellent work. Wessel made the best out of his project, the development of the rf-SET, and the results of Ewout's work can be read in the last two chapters. The technical squad, Bram van der Enden, Leo Lander, Mascha van Oossanen, Leo Dam and Raymond Schouten keep the group alive with their (electro)technical skills.

Furthermore I specially want to thank: Herre van der Zant, numerous ferocious battles on the squash and tennis court gave me a welcome distraction from the work in the group. Hannes 'Stöckli the swiss ski' Majer, who keeps on claiming that 1000 junctions are cooler than 2. My two 'paranimfen', Paul Gerretsen and Maarten van Tol, for assisting me on the scaffold. And last but not least my family and Karin, they always encouraged and supported me in doing this PhD, this thesis is yours too!

Pieter Heij

July 2001



Contents

1	Introduction	1
1.1	Single-electron tunnelling	1
1.2	The single-electron transistor	3
1.2.1	Normal state SET	3
1.2.2	Superconducting SET	5
1.3	Master equation simulations	6
1.4	The Josephson junction	8
1.5	The Cooper pair box	10
1.6	The Josephson quasiparticle cycle	12
1.7	Multi-layer fabrication	14
1.8	Thesis layout	16
	References	16
2	Negative differential resistance due to single-electron switching	19
2.1	Introduction	19
2.2	Experimental details	20
2.3	Experimental results	22
2.4	Conclusions	25
	References	25
3	A single-electron inverter	27
3.1	Introduction	27
3.2	Experimental details	28
3.3	Experimental results	30
3.3.1	Normal state	30
3.3.2	Superconducting state	34
3.4	Conclusions	36
	References	36

4	Charge spectrometry with a strongly coupled superconducting single-electron transistor	39
4.1	Introduction	39
4.2	Experimental details	40
4.3	Experimental results; the high-ohmic SSET	43
4.3.1	Master equation simulations	45
4.3.2	Simulation results	46
4.3.3	Operational constraints	48
4.4	Experimental results; the quantum SSET	51
4.5	Conclusions	54
4.6	Acknowledgements	54
	References	54
5	Superposition of charge states in a system of two capacitively coupled superconducting islands	57
5.1	Introduction	57
5.2	Experimental details	58
5.3	Experimental results	60
5.4	Conclusions	65
5.5	Acknowledgements	66
	References	66
6	Design and fabrication of an on-chip microwave generator and detector	69
6.1	Introduction	69
6.2	The Josephson generator	70
6.3	The Cooper pair box as microwave detector	72
6.4	General design considerations	73
6.5	A generator with nanosecond control	75
6.6	Sample fabrication	77
6.7	Measurement set-up	78
	References	79
7	An on-chip Josephson generator with nanosecond control	81
7.1	The SQUID as a microwave generator	82
7.2	The Cooper pair box as microwave detector	83
7.3	Nanosecond control of the SQUID	87
7.4	Discussion	91
7.5	Conclusions	92

References	92
Summary	93
Samenvatting	95
Curriculum Vitae	97
List of publications	99

Chapter 1

Introduction

The ongoing trend of making faster and more complex computer chips will eventually reach not only economical limits but also fundamental limits. The gate oxide of a transistor, for example, can currently be made as thin as 7 atomic layers [1]. Apart from the fact that it is incredibly difficult and expensive to make a homogeneous oxide layer of 1 atomic layer over a large chip area, the quantum mechanical tunnelling of electrons will ruin the insulating properties of such a thin layer. As components get smaller and smaller, the energy it takes to add a single electron to a component will also become non-negligible. This so-called charging energy is inversely proportional to the size of the component and will become important if the size of components shrinks to the nanometer level.

These single-electron effects can be used to make new devices. The single-electron transistor (SET), for example, exploits the interplay between tunnelling and charging effects [2]. These transistors can be routinely made using electron-beam lithography. SETs are usually investigated at very low temperatures, where most of their properties have been thoroughly studied. The most impressive characteristic is its extreme sensitivity ($8 \times 10^{-6} e/\sqrt{\text{Hz}}$ at 10 Hz) to charge [3]. To study strongly coupled single-electron devices, a multilayer technology is needed. The development of this technology and experiments performed on strongly coupled single-electron devices are described in this thesis.

1.1 Single-electron tunnelling

Two examples of single-electron devices are shown in Fig. 1.1. The small capacitance is achieved by fabricating a tiny isolated structure, called an island. To probe the charging effects on this island, leads are attached to the island through a thin insulating layer. If this layer is made thin enough (~ 1 nm), electrons can

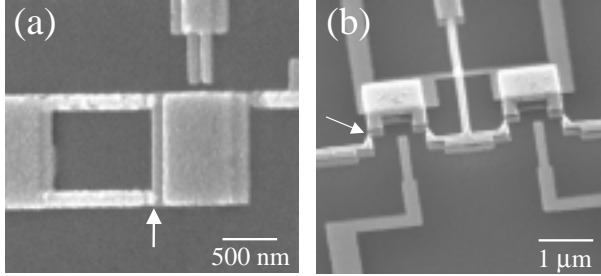


Figure 1.1: (a) Scanning Electron Microscope (SEM) picture of a single-electron transistor. (b) SEM picture of a single-electron inverter. The two different material layers show up as dark grey and light grey. The tunnel junctions are indicated by the arrows.

quantum mechanically tunnel through the insulating layer and a tunnel current can flow. This tunnel element is called a tunnel junction. In general, the tunnel rate depends on the free energy difference before and after tunnelling. If zero-dimensional states are absent on the island and when the leads are metallic, the tunnel rate can be expressed as [4]

$$\Gamma = \frac{\Delta F}{e^2 R} \frac{1}{e^{\Delta F/k_B T} - 1}, \quad (1.1)$$

where ΔF is the change in free energy of the system for a tunnel event, R is the resistance of tunnel junction and T is the temperature. According to this equation, at zero temperature the tunnel rate is zero for $\Delta F > 0$, and increases linearly for $\Delta F < 0$.

When one of the leads or the island are non-metallic, one has to use the more general quantum-mechanical Golden Rule to calculate the rates

$$\Gamma_{1 \rightarrow 2}(\Delta F) = \frac{2\pi}{\hbar} \int_{-\infty}^{\infty} |t_{12}|^2 \rho_1(E-F_1) f(E-F_1) \rho_2(E-F_2) [1-f(E-F_2)] dE, \quad (1.2)$$

where t_{12} is the energy dependent tunnel matrix element, $\rho_{1,2}$ is the density of states of the conductor on the left (1) or right (2) side of the tunnel junction, f is the Fermi function and $F_{1,2}$ is the free energy of the system.

If the leads or the island become superconducting, the electrons will form a condensate and combine into Cooper pairs. In the superconducting density of states a gap Δ opens up at the Fermi energy and integral 1.2 has to be solved numerically [5]. The numerical solution at zero temperature shows that $\Gamma = 0$

for $\Delta F > -2\Delta$. At $\Delta F = -2\Delta$ the rate jumps to $0.78 \frac{2\Delta}{e^2 R}$ and for smaller ΔF it asymptotically increases towards $\Gamma = -\frac{\Delta F}{e^2 R}$. For $T > 0$, the tunnel rates are small but non-zero for $\Delta F > -2\Delta$.

1.2 The single-electron transistor

A single-electron transistor (SET) consists of a small metallic island connected to two leads by tunnel junctions. A third lead or gate is capacitively connected to the island (see Fig. 1.2a). The charge on the island is quantized in units of e if the following requirements are met: the charging energy $E_C = \frac{e^2}{2C_\Sigma}$ should be much larger than the thermal energy $k_B T$, and the junction resistance should be larger than the quantum resistance $\frac{h}{e^2} = 25.8 \text{k}\Omega$. First we will discuss the normal state SET, where the leads and the island are metallic, second the all superconducting case.

1.2.1 Normal state SET

If the bias voltage over the SET is sufficiently small, $|V_1 - V_2| < \frac{e}{2C_\Sigma}$, where $C_\Sigma = C_1 + C_2 + C_g + C_0$, the conductance of the SET is zero. This so-called

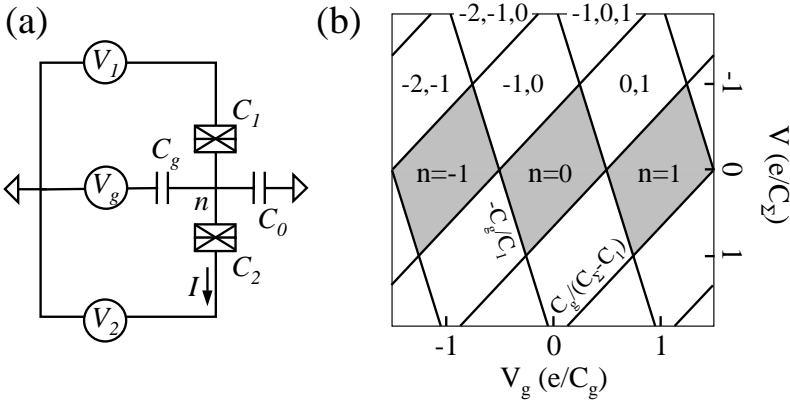


Figure 1.2: (a) Schematic of a single-electron transistor where n is the number of excess electrons on the island and C_0 is the stray capacitance to ground. (b) Schematic of a stability diagram. The regions where various charge states are stable are marked by the solid lines. Due to the Coulomb blockade, the current is zero in the shaded areas at temperatures $k_B T \ll E_C$. In experiments the slope of the solid lines is used to determine sample capacitances.

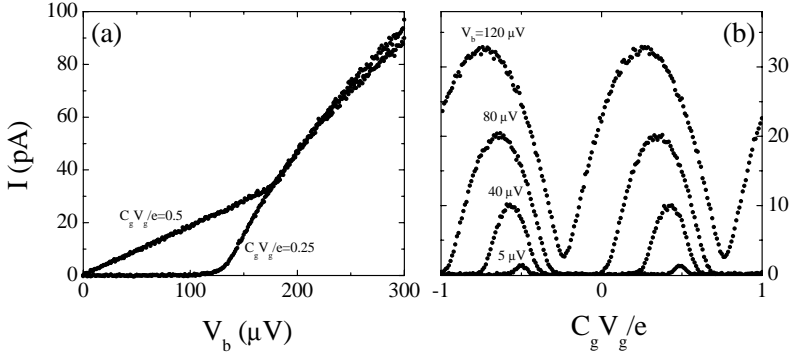


Figure 1.3: (a) Current voltage characteristics for two different gate values for a sample with $E_C = 130 \mu\text{eV}$. (b) Coulomb oscillations of the current versus the gate voltage.

Coulomb blockade can be lifted by tuning the potential V_g on the gate electrode. Figure 1.2b shows the stability diagram of a SET. The shaded areas show within which bias conditions the current is zero. The pattern is e -periodic in the induced gate charge. The slopes of the edges of the diamond-like structure depend on the capacitance values, and are usually used to determine these values. Inside the diamonds is shown which charge states are energetically accessible for that specific bias condition.

The current-voltage (IV) characteristic of a SET depends on the gate volt-

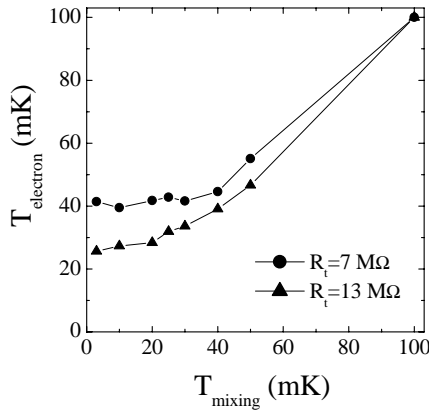


Figure 1.4: The effective electron temperature versus the bath temperature for two transistors with a different resistance.

age. Figure 1.3a shows the IV characteristics for two different gate values. The lower trace manifests the Coulomb blockade of tunnelling, while the blockade is suppressed in the upper trace. If the voltage bias is kept constant, the current versus the gate voltage shows Coulomb oscillations of the current. Figure 1.3b clearly shows the Coulomb oscillations for various bias voltages.

Because of the dissipating nature of tunnelling and because of non-ideal filtering, the effective temperature of the electrons on the island is different from the cryostat's base temperature. The effective electron temperature can be determined via the width of the Coulomb oscillations. For $eV \ll k_B T$ the full-width half maximum of the Coulomb peaks is linear with temperature. When the sample parameters are known, the effective electron temperature can be determined. Figure 1.4 shows the effective electron temperature versus the bath temperature for two SETs with a different resistance. The lowest electron temperature reached is 27 mK for a SET of 13 M Ω . In general, our samples showed the trend that the minimal effective electron temperature decreased for increasing sample resistance.

1.2.2 Superconducting SET

The superconducting SET (SSET) behaves similarly as a normal state SET, but electrons have to be excited above the superconducting gap. Because of the superconducting gap Δ , the charging effects are shifted by $2\Delta/e$ in voltage bias for each junction. Figure 1.5a shows two IV characteristics for different gate voltage. When the Coulomb blockade is lifted, current starts flowing at

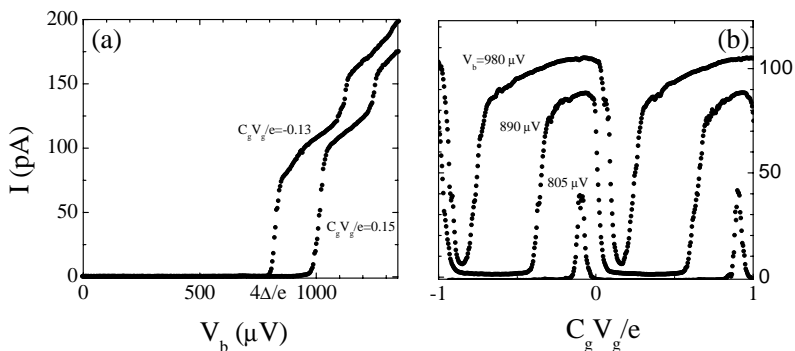


Figure 1.5: (a) IV characteristics of a superconducting SET with $E_C = 170 \mu\text{eV}$ for two different values of the gate voltage. The current is very small for $V < 4\Delta/e$. (b) Coulomb oscillations of the current for different bias voltages.

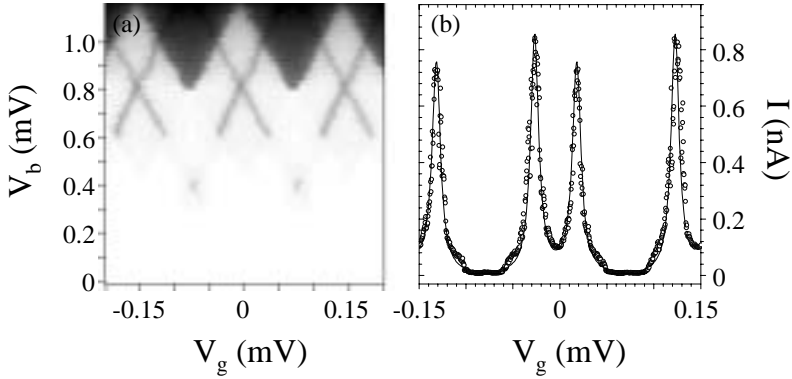


Figure 1.6: (a) The stability diagram of a superconducting SET in grayscale, where black indicates 3.1 nA. Clearly visible are the quasiparticle thresholds above $4\Delta/e = 810 \mu\text{V}$ and the X-shaped resonant lines that represent the JQP cycle resonances. (b) Gate trace at $700 \mu\text{V}$ (circles) and a simulation (solid line) using Eqs. 1.3 and 1.19. Sample parameters were determined with (a). Data obtained from P. Hadley.

$|V| > 4\Delta/e = 800 \mu\text{V}$ for this sample. Figure 1.5b shows Coulomb oscillations of the current in the SSET. The peaks have a square form, whose width scales linearly with the voltage bias. Figure 1.6a shows the stability diagram of another sample with a lower resistance [6]. The onset of quasiparticle current is clearly visible with the sawtooth-like structure above a bias voltage of $4\Delta/e = 810 \mu\text{eV}$. Below this threshold, the most dominant transport mechanism is the simultaneous tunnelling of a Cooper pair and an electron, called the Josephson QuasiParticle (JQP) cycle [7]. The X-shaped resonant structures represent this cycle across the two different junctions. In Fig. 1.6b, the circles represent a measured gate trace at $700 \mu\text{V}$, showing the two separate JQP peaks, while the solid line is a simulation, using Eqs 1.3 and 1.19. The JQP cycle is discussed more elaborately in paragraph 1.6.

1.3 Master equation simulations

The master equation can be used to calculate the current in an arbitrary circuit of tunnel junctions, capacitors and voltage sources. An island is defined as a piece of metal connected to the environment or other circuit elements by at least one tunnel junction. Consider a circuit containing m islands, where the state of the circuit N is described by the number of excess electrons on all islands: $N =$

(n_1, n_2, \dots, n_m) . If we only take into account a finite number of excess electrons l , the system is described by the master equation

$$\frac{\partial}{\partial t} P_N = \sum_K P_K \Gamma_{K \rightarrow N} - P_N \sum_K \Gamma_{N \rightarrow K}, \quad (1.3a)$$

$$\sum_N P_N = 1, \quad (1.3b)$$

where P_N is the population of the state N , K represents all charge configurations other than N and $\Gamma_{K \rightarrow N}$ and $\Gamma_{N \rightarrow K}$ represent the transition rates between N and K . Equations 1.3a,b can be rewritten as a matrix equation $\frac{\partial}{\partial t} P = \Gamma P$. Here P is a $1 \times l^m$ column vector containing the population of all possible charge states and Γ is a $l^m \times l^m$ matrix containing all transition rates between the charge states. If all transition rates are calculated and the applied voltages are constant in time $\frac{\partial}{\partial t} P = 0$ and P can be calculated. The current I through a specific tunnel junction is calculated with

$$I = e \sum_N P_N (\Gamma_{N \rightarrow} - \Gamma_{N \leftarrow}), \quad (1.4)$$

where $\Gamma_{N \rightarrow}$ and $\Gamma_{N \leftarrow}$ are the forward and backward tunnel rates across this junction. The tunnel rates are calculated with Fermi's golden rule, using the change in free energy of a tunnel event. To calculate the free energy difference, first the electrostatic energy of the circuit is calculated as a function of the number of electrons on each island and all voltage sources

$$E(N, V) = \frac{1}{2} Q^T C^{-1} Q, \quad (1.5a)$$

$$Q = \begin{pmatrix} Q_1 + n_1 e \\ Q_2 + n_2 e \\ \dots \\ Q_k + n_m e \end{pmatrix}, \quad (1.5b)$$

$$C = \begin{pmatrix} C_{\Sigma 1} & -C_{12} & \dots & \dots & -C_{1m} \\ -C_{21} & C_{\Sigma 1} & -C_{32} & \dots & \\ \dots & -C_{32} & \dots & & \\ \dots & \dots & & C_{\Sigma(m-1)} & \\ -C_{m1} & & & & C_{\Sigma m} \end{pmatrix}, \quad (1.5c)$$

where Q is the total charge induced on an island by all voltage sources and the background charge, $C_{\Sigma i}$ is the total capacitance directly connected to node i and C_{ij} is the direct capacitance between nodes i and j . The chemical potential $\mu_k(N)$

is equal to the electrostatic energy difference associated with a tunnel event on island k and is defined as

$$\mu_k(N) = E(n_1, \dots, n_k, \dots) - E(n_1, \dots, n_k - 1, \dots). \quad (1.6)$$

The difference in free energy $\Delta F(k_n)$ of a tunnel event from electrode or island i to f is

$$\Delta F = \mu_f - \mu_i. \quad (1.7)$$

When an electron tunnels from or to an electrode connected to a voltage source $\mu = eV$, where V is the bias voltage of that source. With help of Eq. 1.2 the tunnel rate of all tunnel events can be calculated and Eq. 1.3 can be solved for P . The currents are finally calculated with Eq. 1.4.

To optimize the calculation time, the number of charge states l has to be minimized. This number can be minimized if the charge states that are used are centered around the charge state with the highest occupation probability. However, a priori the charge state with the highest probability on an island is unknown. For a SET with junction resistances R_1 and R_2 one can make the following estimate [8]

$$n_{opt} = \frac{-Q_0 - C_{g1}V_{g1}}{e} + \frac{-C_1V_1 - C_2V_2}{e} + \frac{C_\Sigma(R_1V_2 + R_2V_1)}{e(R_1 + R_2)}. \quad (1.8)$$

Usually $C_g, C_0 \ll C_1, C_2$ and the last two terms are only important for high bias, $V_{1,2} \gg \frac{E_C}{e}$.

1.4 The Josephson junction

When the electrode material of a tunnel junction is a superconductor, Cooper pairs carry the charge and can tunnel without a voltage. B. D. Josephson first predicted this effect and formulated the two Josephson equations [9]

$$I_B = I_C \sin \phi, \quad (1.9)$$

where I_C is the maximum supercurrent that can flow through the junction, the critical current, and ϕ the gauge invariant phase difference $\phi = \phi_1 - \phi_2 + \int_1^2 \mathbf{A} \cdot d\mathbf{l}$. Here ϕ_1 and ϕ_2 are the quantum mechanical phases of both superconducting electrodes and \mathbf{A} is the vector potential. The magnitude of I_C depends on the Josephson coupling energy $E_J = \hbar\Delta/8e^2R$ of the junction according to $I_C = 2eE_J/\hbar$. The second Josephson equation states that the phase difference evolves

in time with the Josephson frequency $\frac{2eV}{\hbar}$, when a voltage V is present over the junction

$$\frac{d\phi}{dt} = \frac{2eV}{\hbar}. \quad (1.10)$$

A frequently used model to describe the behavior of a Josephson junction is the resistively and capacitively shunted junction (RCSJ) model [10]. In this model, the Josephson junction is modelled as an ideal junction, obeying Eqs. 1.9 and 1.10, shunted by a resistance R_T and a capacitance C . Dissipation is modelled by the resistance, which includes both the (voltage dependent) junction resistance R_J and shunt resistance R_S . The shunt capacitor describes the geometric capacitance between the leads. As shown in Fig. 1.7, the bias current through the circuit is the sum of three parallel channels

$$I_B = I_C \sin \phi + \frac{V}{R_T} + C \frac{dV}{dt}. \quad (1.11)$$

Eliminating V with use of Eq. 1.10 gives a second-order differential equation which can be rewritten as

$$\frac{d^2\phi}{d\tau^2} + \frac{1}{\sqrt{\beta_c}} \frac{d\phi}{d\tau} + \sin \phi = \frac{I_B}{I_C} = i, \quad (1.12)$$

where the time τ is normalized to the plasma frequency $\omega_p = \sqrt{\frac{2eI_c}{\hbar C}}$ of the junction. Furthermore β_c is the McCumber-parameter

$$\beta_c = (\omega_p RC)^2 = \frac{2eI_c R_T^2 C}{\hbar}. \quad (1.13)$$

This parameter is the ratio between the main time constants of the system, the RC-time and the plasma frequency of the Josephson junction. Depending on the

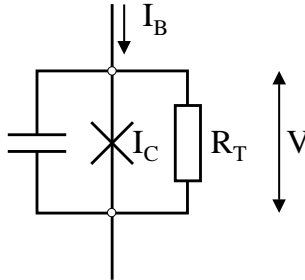


Figure 1.7: Schematic of a resistively and capacitively shunted Josephson junction. The cross denotes a pure Josephson element, obeying Eqs. 1.9 and 1.10.

value of β_c , the IV-characteristic of the junction is hysteretic ($\beta_c > 1$) or non-hysteretic ($\beta_c \leq 1$). These parameter regimes resemble those of an underdamped and an overdamped pendulum respectively.

The bias current I_B in equation 1.12 can be either static in time, or a time dependent bias current. Usually the differential equation has to be solved numerically. For a constant high bias $i \gg 1$, the phase evolves linearly in time and a flux quantum passes through the junction every $(\frac{2eV}{h})^{-1}$ s.

1.5 The Cooper pair box

A schematic of the superconducting box circuit or Cooper pair box (CPB) is shown in Fig. 1.8a. The CPB consists of a superconducting island connected to a lead with a Josephson junction. The potential of the island can be tuned with a gate voltage. If the Josephson energy E_J is smaller than the charging energy E_C and $E_C < \Delta$, the system is effectively a two-level system. Charge is quantized in units of $2e$ and only two charge states are accessible, zero $|0\rangle$ and one excess Cooper pair on the island, $|2\rangle$. In this charge basis, the system is described by the following Hamiltonian

$$H = 4E_C (n_g^2 |0\rangle \langle 0| + (1 - n_g)^2 |2\rangle \langle 2|) - \frac{E_J}{2} (|2\rangle \langle 0| + |0\rangle \langle 2|). \quad (1.14)$$

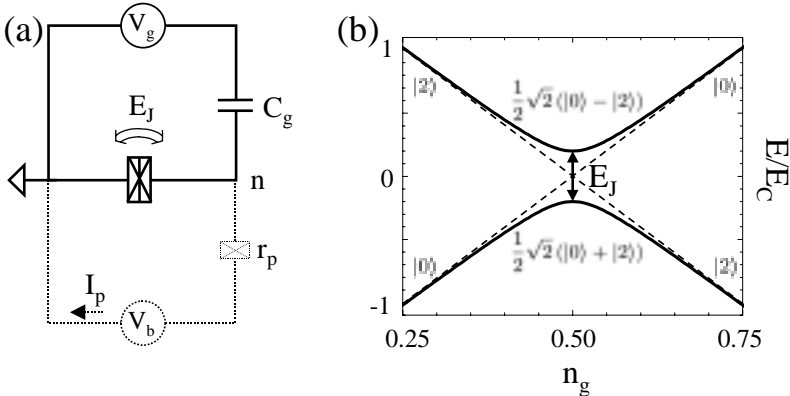


Figure 1.8: (a) Schematic of a Cooper pair box. An additional high-ohmic probe junction (dashed) can be used to measure the charge state of the system. (b) Energy diagram of a CPB where $E_J = 0.4E_C$. At $n_g = 0.5$ the level splitting is E_J and the ground state of the system is a superposition of charge states $|0\rangle$ and $|2\rangle$.

Here n_g is the charge induced on the island by all voltage sources, normalized to $2e$. The charging term couples charge states with the same charge, while the Josephson term couples charge states which differ by one Cooper pair. The ground state, found by solving the time-independent Schrödinger equation $H\Psi = E\Psi$, is a superposition of states $|0\rangle$ and $|2\rangle$. First evidence of this superposition was measured by Bouchiat et al. [11]. They used a SET to measure the average charge on the CPB and observed a staircase-like dependence of the average charge on the induced gate charge of the CPB. This indicated that charge was quantized in units of $2e$, but more importantly, they showed that the steps were rounded due to quantum mechanical fluctuations of the charge, i.e. the ground state was a superposition of charge states.

By solving the Schrödinger equation, the band structure of the CPB can also be calculated. Figure 1.8b shows the band structure of a CPB where $E_J = 0.4E_C$. The band structure has a gap of E_J at $n_g = \frac{1}{2}$. The gap in the band structure was experimentally probed with microwaves by Nakamura et al. [12]. They connected a probe junction to the island of the CPB, shown as the dashed circuit in Fig. 1.8a. The probe junction was biased by a voltage source V_b . To be able to measure the band gap, the level broadening should be smaller than E_J , the coherent regime. The level broadening due to quasiparticles tunnelling through the probe junction is of the order of $\hbar\Gamma$, where Γ is the tunnel rate. Consequently the probe junction should have a high resistance such that $\hbar\Gamma < E_J$. At $n_g = \frac{1}{2}$ no photon-assisted tunnelling current was measured for $hf < E_J$, indicating the presence of a gap in the band structure.

Apart from the average charge on the CPB, one would like to follow the charge on the CPB in time. The dynamics of a CPB can be predicted by solving the time dependent Schrödinger equation

$$i\hbar \frac{\partial}{\partial t} |\Psi\rangle = H |\Psi\rangle, \quad (1.15)$$

where H is the Hamiltonian as defined by Eq. 1.14. By applying pulses to the gate for example, the n_g term in H becomes time dependent and the solution $|\Psi\rangle$ will also be time dependent. Nakamura et al. have performed an experiment where the gate voltage is pulsed non-adiabatically to $n_g = \frac{1}{2}$ for a certain time Δt [13]. The solution of Eq. 1.15 shows that at $n_g = \frac{1}{2}$, $|\Psi\rangle$ will oscillate between $|0\rangle$ and $|2\rangle$ with the frequency E_J/\hbar . As the probe current is proportional to the probability of charge state $|2\rangle$, a measurement of the probe current versus Δt should reveal these coherent oscillations of the charge. The measurements by Nakamura et al. are shown in Fig. 1.9, clearly showing an oscillatory behavior with the right period, $T_{coh} = \hbar/E_J$.

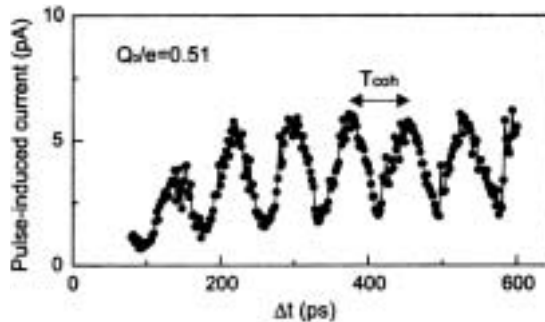


Figure 1.9: Pulse-induced probe current, demonstrating coherent oscillations of the charge in a Cooper pair box. [Reproduced after Y. Nakamura and J. S. Tsai, *Jour. of Low Temp. Phys.* **118**, 765 (2000), with permission of the authors.]

Instead of applying a pulse, the CPB can also be radiated by pulsed microwaves. If the frequency matches the level splitting at a particular gate voltage, the system will undergo Rabi-oscillations [14]. The system oscillates between the ground state and the excited state with a frequency that depends on the amplitude of the applied microwaves.

1.6 The Josephson quasiparticle cycle

In a superconducting SET, or equivalently a CPB with attached probe junction, the coherent (ie. reversible) tunnelling of a Cooper pair through a Josephson junction is interrupted by the incoherent (ie. irreversible) tunnelling of a quasiparticle through the other junction. The Josephson quasiparticle cycle is completed by a second quasiparticle tunnelling through the other junction. If $E_J < E_C < \Delta$, we can assume that only three charge states are occupied on the island: $|0\rangle$, $|1\rangle$, and $|2\rangle$, with $|0\rangle$ and $|2\rangle$ having Josephson coupling while $|1\rangle$ is only accessible by quasiparticle tunnelling from $|2\rangle$. This corresponds to having a Cooper pair resonance at one of the junctions, but not at the other.

If there were no quasiparticle tunnelling, the time evolution of the system between $|0\rangle$ and $|2\rangle$ could be described using the Schrödinger equation 1.15. On the other hand, if there were no Cooper pair tunnelling, then the time evolution is stochastic and can be described by the master equation 1.3. Since both Cooper pair and quasiparticle tunnelling occur in the JQP cycle, some combination of these two approaches is necessary to describe the time evolution of the system.

The state of the system is described by the density matrix

$$\rho = \sum_a p_a |\Psi_a\rangle \langle \Psi_a| = \sum_{nk} \rho_{nk} |n\rangle \langle k| = \begin{bmatrix} \rho_{00} & \rho_{01} & \rho_{02} \\ \rho_{10} & \rho_{11} & \rho_{12} \\ \rho_{20} & \rho_{21} & \rho_{22} \end{bmatrix}, \quad (1.16)$$

where $\rho_{nk} = c_n c_k^*$. The diagonal elements, $\rho_{nn} = |c_n|^2 = P_n$, are the populations of the charge states, while the off-diagonal elements represent coherences between states due to Josephson coupling. Since the $|1\rangle$ state has no coherences with any allowed charge state, $\rho_{01} = \rho_{10} = \rho_{21} = \rho_{12} = 0$. Also, since ρ is Hermitian, $\rho_{20} = \rho_{02}^*$. The density matrix evolves according to

$$i\hbar \frac{\partial}{\partial t} \rho = [H, \rho], \quad (1.17)$$

where $H = H_0 + H_T$ is the full Hamiltonian, ignoring the environment; H_0 is the Cooper pair Hamiltonian of Eq. 1.14 with an additional term $|1\rangle \langle 1|$ added to the charging energy to account for the presence of a single quasiparticle, and H_T describes the incoherent tunnelling. Gurvitz et al. have shown that one can take this decoherence into account by separating the Hamiltonian into coherent (H_0) and incoherent (H_T) terms, resulting in the following set of equations for the time evolution of the different density matrix elements [15]

$$\frac{\partial}{\partial t} \rho_{nn} = -\frac{i}{\hbar} \langle n | [H_0, \rho] | n \rangle + \sum_k \rho_{kk} \Gamma_{k \rightarrow n} - \rho_{nn} \sum_k \Gamma_{n \rightarrow k}, \quad (1.18a)$$

$$\frac{\partial}{\partial t} \rho_{nk} = -\frac{i}{\hbar} \langle n | [H_0, \rho] | k \rangle - \frac{1}{2} \rho_{nk} \left(\sum_m \Gamma_{n \rightarrow m}^{(d)} + \sum_m \Gamma_{k \rightarrow m}^{(d)} \right). \quad (1.18b)$$

The first term of each equation determines the coherent evolution of each element. The other terms resemble the master equation. For the diagonal elements (populations), there are gain and loss terms due to the incoherent tunnel rates Γ , but the coherences have only a loss term set by an effective decoherence rate $\Gamma^{(d)}$. We will assume that this decoherence rate is identical to the quasiparticle tunnel rate in the JQP cycle. There may be other contributing factors to decoherence, but the quasiparticle tunnel rate (~ 1 -100 GHz) probably dominates.

The JQP cycle is modelled as follows. The state $|2\rangle$ decays to $|1\rangle$ with quasiparticle tunnel rate Γ_{p1} , and $|1\rangle$ decays to $|0\rangle$ with rate $\Gamma_{p2} < \Gamma_{p1}$. For steady-state solutions, the left hand side of Eqs 1.18a,b is equal to zero. The steady-state probabilities ρ_{nn} of the charge states $|0\rangle$, $|1\rangle$, and $|2\rangle$ can now be calculated. The resulting JQP current is

$$I_p = e(\Gamma_{p1} \rho_{22} + \Gamma_{p2} \rho_{11}) = \frac{2e\Gamma_{p1}}{\frac{4\delta^2 + \hbar^2 \Gamma_{p1}^2}{E_J^2} + 2 + \frac{\Gamma_{p1}}{\Gamma_{p2}}}, \quad (1.19)$$

where the energy δ represents the detuning of the SSET from the Cooper pair resonance due to a gate or bias voltage. The detuning is the free energy difference associated with tunnelling of a Cooper pair. For example, the free energy difference for a Cooper pair tunnelling onto the island through junction 1 in Fig. 1.2 is

$$\delta = \Delta F (0 \Rightarrow 2) = \frac{2e}{C_\Sigma} [-V_1 (C_2 + C_g) + C_g V_g + Q_0 + e], \quad (1.20)$$

in case of an asymmetric bias ($V_2 = 0$). In the coherent regime $\hbar\Gamma_{p1} \ll E_J$, the Cooper pair tunnels back and forth many times, before being interrupted by a tunnelling quasiparticle. In this regime, the probe current is proportional to Γ_{p1} and the peak width is proportional to E_J . In the incoherent regime $\hbar\Gamma_{p1} \gg E_J$, the probe current is proportional to E_J^2 and the peak width is proportional to $\hbar\Gamma_{p1}$.

There is a close analogy between the JQP current through a SSET and a resonant tunnelling current through two coupled quantum dots with a large level splitting. The tunnelling between two quantized levels in the quantum dots is analogous to coherent tunnelling of a Cooper pair, and two quasiparticles tunnelling through the probe junction is analogous to a first quasiparticle tunnelling into one dot and a second quasiparticle tunnelling out of the other dot. By replacing Γ_{p2} , Γ_{p2} and E_J by Γ_{p2} , Γ_{p2} and $2T_C$, the same formula is obtained as proposed by Nazarov [16]. A result similar to Ref. [12] for the SSET has for example also been measured in coupled quantum dots [17].

1.7 Multi-layer fabrication

Different fabrication methods have been used for the samples described in this thesis. The general details of multi-layer fabrication are described in the chapters themselves, here we will discuss the details of the multi-layer sample fabrication.

The general recipe for the fabrication of each separate layer is as follows. A double layer of electron sensitive resist is spun onto the silicon substrate. The bottom layer is usually 400 nm thick, while the top layer is approximately 75 nm thick. The bottom layer has a higher electron sensitivity than the top layer. The desired structure is written into the resist with an electron beam with beam spot sizes of 3 to 50 nm. The different electron sensitivity of the resist layers leads to undercut. When the exposed resist is removed with a developer, the pattern in the bottom layer is slightly larger. A thin film of material is then evaporated perpendicularly to the substrate normal in a high vacuum electron gun evaporation system. The undercut eases the removal of excess resist after

evaporation and even allows one to evaporate material under small angles from the substrate normal.

To align subsequent layers, the first layer contains markers. To be able to find these markers with the electron beam, they are made of a material with a high atomic mass, usually platinum or gold. This layer can also be used to make resistive shunts with these materials. The second layer usually contains the aluminum structures to capacitively couple elements in the third layer. The second layer is covered by an insulator like SiO₂, or the aluminum is heavily oxidized to form an insulating Al_xO_y layer. Because of problems with the insulation of SiO₂, the latter method was developed in our group. The sample is heated to 150 °C and oxidized in an oxygen plasma. Figure 1.10 shows the oxide thickness as a function of the O₂ pressure in the vacuum chamber. Oxide thicknesses of 10 nm are feasible with this technique. Tests revealed that leakage is only a few pA/mm² for a field of 0.1 V/m, while the leakage current exponentially depends on the electric field.

In the last layer, small tunnel junctions are fabricated by shadow evaporation of aluminum [18]. When a pattern is exposed like in Fig. 1.11a development results in a free hanging bridge. Figure 1.11b is a cross-section of Fig. 1.11a and shows the principle of shadow evaporation. Two layers of aluminum (30 nm and 50 nm) are evaporated from opposite angles. The first layer is oxidized in 5-250 mTorr of pure oxygen. After evaporation all resist is removed with

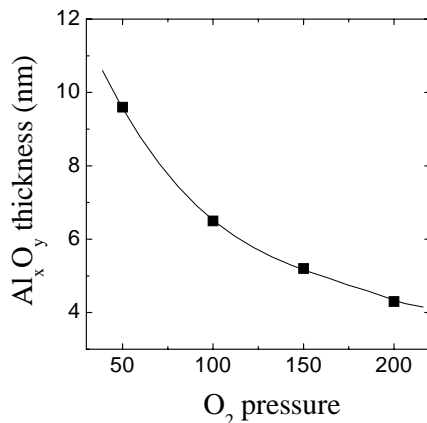


Figure 1.10: Oxide thickness versus the oxide pressure in the vacuum chamber. The sample was heated to 150 °C and a current of 50 mA was forced through the plasma for 5 minutes.

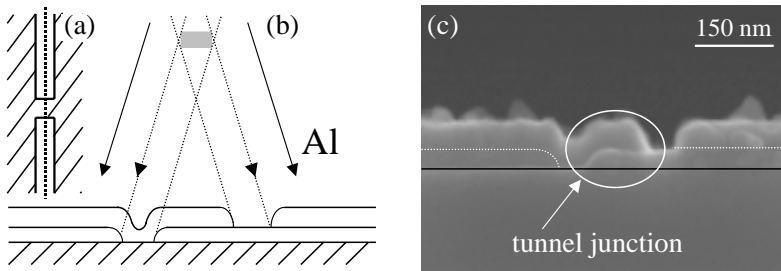


Figure 1.11: (a) Top view of the double layer resist. The cross-hatched parts are unexposed resist. (b) Cross sectional schematic of a shadow evaporated tunnel junction along the dashed line in (a). (c) Scanning electron microscope picture of a finished tunnel junction. The location of the actual tunnel barrier is visible in between the two aluminum layers.

acetone. A cross sectional scanning electron microscope image of the resulting tunnel junction is shown in Fig. 1.11c.

1.8 Thesis layout

In the first part of this thesis we look at the performance of the various single-electron devices. Chapter 2 and Chapter 3 discuss a single-electron transistor switched by the presence of an electron and the single-electron inverter respectively. Chapter 4 suggests an alternative use of the superconducting SET as a strongly coupled charge spectrometer. The experiments of Chapter 5 show that strong capacitive coupling can also be used to couple quantum fluctuations of the charge. Chapters 6 and 7 study whether the Josephson junction is suitable as an on-chip radiation source for use in mesoscopic experiments.

References

- [1] See for example <http://developer.intel.com/>.
- [2] K. K. Likharev, *IEEE Trans. Mag* **23**, 1142 (1987).
- [3] V. A. Krupenin, D. E. Presnov, A. B. Zorin, and J. Niemeyer, *J. Low Temp. Phys.* **118**, 287 (2000).
- [4] D. V. Averin and K. K. Likharev in *Mesoscopic Phenomena in Solids*, edited by B. L. Altshuler, P. A. Lee and R. A. Webb (Elsevier, Amsterdam, 1991).

-
- [5] An example of the MatLab source code for the calculation of the tunnel rate in an all-superconducting junction can be found at <http://qt.tn.tudelft.nl/research/set/super.html>.
- [6] Data obtained from P. Hadley, E. Delvigne, E. H. Visscher, S. Lähteenmäki, and J. E. Mooij, *Phys. Rev B* **58**, 15317 (1998).
- [7] Y. Nakamura, C. D. Chen, and J. S. Tsai, *Phys. Rev. B* **53**, 8234 (1996).
- [8] For a derivation: <http://qt.tn.tudelft.nl/~hadley/set/transistor/nopt.html>.
- [9] B. D. Josephson, *Phys. Lett.* **1**, 251 (1962).
- [10] See for example M. Tinkham, *Introduction to Superconductivity* p. 202 (McGraw-Hill, New York, 1996), second edition; T. P. Orlando en K. A. Delin, *Foundations of Applied Superconductivity* p. 458 (Addison-Wesley, Reading, 1991), first edition.
- [11] V. Bouchiat, D. Vion, P. Joyez, D. Esteve, and M. H. Devoret, *Phys. Scr.* **T76**, 165 (1998); *Journ. Supercond.* **12**, 789 (1999).
- [12] Y. Nakamura, C. D. Chen, and J. S. Tsai, *Phys. Rev. Lett.* **79**, 2328 (1997).
- [13] Y. Nakamura, Yu. A. Pashkin, J. S. Tsai, *Nature* **389**, 786 (1999); Y. Nakamura and J. S. Tsai, *Jour. of Low Temp. Phys.* **118**, 765 (2000); Y. Nakamura and J. S. Tsai, *Journ. of Sup.* **12**, 799 (1999).
- [14] See for example Cohen Tannoudji, Diu and Laloë, *Quantum Mechanics* (John Wiley & Sons, New York, 1977).
- [15] S. A. Gurvitz, *Phys. Rev. B* **57**, 6602 (1998).
- [16] Yu. V. Nazarov, *Physica B* **189**, 57 (1993).
- [17] T. H. Oosterkamp, T. Fujisawa, W. G. van der Wiel, K. Ishibashi, R. V. Hijman, S. Tarucha, and L. P. Kouwenhoven, *Nature* **395**, 873 (1998).
- [18] T. A. Fulton and G. J. Dolan, *Phys. Rev. Lett.* **59**, 109 (1987).

Chapter 2

Negative differential resistance due to single-electron switching

C. P. Heij, D. C. Dixon, P. Hadley and J.E. Mooij

We present the multilevel fabrication and measurement of a Coulomb-blockade device displaying tunable negative differential resistance (NDR). Applications for devices displaying NDR include amplification, logic, and memory circuits. Our device consists of two Al/Al_xO_y islands that are strongly coupled by an overlap capacitor. Our measurements agree excellently with a model based on the orthodox theory of single-electron transport.

2.1 Introduction

Single-electron tunnelling devices offer a means to manipulate individual electrons. Their advantages of small size and low power dissipation have stimulated a number of proposals for their use in some future generation of computation technology [1], yet relatively few such circuits have been measured. Many techniques exist for creating single-electron devices, including the use of scanning probes to manipulate the nanometer scale structures necessary for room temperature operation. These structures have so far been limited to planar layouts, which severely restrict possible circuit architectures because voltage gain becomes difficult to achieve and wire crossing is impossible. The most widely used fabrication technique, electron beam lithography, allows one to build multilayered circuits that can circumvent these problems. E-beam lithography, however, has a minimum resolution of 10 nm; consequently, single-electron effects can usually only

This chapter was published in 'Applied Physics Letters **74**, 1042 (1999)'

be observed at low temperature ($T < 1$ K) in devices built this way. Up to now, technologically oriented research has primarily focused on the further miniaturization of basic components, while ignoring the fabrication and testing of more complex circuits. We feel it is worthwhile to consider low-temperature prototypes of these circuits to estimate the usefulness of their future high-temperature counterparts.

In this chapter we report on a multilayer circuit consisting of two strongly coupled Al/Al_xO_y islands fabricated using electron beam lithography and measured at low temperature. The circuit demonstrates negative differential resistance (NDR) due to the tunnelling of a single electron into one of the islands. Device applications of NDR—including amplification, logic and memory—have been extensively discussed in literature regarding resonant tunnel diodes [2]. Single-electron NDR has been predicted in systems of multiple islands, where electrostatic repulsion between electrons in different islands regulates the source-drain current [3, 4]. Our circuit offers the advantage of requiring only two islands, rather than six arranged in a zig-zag [3], or four in a ring geometry [4].

2.2 Experimental details

The equivalent circuit diagram of our device is shown in Fig. 2.1a. The left island forms a single-electron transistor (SET), allowing a current I to flow between the voltage source V_b and ground. The right island, however, merely traps charge entering from the source, and so acts as an "electron box" [5]. The two islands are also coupled by a large mutual capacitance C_m , but electron tunnelling between the islands is forbidden. Additional control is provided by tuning gate voltages V_{g1} and V_{g2} , which determine the electrostatic potentials and charge states of the islands. The current through a solitary SET depends both upon the bias voltage across its terminals and the gate voltage. In our setup the SET feels an additional effective gate voltage due to the charge state of the electron box. Whenever a single extra electron tunnels into the box, there is a discontinuous change in charge on C_m , resulting in a jump in the effective gate voltage felt by the SET and consequently a jump in the current[†] [6]. The NDR mechanism is as follows. The SET is tuned so that it conducts at low V_b , while the box is in Coulomb blockade. When V_b is increased past some threshold voltage and

[†] A conceptually similar experiment was described in Ref. [6]. There the tunnel current through a metallic grain was studied with a scanning tunnelling microscope (STM). The voltage bias of the STM also charged a neighboring grain that was capacitively coupled to the first grain. This resulted in jumps in the IV-characteristic, that could be explained by a mechanism similar to the mechanism presented in this chapter.

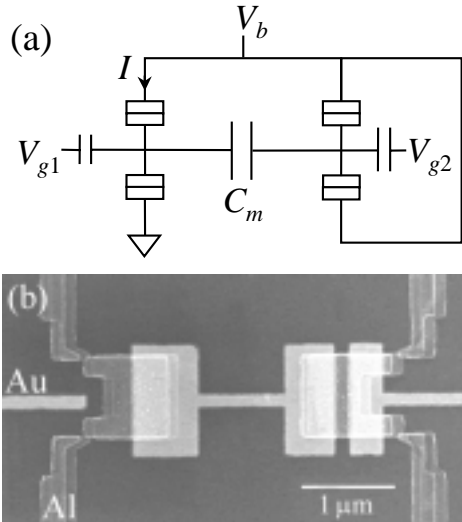


Figure 2.1: (a) Schematic circuit diagram of the device. Electrons flow from source to drain through the left island, while the right island forms an "electron box." (b) SEM photograph of the multilevel device, with two Al/Al_xO_y islands coupled to each other by an underlying Au layer. The islands' potentials can also be tuned using gate electrodes in this layer.

overcomes this blockade, an electron tunnels into the box and becomes trapped. Due to the mutual capacitance C_m , this extra electron increases the electrochemical potential of the SET and pushes it into Coulomb blockade, decreasing I . In other words, the addition of a single extra electron to the box switches the SET from "on" to "off." Simulations (described below) have shown that C_m should be approximately larger than the junction capacitance in order to see the effect. Junction capacitances C_j of 0.2-0.3 fF are obtainable in Al/Al_xO_y, the material of choice for most single-electronics experiments. Such a high value of C_m is difficult to achieve in a planar, single-layer design [7]. Much higher capacitances are attainable by overlapping circuit elements, which requires multilevel fabrication [8].

Figure 2.1b shows a Scanning Electron Microscope (SEM) photograph of our device, consisting of an Al island layer (medium gray) and an underlying Au gate layer (light gray), with a thin intermediate SiO layer providing electrical insulation. The tunnel junctions are formed at the corners of the islands where they meet the pointed ends of the leads. Three sections of the gate layer are

visible; the two structures extending from the left and right sides are the tuning gates, while the central dumbbell-shaped structure underlaying both islands forms the mutual capacitor C_m .

The device was fabricated on a silicon substrate with a 250 nm thermally oxidized top layer, and patterned using standard electron beam lithography with a high resolution pattern generator in a double layer electron-sensitive resist. The bottom gate layer was formed by evaporating 5 nm of Ti and 20 nm of Au perpendicular to the substrate surface. Directly after lift-off the whole sample was covered with a 32 nm insulating SiO layer. To ensure good step coverage, SiO was evaporated under four perpendicular angles oriented 30° to the substrate surface normal. The islands, leads and contact pads were written in a new bilayer of electron-sensitive resist after aligning the electron beam pattern generator to Au markers defined in the gate layer. A pattern generator alignment resolution of 50 nm or less is necessary to produce good results. The tunnel junctions were formed using the standard technique of double angle shadow evaporation of Al through the resist mask, oxidizing the Al between evaporations [9]. Contact pads were coupled to the gates by 0.2 pF overlap capacitors. To protect the junctions from high voltage static discharges, the leads were shunted on-chip by 12 pF overlap capacitors.

2.3 Experimental results

The device was measured in a standard ^3He - ^4He dilution refrigerator at a base temperature of 4 mK (electron temperature ≈ 27 mK). An external magnetic field of 1 T was applied to suppress superconductivity. From high-bias measurements, the total tunnelling resistances of the SET and the box were determined to be 7 M Ω and 13 M Ω , respectively. Having verified that all the junctions had finite tunnelling resistances, the leads were connected as in Fig. 2.1a. No leakage current through the SiO insulating layer was detected. A typical measurement of the current I as a function of source-drain bias V_b is plotted in Fig. 2.2. The device clearly demonstrates NDR in the bias range of 110-130 μV , with a peak-to-valley ratio in excess of 30. A more precise determination of this ratio is difficult, however, due to an enhancement of low-frequency noise around the NDR onset, possibly caused by thermally activated charge fluctuations in the box. Fig. 2.2 also shows enhanced differential conductance at $V_b \approx -70 \mu\text{V}$. This feature is due to a mechanism similar to NDR, but where the trapping of an extra electron in the box suddenly pulls the SET *out* of Coulomb blockade. The NDR features can be shifted by tuning the gate voltages. The dependence on V_{g1} is shown in

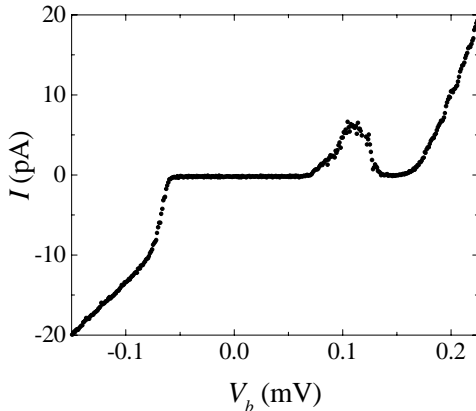


Figure 2.2: Typical data sweep showing both NDR for positive bias and enhanced differential conductance for negative bias, both due to single-electron switching in the "electron box" island. The electron temperature is 27 mK.

Fig. 2.3a, where the differential conductance $\partial I/\partial V_b$ is plotted in grayscale as a function of V_b and V_{g1} . Here we see diamond-shaped Coulomb blocked regions (marked by " $I = 0$ "), fractured by the discrete charging of the box. Black regions represent NDR, while white represents enhanced differential conductance.

The electrostatic potentials of a two-island circuit may be expressed analytically in terms of the applied voltages, the charge state of each island, and the capacitances [10]. Consequently, the slopes of the various thresholds in Fig. 2.3a, combined with similar measurements (such as by sweeping V_{g2}), allow us to fully characterize the capacitor network of the device. The junction capacitances were all approximately 0.3 fF, while C_m was estimated to be 0.64 fF. Using our estimated capacitances, we have carried out simulations of the device using a master equation approach combined with the orthodox theory of single-electron tunnelling [11, 12]. The simulation of Fig. 2.3b shows $\partial I/\partial V_b$ as a function of V_b and V_{g1} , assuming an electron temperature of 25 mK. It correctly reproduces the position and character of the features in Fig. 2.3a, with only minor variations. We similarly found excellent agreement between experiment and simulation when V_{g2} was swept.

Simulations show that the magnitude of NDR gradually decreases with increasing temperature, vanishing when:

$$kT \gtrsim \frac{1}{4} \frac{e^2 C_m}{C_1 C_2 - C_m^2}. \quad (2.1)$$

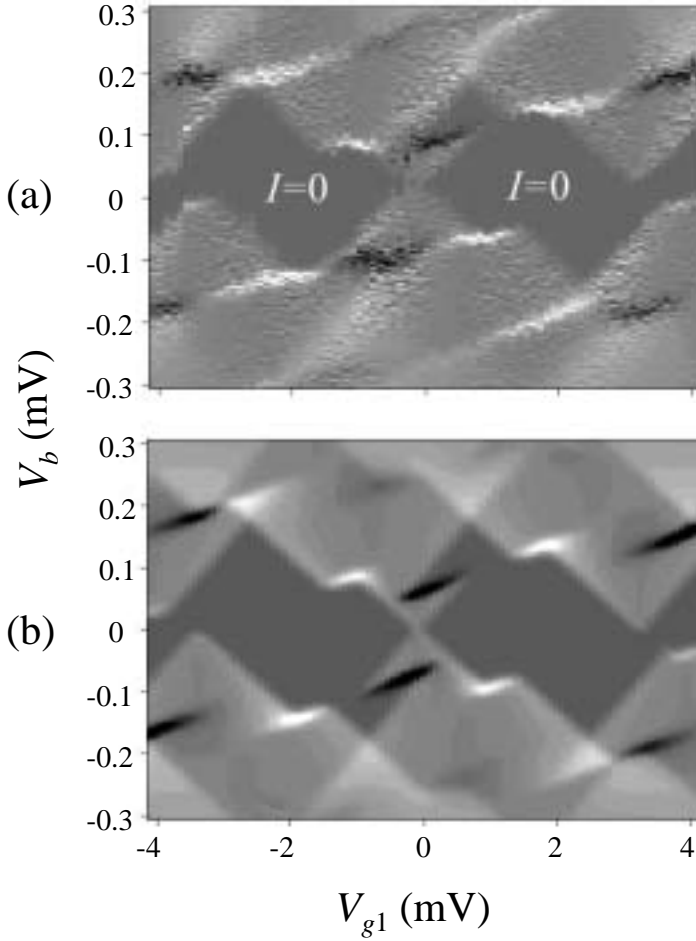


Figure 2.3: (a) Grayscale plot of $\partial I/\partial V_b$ as a function of V_{g1} and V_b , showing the tunability of the NDR onset (black, $-1\mu\text{S}$) and the enhanced differential conductance (white, $1\mu\text{S}$). The periodicity of the SET is 3.5 mV. (b) Master-equation simulation of the device, using capacitances estimated from multivariable fitting of the features in (a).

Here $C_{1(2)}$ is the total capacitance of the SET (box) including the coupling capacitance C_m . This maximum temperature was approximately 150 mK for our device, and measurements at $T = 100$ mK confirmed that NDR exists, but is greatly diminished, at this higher temperature. Simulations also predict that, for sufficiently large $C_m > 3C_j$, multiple NDR regimes should appear. We estimate that a fully optimized device using our multilevel technique could yield a C_m/C_j ratio of 10, making possible the study of very strongly coupled metallic islands.

2.4 Conclusions

In conclusion, we have measured negative differential resistance due to single-electron switching in a circuit with a strong capacitive coupling between two islands. Measurements were in excellent quantitative agreement with semiclassical simulations. Our multilevel fabrication process allows inter-island couplings unmatched by any planar architecture, perhaps allowing the observation of new physical effects. Our measurements also demonstrate the strong influence that the introduction of a single electron can have on the conductance of a small island of charge, an effect that will only gain importance as the present trend of transistor miniaturization proceeds. We acknowledge useful input from Paul McEuen and K. K. Likharev.

References

- [1] For a review, see K. K. Likharev, Proceedings of the IEEE **87**, 606 (1999).
- [2] *Tunnel-Diode and Semiconductor Circuits*, edited by John M. Carroll (McGraw-Hill, New York, 1963).
- [3] Hiroshi Nakashima and Kiyohiko Uozumi, Jpn. J. Appl. Phys. **34**, L1659 (1995); *ibid.*, Int. J. Electronics **83**, 333 (1997).
- [4] Mincheol Shin, Seongjae Lee, Kyoung Wan Park, and El-Hang Lee, Phys. Rev. Lett. **80**, 5774 (1998).
- [5] P. Lafarge, H. Pothier, E. R. Williams, D. Esteve, C. Urbina and M. H. Devoret, Z. Phys. B **85**, 327 (1991).
- [6] C. T. Black, M. T. Tuominen, and M. Tinkham, Phys. Rev. B **50**, 7888 (1994).
- [7] G. Zimmerli, R. L. Kautz, and John M. Martinis, Appl. Phys. Lett. **61**, 2616 (1992).

- [8] E. H. Visscher, S. M. Verbrugh, J. Lindeman, P. Hadley, and J. E. Mooij, *Appl. Phys. Lett.* **66**, 305 (1995).
- [9] T. A. Fulton and G. J. Dolan, *Phys. Rev. Lett.* **59**, 109 (1987).
- [10] See, for example, David C. Dixon, Ph.D. thesis, Berkeley, University of California, 1998.
- [11] D. V. Averin and K. K. Likharev, in *Mesoscopic Phenomena in Solids*, edited by B. L. Altshuler, P. A. Lee, and R. A. Webb (Elsevier, Amsterdam, 1991) p. 173.
- [12] G.-L. Ingold and Yu. V. Nazarov, in *Single Charge Tunneling*, edited by H. Grabert and M. H. Devoret (Plenum, New York, 1992) pp. 21-108.

Chapter 3

A single-electron inverter

C. P. Heij, P. Hadley and J.E. Mooij

A single-electron inverter was fabricated that switches from a high output to a low output when a fraction of an electron is added to the input. For the proper operation of the inverter, the two single-electron transistors that make up the inverter must exhibit voltage gain. Voltage gain was achieved by fabricating a combination of parallel-plate gate capacitors and small tunnel junctions in a two-layer circuit. A comparison is made between an inverter in the normal state and one in the superconducting state.

3.1 Introduction

The use of single-electron tunnelling devices for computation has been widely discussed because these devices can be made very small and they consume relatively little power [1, 2]. A variety of single-electron device logic schemes have been put forward but relatively few of the proposed single-electron logic elements have been tested experimentally. Here, measurements on a single-electron inverter are presented. The inverter is a fundamental building block of single-electron transistor logic, which bears considerable resemblance to standard Complementary Metal-Oxide-Semiconductor (CMOS) logic [3, 4]. The logic levels are represented by voltages and a small number of electrons are transported when the inverter switches from the high state to the low state. The logic gates NAND and NOR can be realized by making slight variations on the inverter circuit. With two inverters, a static Random Access Memory (RAM) memory cell can be constructed

Parts of this chapter were published in 'Applied Physics Letters **78**, 1140 (2001)'

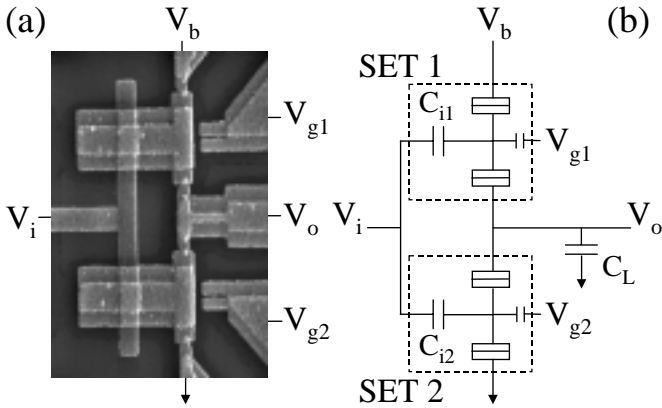


Figure 3.1: (a) A scanning electron microscope image of the inverter and (b) the corresponding schematic. The width of the T-shaped islands is $1 \mu\text{m}$. The dotted lines outline the two SET's in the circuit. The load capacitor C_L is not shown in the SEM photo.

and a ring oscillator can be made from three inverters. Voltage gain is essential for many of these circuit applications but thus far gain has been achieved in relatively few devices [5, 6, 7, 8]. The inverter discussed here has voltage gain.

3.2 Experimental details

A scanning electron microscope (SEM) photograph of the device and a schematic diagram of the inverter circuit are shown in Fig. 3.1a and 3.1b. The inverter consists of two nominally identical single-electron transistors (SET's) in series that share a common input gate. The SET's are outlined with dotted lines in the schematic. The input of the inverter, V_i , extends under the two islands. The input is electrically isolated from the two islands by an 8 nm thick layer of aluminum oxide. This forms the two input capacitors C_{i1} and C_{i2} . The output V_o is connected to ground via an on-chip load capacitor C_L of 130 pF to suppress charging effects at the output. The output is also coupled to the two islands via small tunnel junctions. The power lead, V_b , and the grounded lead are similarly connected to the islands via small tunnel junctions. The two tuning gates, V_{g1} and V_{g2} , are used to tune the induced charges on the two islands.

Figure 3.2 shows two simulations of the individual currents through both SETs versus the output voltage. The input voltage was changed from $18 \mu\text{V}$ in Fig. 3.2a

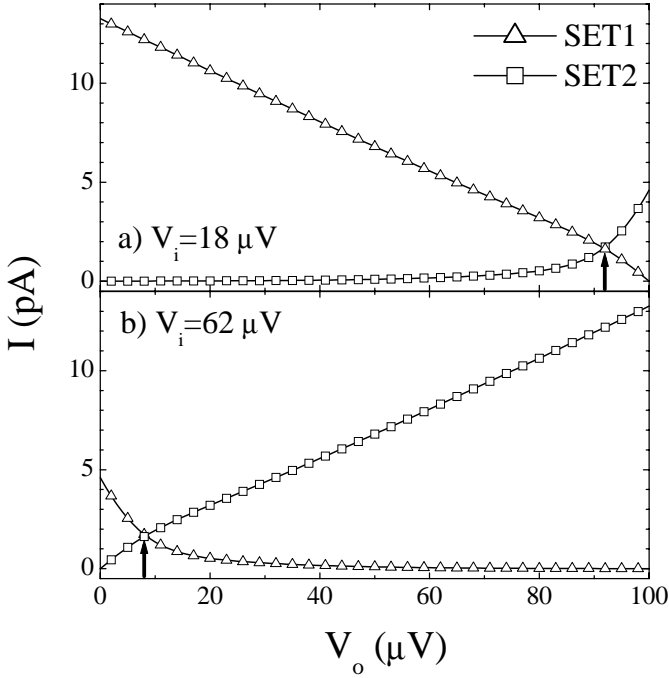


Figure 3.2: Simulation of the individual currents I through each SET as a function of the output voltage V_o for (a) $V_i = 18 \mu\text{V}$ and (b) $V_i = 62 \mu\text{V}$. The bias voltage is $100 \mu\text{V}$ and $T=30 \text{ mK}$. The output voltage is stable when both currents are equal, indicated by the arrows. The actual sample parameters were used to perform the simulations.

to $62 \mu\text{V}$ in Fig. 3.2b while all other voltages were kept constant. This corresponds to inducing an extra charge of $0.22e$ onto the input capacitors. In the experiments, the output voltage adjusted such that the current through both SETs was equal, indicated by the arrows. For inverter operation, the output should be high when the input is low and the output should be low when the input is high. When C_Σ is the total capacitance of an island to ground, maximum output swing is achieved by applying a bias voltage of $V_b = e/C_\Sigma$ and adjusting the two tuning gates such that when the input voltage is low, the top transistor (SET1) is conducting and the bottom transistor (SET2) is in the Coulomb blockade (Fig. 3.2a). This effectively connects the output to the supply voltage and makes the output high. When a high input voltage is applied, this shifts the induced charge on each of the SET's by a fraction of an electron and puts the top transistor in Coulomb blockade and makes the bottom transistor conducting so that the output is effectively

connected to ground. Thus, when the input is high, the output is low (Fig. 3.2b). Both for high and low output voltage, the Coulomb blockade limits the dissipation in this device. In simulations of our device, the steady state dissipation is 5 fW at the output voltages indicated by the arrows in Fig. 3.2a and b. This is many orders of magnitude lower than inverters fabricated with CMOS technology, which typically dissipate 10^{-9} Watts in the steady state.

The device was fabricated on a thermally oxidized silicon substrate using a high-resolution electron beam pattern generator at 100 kV. Each layer of the circuit was defined using a double layer resist and was aligned to prefabricated Pt markers. The bottom layer of the circuit consisted of a 25 nm thick aluminum film that was patterned to form the lower electrodes of the gate capacitors and the load capacitor. To form the dielectric for the capacitors, the sample was heated to 200°C and the aluminum was oxidized in an O₂ plasma at 100 mTorr for 5 minutes. The resulting Al_xO_y layer was 8 nm thick. A second aluminum film was then deposited in a pattern that defined the islands and the leads. The four tunnel junctions were defined in this layer by shadow evaporation.

The device was measured in a dilution refrigerator with a base temperature of 25 mK. All leads were equipped with π -filters at room temperature and copper-powder filters at base temperature. During the first cool down, superconductivity was suppressed using a 1 T magnetic field. Measurements on the individual SET's revealed that the tunnel junctions were all approximately identical with capacitances of $C_j = 280$ aF and resistances of 1.1 M Ω . The input capacitances were $C_{i1} = 800$ aF and $C_{i2}=810$ aF, the tuning gate capacitances C_g were 45 aF, and the stray capacitance C_0 of each island was estimated to be 190 aF. During a second cool, down measurements were done in the superconducting state. All sample parameters remained the same except for the junctions, where the capacitance and resistance changed to $C_j = 155$ aF and R=1.3 M Ω as a result of the thermal cycling.

3.3 Experimental results

3.3.1 Normal state

The conduction of the independent SETs depends on the total charge Q that is induced on the individual islands. This includes contributions from the polarization charges on all capacitors connected to the island and the voltage sources connected to them. When the junction capacitances and resistances are equal,

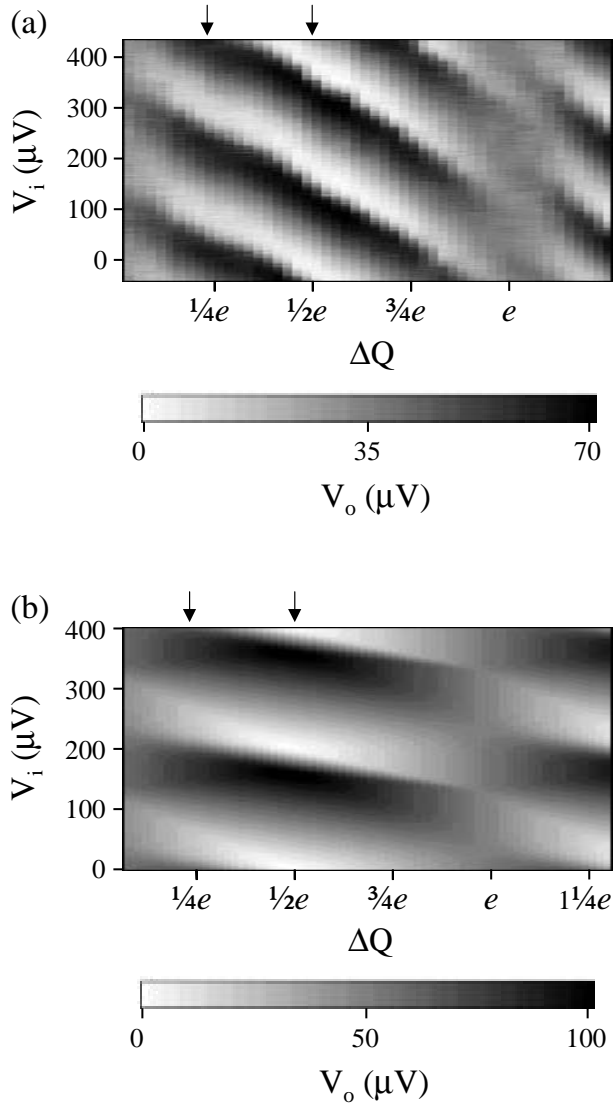


Figure 3.3: (a) The output voltage of the inverter is plotted in grayscale as a function of the input voltage and the induced charge difference between the two islands for $T=30$ mK. (b) Simulation of the output voltage of the inverter as a function of the input voltage and the induced charge difference between the two islands for $T=30$ mK. The arrows indicate where the data for Fig. 3.4 was extracted from Fig. 3.3a and 3.3b. The bias voltage was $V_b = e/C_\Sigma = 100$ μV .

the average induced charge on islands 1 and 2 reduces to [9]

$$Q_1 = C_{i1}V_i + C_gV_{g1} + Q_{01} - \frac{V_b}{2}(C_g + C_0) - \frac{V_o}{2}(C_g + C_0), \quad (3.1)$$

$$Q_2 = C_{i2}V_i + C_gV_{g2} + Q_{02} - \frac{V_o}{2}(C_g + C_0), \quad (3.2)$$

$$\Delta Q = Q_1 - Q_2, \quad (3.3)$$

where Q_{01} and Q_{02} are the background offset charges induced on the respective islands. The input-output characteristics of an inverter can be adequately characterized by ΔQ , the *difference* in induced charge on both islands. Figure 3.3a shows the dependence of the output voltage on V_i and ΔQ . This figure illustrates that the input-output characteristics of the inverter can vary greatly depending on ΔQ . In the region around $\Delta Q = e$, the output is a weak function of the input. When the tuning gates are adjusted so that the induced charges are $e/2$ out of phase, there are large oscillations of the output voltage as the input voltage is varied. Increasing both of the tuning gates simultaneously leaves ΔQ constant but has the same effect as increasing V_i . Because of gate cross capacitances, Fig. 3.3a is skewed with respect to the simulations that are shown in Fig. 3.3b. Simulations of the individual SETs are done using the orthodox theory for single-electron tunnelling. Using an iterative procedure the output voltage V_o was changed until the currents through both transistors were the same.

Figure 3.4 shows input-output characteristics at 30 mK for two different values of ΔQ . The arrows in Fig. 3.3 indicate where the data for Fig. 3.4 was extracted. Note that when the input voltage is low, the output voltage is high and when the input voltage is high, the output voltage is low. To achieve this input-output characteristic, the gate voltages were adjusted manually. At this point there is no procedure known for automatically tuning the gate voltages on-chip for the optimal inverter performance. This is probably the largest problem inhibiting the further development of this sort of logic.

The solid lines in Fig. 3.4 are simulations of the inverter characteristics calculated at 30 mK. For the most part, the orthodox theory fits the measurements. The largest deviations occur at $\Delta Q = e/2$ and either minimal or maximal output voltage. At $\Delta Q = e/2$, the maximal observed output voltage swing is 75% of what is expected from orthodox theory. This is probably due to external noise coupling in via the leads. The device is most sensitive to external noise at these bias conditions. An important consideration for the proper operation of an inverter is that the maximum output voltage swing must be greater than the voltage swing necessary at the input to switch the output from low to high. In other words, the inverter must exhibit voltage gain. The maximum voltage gain that can be achieved in a single-electron transistor is the ratio of the input-gate

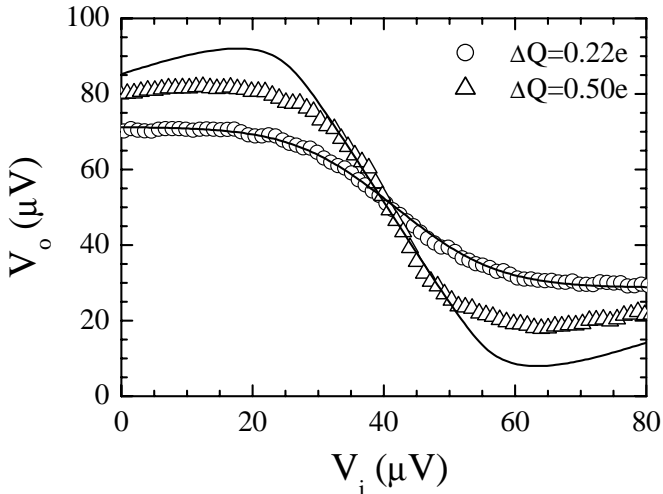


Figure 3.4: The input-output characteristics of the inverter are plotted for two values of the induced charge difference for $T=30$ mK. The solid lines are simulations using the orthodox theory for single-electron tunnelling.

capacitance to the junction capacitance $g_v = C_i/C_j$. In this work, overlap capacitors were used to make relatively large input-gate capacitors. The maximum voltage gain of the inverter in the normal state, which can be determined from the slope of the transitional region in Fig. 3.4, was $g_v = 2.6$.

Figure 3.5 shows the gain of the inverter as a function of temperature. Note that a voltage gain greater than one was attained for temperatures below about 140 mK. In both experiments and simulations the gain decreased significantly at the lowest temperatures. Increasing thermal fluctuations rapidly smear out the onset of sequential tunnelling in a SET, decreasing the output voltage of the inverter. Figure 3.2 shows that at 30 mK the onset of sequential tunnelling is significantly rounded, decreasing the output voltage swing. In general, the gain of an inverter will decrease by approximately 20% at a temperature of $E_C/10k_B$. This corresponds to a temperature of 60 mK in our case. While there have been many reports of single-electron transistors operating at room temperature, those transistors typically have a voltage gain much less than one. Gain is difficult to achieve at high temperatures because the gate capacitance must be made larger than the junction capacitance while making the total capacitance small. Fabricating a room-temperature single-electron transistor with voltage gain is extremely challenging because it almost certainly requires control of the fabrication process

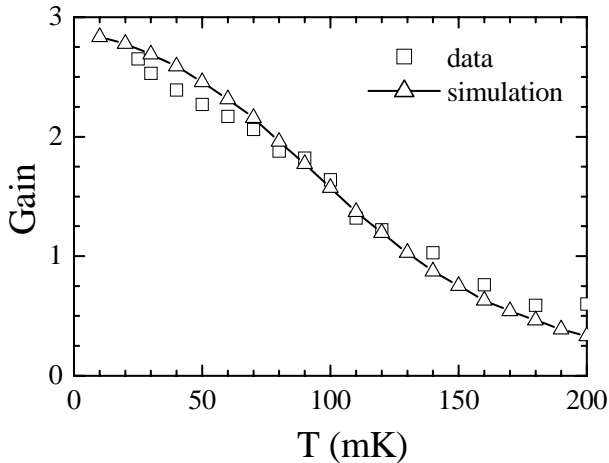


Figure 3.5: The gain of the inverter is plotted as a function of the temperature. The gain decreases below one at 140 mK. The expected temperature dependence of the gain was simulated using the orthodox theory for single-electron tunnelling.

on a nanometer scale in three dimensions.

3.3.2 Superconducting state

As discussed before, one of the major disadvantages of a normal state inverter is its sensitivity to thermal fluctuations. Here we show that the superconducting gap Δ can protect the inverter against thermal fluctuations, yielding much higher operating temperatures. The principles of operation of an inverter in the superconducting state are similar to a normal state inverter, but an extra bias of $2\Delta/e = 400 \mu\text{V}$ has to be applied per junction for the quasiparticles to be excited over the superconducting gap. The optimal voltage bias of a superconducting inverter now is $8\Delta/e + e/C_\Sigma$. Also the output voltage is lifted by $4\Delta/e$ and fluctuates from $4\Delta/e$ to $4\Delta/e + e/C_\Sigma$. Figure 3.6 shows the input-output characteristics of the superconducting inverter at 25 mK. The solid lines are simulations using the superconducting tunnel rate. As in the normal state, the output swing decreases when ΔQ is changed from $0.5e$. Although the experimental curves are more rounded than the simulations, for temperatures below 200 mK this rounding is not due to thermal fluctuations. At a temperature of 200 mK, the characteristics are still similar to Fig. 3.6. The rounding might be caused by either external noise coupling into the leads, or by smearing of the

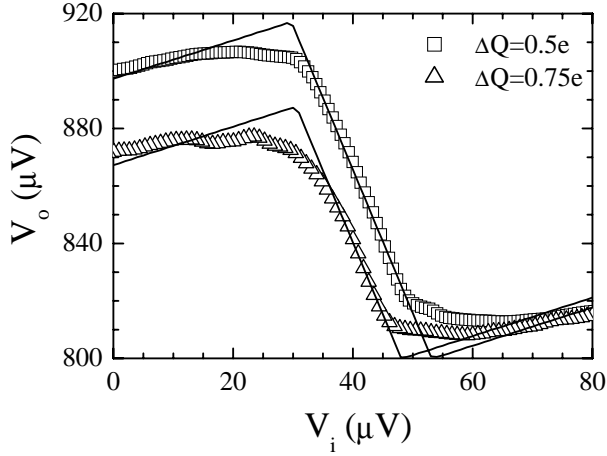


Figure 3.6: The input-output characteristics of the superconducting inverter versus the induced charge difference at 25 mK. The solid lines are simulations using the orthodox theory of single electron tunnelling. The bias voltage was $V_b = 8\Delta + e/C_\Sigma = 1720 \mu\text{V}$

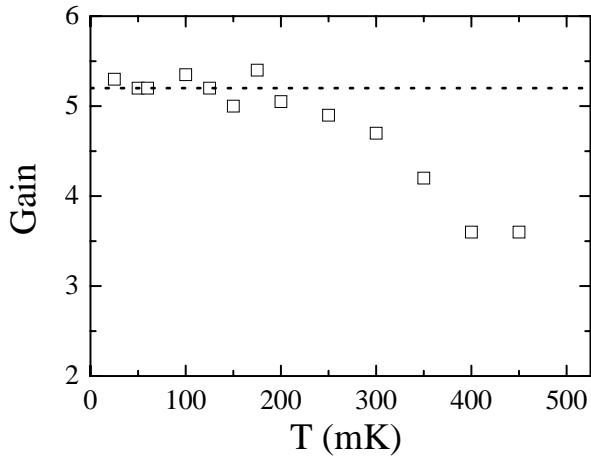


Figure 3.7: The gain of the superconducting inverter is plotted as a function of the temperature. The dotted line denotes the gain as calculated with orthodox theory of single-electron tunnelling.

superconducting gap. Another difference with respect to a normal state inverter is that the gain stays constant for ΔQ differing from 0.5e, only the output voltage swing decreases.

The gain of the superconducting inverter as a function of temperature is shown in Fig. 3.7. The experimental gain stays constant up to 200 mK, decreasing slowly for higher temperatures. The Coulomb blockade is protected from thermal smearing by the superconducting gap. In simulations the gain did not change notably from $g_v = 5.2$ when the temperature was increased to 500 mK. Possibly the superconducting density of states is affected by thermal fluctuations in a way that is not included in our simple model used to calculate the superconducting tunnel rates. The rounding of the gap, as discussed in chapter 4, might be sensitive to temperatures above 200 mK.

3.4 Conclusions

The measurements on this single-electron inverter show that it can operate as it was designed to and that the orthodox theory adequately describes the behavior of the circuit. The voltage gain necessary for the operation of this inverter was achieved by using overlap capacitors in a multilayer circuit. In the normal state the gain rapidly decreases as a function of temperature because the Coulomb blockade is smeared by thermal fluctuations. A maximum gain of 2.6 was reached at 25 mK. Because the superconducting gap protects the inverter from thermal fluctuations, the superconducting inverter still had gain up to 450 mK. Due to thermal cycling, the junctions capacitances decreased and the maximum voltage gain increased to 5.2, staying constant up to 200 mK.

References

- [1] For an overview of Single-electron devices and their applications, see: K. K. Likharev, Proceedings of the IEEE **87** 606 (1999).
- [2] Yu. A. Pashkin, Y. Nakamura, and J.S. Tsai, Appl. Phys. Lett. **76**, 2256 (2000).
- [3] J. R. Tucker, J. Appl. Phys. **72**, 4399 (1992).
- [4] A. N. Korotkov, R. H. Chen, and K. K. Likharev, J. Appl. Phys. **78**, 2520 (1995).

-
- [5] G. Zimmerli, R.L. Kautz, and John M. Martinis, *Appl. Phys. Lett.* **61**, 2616 (1992).
 - [6] R. A. Smith and H. Ahmed, *Appl. Phys. Lett.* **71**, 3838 (1997).
 - [7] C. P. Heij, D. C. Dixon, P. Hadley, and J. E. Mooij, *Appl. Phys. Lett.* **74**, 1042 (1999).
 - [8] Y. Ono, Y. Takahashi, K. Yamazaki, M. Nagase, H. Namatsu, K. Kurihara, and K. Murase, *Appl. Phys. Lett.* **76**, 3121 (2000).
 - [9] See for example Eq. 1.8.

Chapter 4

Charge spectrometry with a strongly coupled superconducting single-electron transistor

C. P. Heij, P. Hadley and J.E. Mooij

We have used a Superconducting Single-Electron Transistor (SSET) as a DC-electrometer that is strongly coupled to the metal island of another SSET. With this set-up, it is possible to directly measure the charge *distribution* on this island. The strong capacitive coupling was achieved by a multilayer fabrication technique that allowed us to make the coupling capacitance bigger than the junction capacitances. Simulations of this system were done using orthodox theory of single-electron tunnelling and showed excellent agreement with the measurements.

4.1 Introduction

When a SSET is used as a standard electrometer, the central island is weakly coupled to another object via a capacitance, much smaller than the electrometer's junction capacitances. The SSET is operated at a bias and gate voltage where the electrometer current is maximally sensitive to changes in the objects charge. With this set-up a resolution of $8 \times 10^{-6} e/\sqrt{\text{Hz}}$ at 10 Hz has been obtained [1]. Because the coupling is weak, only a fraction of the real signal is detected. Consequently the change in electrometer current is very small. We will show that when the

Parts of this chapter were accepted for publication in 'Physical Review B, 2001'.

coupling is strong it is possible to measure the distribution of charge on the object, even though the charge on this object changes much faster than the electrometer's bandwidth. Calculations of the current through single-electron transistors are based on the charge distribution, but this distribution has never been measured directly.

Another way to measure the charge distribution is to monitor the charge in real-time. To monitor the individual electrons passing by, requires a measurement bandwidth of tens of MHz for pA currents. Because of the SSETs high output impedance ($R \gg 2 \times h/e^2 = 52 \text{ k}\Omega$) and the large lead and filtering capacitances ($\approx 1 \text{ nF}$), however, the bandwidth is usually limited to a few hundred Hertz. With the use of cryogenic amplifiers placed in close proximity to the SSET, the output impedance can be lowered to allow a bandwidth of hundreds of kHz [2, 3]. Using the recently developed rf-SET, in principle it is possible in to measure with a resolution of $0.1e$ using a bandwidth of 100 MHz [4]. However, experimental problems are big and have so far limited measurements on high frequency single-electron processes.

First we used a superconducting electrometer that was strongly coupled to the island of a high-ohmic SSET. The electrometer was biased at a small voltage and its tuning gate was used to scan the charge on the neighboring island. These gate traces directly reflect the charge distribution on this island, even though this charge is changing at timescales far outside the electrometers' conventional measurement bandwidth. The measurements are consistent with orthodox theory and this shows that a strongly coupled SSET can be used to directly measure the charge distribution. In a second experiment, we used the same techniques to measure on a 'quantum' SSET whose total resistance is comparable to the quantum resistance. No calculations have been performed to describe transport in such a system, and these measurements are the first to reveal some of its dynamics.

In the first part of this chapter, measurements and simulations of the high-ohmic SSET are presented, followed by a discussion of the electrometer's performance and its operational constraints. Finally we present the measurements on the quantum SSET, and discuss these results.

4.2 Experimental details

A schematic of the device is shown in Fig. 4.1a. The device was fabricated in three layers. The junctions were fabricated using standard shadow evaporation of aluminum. SSET1 has a planar gate capacitor C_{g1} while the gate capacitor C_{g2} is

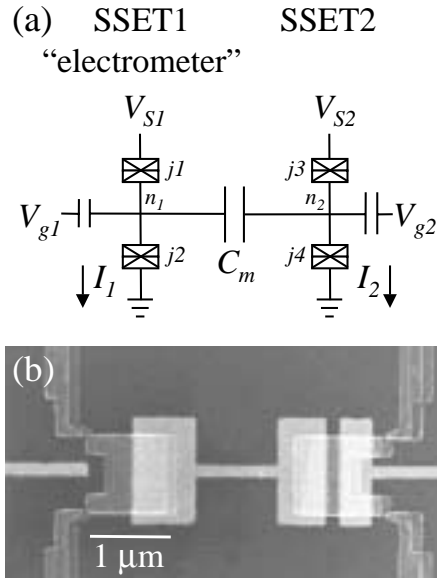


Figure 4.1: (a) Schematic of the circuit. The two junctions on the left form the electrometer (SSET1), whose island is coupled capacitively to the island of a nearby SSET (SSET2). (b) Scanning electron microscope picture of the completed device. The light gray layer is fabricated in gold, the aluminum layer shows up as dark grey. The bottom junctions are larger than the top junctions due to the proximity of a large electrode written $3 \mu\text{m}$ underneath the bottom junctions.

defined as a parallel plate capacitor. Details of the fabrication of a similar device were described in chapter 2. Figure 4.1b shows a SEM picture of the device. The two square islands of the SSETs are coupled via an underlying dumbbell shaped conductor. The coupling conductor itself is an island with a small capacitance, but because the number of electrons on the conductor does not change, it does not add an extra degree of freedom to the system. Consequently we can describe the system by only taking into consideration the excess electrons n_1 and n_2 on the two islands of the SSETs, coupled by a single effective capacitance. The total effective capacitance between the two islands is called C_m . Both SSETs were biased asymmetrically, connected to a voltage source at one side and grounded at the other side. The device was measured in a dilution refrigerator with a base temperature of 10 mK. The leads were equipped with π -filters at room temperature and standard copper-powder filters [6] at base temperature. The effective electron temperature was measured in the normal state by fitting experimentally

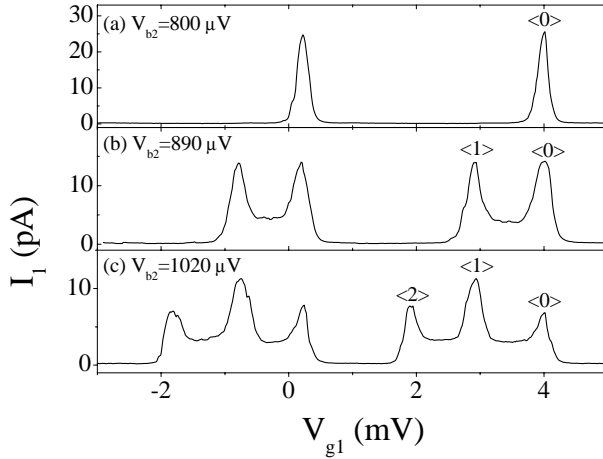


Figure 4.2: Experimental Coulomb traces of the electrometer for different values of V_{b2} while $V_{b1} = 5 \mu\text{V}$, $V_{g2} = 10 \mu\text{V}$ and $T=25 \text{ mK}$. The extra peaks Coulomb peaks in (b) and (c) correspond to the presence of extra electrons on island 2.

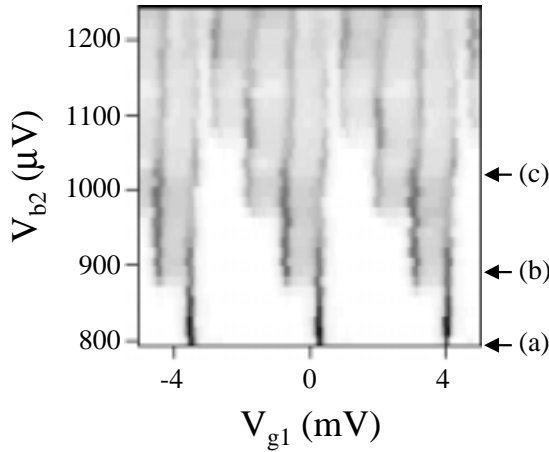


Figure 4.3: Electrometer current versus V_{g1} and V_{b2} . White indicates no current, black indicates a maximum current of 25 pA. The arrows indicate the values of V_{b2} where the traces of Fig. 4.2a-c have been extracted. At $V_{b2} = 1180 \mu\text{V}$ the charge state $\langle 4 \rangle$ becomes populated, but the corresponding peak overlaps with the neighboring set of Coulomb peaks.

	$j1$	$j2$	$j3$	$j4$	C_{g1}	C_{g2}	C_m	$C_{\Sigma 1}$	$C_{\Sigma 2}$
C (fF)	0.135	0.350	0.16	0.40	0.042	0.640	0.450	0.977	1.650
R (M Ω)	3.5	3.5	6.5	6.5	∞	∞	∞	-	-

Table 4.1: Capacitance and resistance values for the circuit parameters as calculated from the stability diagrams and IV characteristics of both SSETs.

obtained Coulomb peaks and yielded an electron temperature of 25 mK. All further measurements were done in the superconducting state, the superconducting gap being $\Delta = 200 \mu\text{eV}$.

4.3 Experimental results; the high-ohmic SSET

Throughout the measurements, the voltage bias of the electrometer was kept constant at $V_{b1} = 805 \mu\text{V}$, just above $4\Delta/e$. The current through the electrometer I_1 was measured as a function of the gate voltage V_{g1} and the bias voltage V_{b2} of the SSET2. The gate voltage V_{g2} was kept constant. Figure 4.2a shows typical Coulomb oscillations of the current through the electrometer. The gate of the electrometer was swept while SSET2 was biased at $800 \mu\text{V}$, the current I_2 being negligibly small. Figure 4.2b shows the same Coulomb trace when $V_{b2} = 890 \mu\text{V}$, above the quasiparticle threshold of SSET2. Surprisingly, the Coulomb peak is split into two peaks, while at even higher bias ($V_{b2} = 1090 \mu\text{V}$) it is split into three. As we will explain in the following section, each extra peak can be attributed to the presence of an extra electron on the second island.

When $V_{b2} = 800 \mu\text{V}$, the current through SSET2 is still negligibly small and the occupation probability of charge state $\langle 0 \rangle$ on island 2 is nearly 1. When V_{b2} is higher than the threshold voltage, a quasiparticle current I_2 will start to flow and the charge n_2 on the island 2 will switch between $\langle 0 \rangle$ and $\langle 1 \rangle$. The presence of an extra electron on island 2 will induce a fraction of an electron on coupling capacitor C_m . By writing down the total charge on both islands as a function of the capacitances and the island potentials, one can show that this fraction is $C_m/C_{\Sigma 2}$, where $C_{\Sigma 2}$ is the sum of all capacitors connected directly to island 2. Table 4.1 gives the capacitance and resistance values of all the circuit elements. With this table, we can calculate that the charge induced on capacitor C_m is $0.27 e$. This results in the extra Coulomb peak (labelled $\langle 1 \rangle$) shifted $-e/C_{g1} * 0.27 = -1.04 \text{ mV}$ with respect to the peak labelled $\langle 0 \rangle$ in Fig. 4.2b. When V_{b2} is increased even more, charge state $\langle 2 \rangle$ is also populated on island 2 and three peaks appear (Fig. 4.2c). Figure 4.3 shows the Coulomb traces of the electrometer current I_1 in grayscale versus the bias V_{b2} . One can clearly see that

	I. experiments			II. simulations			III. SSET1 'off'		
V_{b2} (μV)	p_0	p_1	p_2	p_0	p_1	p_2	p_0	p_1	p_2
890	0.50	0.50	0	0.50	0.50	0	0.50	0.50	0
1020	0.28	0.43	0.29	0.28	0.42	0.30	0.29	0.40	0.31

Table 4.2: The population of first three charge states on island 2, as calculated from the peak heights in the experiments (Fig. 4.2) and the simulations (Fig. 4.4). The undisturbed population is determined by a calculation of the population matrix P_{ij} of Eq. 4.2a when the electrometer is switched off ($V_{b1} = 800 \mu\text{V}$).

consecutive charge states become populated with increasing V_{b2} . The average bias voltage difference between successive charge states on island 2 is $2E_{C2}/e$, where E_{C2} is the charging energy of island 2. The charge state $\langle 4 \rangle$ becomes populated at $V_{b2} = 1180 \mu\text{V}$ and induces $1.08 e$ on island 1. The corresponding peak in the Coulomb trace of the electrometer overlaps with the next set of Coulomb peaks, limiting the number of observable charge states to four with these circuit parameters.

By measuring Coulomb oscillations, the electrometer can be used to directly resolve the average population of charge states on a nearby island, even though the charge on this island changes on a nanosecond timescale. At Coulomb peak $\langle j \rangle$, current can only flow through the electrometer when the island 2 is in charge state $\langle j \rangle$. The fraction of the time that island 2 spends in charge state $\langle j \rangle$ is equal to the relative peak height defined by

$$p_i = \frac{I_{p,i}}{\sum_j I_{p,j}}, \quad (4.1)$$

where $I_{p,j}$ is the peak height of the Coulomb peak corresponding to the charge state $\langle j \rangle$ on island 2. Simulations confirm that the height of the individual peaks reflects the exact population of the corresponding charge state.

The relative peak heights of the Coulomb traces in Fig. 4.2b,c are calculated and shown in column I of Table 4.2. They closely match the occupation of the various charge states as calculated in the simulations for identical bias conditions, shown in column II. Also, for bias conditions other than $V_{b2} = 890 \mu\text{V}$ and $1020 \mu\text{V}$, the simulated relative peak heights closely match the experimental ones. This shows that a strongly coupled SSET can be used to quantitatively measure the charge *distribution* on a nearby object.

4.3.1 Master equation simulations

The current through both SSETs was calculated using a master equation analysis. By solving the master equation we can calculate the occupation probabilities of the various charge states. Using the general master equation 1.3 for an n -island device, the master equation for this two island system is

$$\frac{\partial P_{ij}}{\partial t} = \sum_{kl \neq ij} (P_{kl} \Gamma_{kl \rightarrow ij} - P_{ij} \Gamma_{ij \rightarrow kl}), \quad (4.2a)$$

$$\sum_{ij} P_{ij} = 1, \quad (4.2b)$$

where P_{ij} is the probability that the system has i excess electrons on island 1 and j excess electrons on island 2. Γ denotes the transition rate between different charge states. In the stationary state, P_{ij} does not change and the left hand side of Eq. 4.2a is zero. The first term on the right describes the population of charge state ij from charge state kl while the second term describes the depopulation of charge state ij to charge state kl . We neglect co-tunnelling processes and Γ only is non-zero when either $i = k \pm 1$ or $j = l \pm 1$. Furthermore we only take into account a maximum of five charge states per island. Eqs 4.2a and 4.2b can be combined into a single matrix equation, which is solved numerically for P_{ij} .

The superconducting tunnel rates Γ were then determined with Fermi's Golden Rule using the superconducting density of states and the free energy difference ΔF of a tunnelling event [7, 8]. ΔF is the sum of the change in electrostatic energy plus the work done by the voltage sources. With help of Eq. 1.5 the total electrostatic energy of the system can be written as

$$E(n_1, n_2) = E_{C1}(n_{g1} + n_1)^2 + E_{C2}(n_{g2} + n_2)^2 + E_m(n_{g1} + n_1)(n_{g2} + n_2), \quad (4.3a)$$

$$E_{C1} = \frac{e^2 C_{2\Sigma}}{2(C_{\Sigma1} C_{\Sigma2} - C_m^2)} = 95 \mu eV, \quad (4.3b)$$

$$E_{C2} = \frac{e^2 C_{1\Sigma}}{2(C_{\Sigma1} C_{\Sigma2} - C_m^2)} = 53 \mu eV, \quad (4.3c)$$

$$E_m = \frac{e^2 C_m}{C_{\Sigma1} C_{\Sigma2} - C_m^2} = 51 \mu eV, \quad (4.3d)$$

where n_{g1} and n_{g2} are the normalized charges induced on the islands by the all voltage sources and the background charge, n_1 and n_2 are the excess number of electrons on the islands and $C_{\Sigma1}$ and $C_{\Sigma2}$ are the sum of all capacitors directly connected to the respective islands. The electrostatic energy has three contributions, the charging energies of the separate SSETs (Eqs 4.3b and 4.3c) and the

coupling energy E_m , which describes the electrostatic interaction between both SSETs.

The total current I_1 is equal to the current through the single junction $j1$ or $j2$

$$I_1 = e \sum_{ij} P_{ij} (\Gamma_{ij\rightarrow} - \Gamma_{ij\leftarrow}), \quad (4.4)$$

where $\Gamma_{ij\rightarrow}$ and $\Gamma_{ij\leftarrow}$ are the forward and backward tunnelling rate across the junction.

4.3.2 Simulation results

In Fig. 4.4, the current through the electrometer has been calculated for the same bias conditions as Fig. 4.2. One can clearly see the extra Coulomb peaks appear when the bias voltage V_{b2} is increased. The absolute peak height of the experiments is about 60% of the peak height in the simulations. This can be accounted for by the rounding of the superconducting gap. Instead of the discontinuous jump in quasiparticle current through a superconducting junction at $2\Delta/e$, in real experiments, the current increases with a non-zero slope. In these experiments, the differential resistance in this regime is about 5% of the high bias junction resistance. For a bias voltage of $V_{b1} = 805 \mu\text{V}$, only $5 \mu\text{V}$ above $4\Delta/e$, this has two consequences. First, the Coulomb peaks have a more triangular form as can be seen in Fig. 4.2, and second, the Coulomb peak height is smaller than in the simulations where the rounding has not been taken into account. Simulations where the rounding of the gap was taken into account with a simple model showed that the rounding of the gap does not change the relative height of the peaks, it merely decreases the overall current.

For the simulated Coulomb traces of Fig. 4.4, the relative peak heights as specified by Eq. 4.1 are given in Table 4.2. The experiments closely match the simulated values. The relative peak heights in simulations are slightly different though from the occupation of the charge states on island 2 when the electrometer is switched "off" ($V_{b2} = 800 \mu\text{V}$). Column three of Table 4.2 shows the undisturbed occupancies of the three charge states as determined from the population matrix P_{ij} . As can be seen from Table 4.2, the bias of the electrometer has a small back action on the occupation of charge states on island 2. For the bias range of Fig. 4.5, it can be shown that the back action of this electrometer changes the occupancies of the various charge states by a maximum of 5%.

Figure 4.5 is the simulated equivalent of Fig. 4.3. The extra peaks appear in Fig. 4.5 at exactly the same bias conditions as in Fig. 4.3, demonstrating the close agreement between experiments and simulations. Another feature that

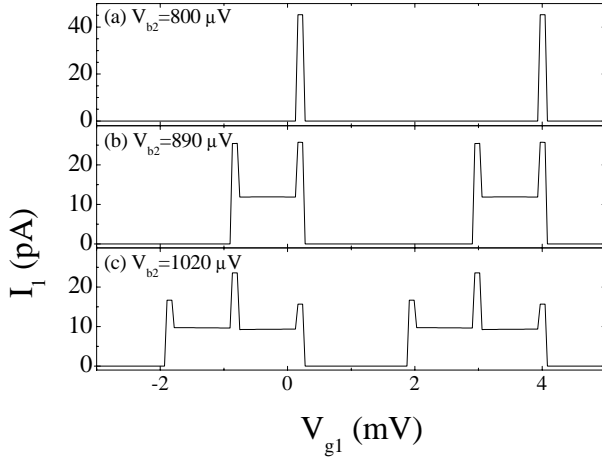


Figure 4.4: Simulations of Coulomb traces of the electrometer for different values of V_{b2} . $V_{b1} = 805 \mu\text{V}$, $V_{g2} = 10 \mu\text{V}$ and $T=25 \text{ mK}$.

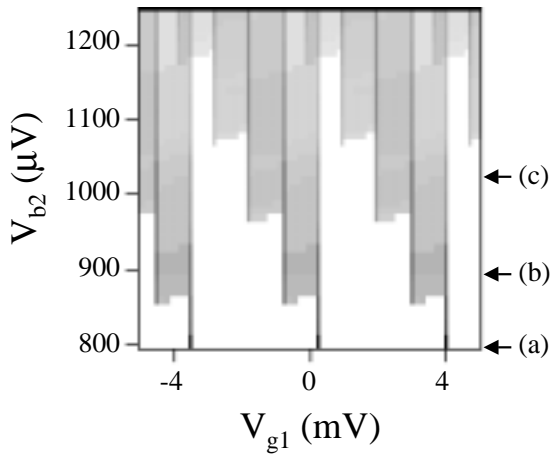


Figure 4.5: Simulation of the electrometer current versus V_{g1} and V_{b2} . White indicates no current, black indicates a current of 45 pA. The arrows indicate the values of V_{b2} where the traces of Fig. 4.4a-c have been extracted.

clearly shows up in the simulations as well as the measurements is the existence of a current plateau in between the neighboring Coulomb peaks. Under these bias conditions, the electron-tunnelling through both SSETs is correlated. This effect has been discussed for coupled 1D arrays of tunnel junctions, but has never been demonstrated experimentally [9, 10]. The details of this effect will be discussed below.

4.3.3 Operational constraints

Bias voltage

The ability to determine the position and the height of the extra Coulomb peaks gives constraints on the bias conditions. In general, the width of the peaks has to be smaller than the separation between adjacent peaks. In the superconducting state, the width of Coulomb peaks is almost independent of temperature for $k_B T < 0.5\Delta$ and depends linearly on the applied bias. This constraint can be rewritten as:

$$eV_{b1} - 4\Delta < E_m. \quad (4.5)$$

This simply states that the energy associated with the voltage bias has to be smaller than the coupling energy. Because of the quasiparticle threshold at $4\Delta/e$, this constraints the bias voltage to $800 \mu\text{V} < V_{b1} < 851 \mu\text{V}$ for this sample. The quasiparticle rate is almost independent of the bias in this bias window and simulations indicate that the back action of the electrometer is also constant. If we take into account the rounding of the gap and the experimental current noise, $V_{b2} = 805 \mu\text{V}$ is about the optimal bias voltage, combining an acceptable signal to noise ratio with a reasonably small width of the Coulomb peaks. With the current sample parameters, we are limited to the observation of a maximum of four charge states on the neighboring island. We estimate that it is feasible to observe at least seven different charge states, when the coupling capacitance is lowered to 190 aF, while keeping the other sample parameters constant.

Current plateau

Both Fig. 4.2 and 4.4 clearly show the existence of a current plateau in between the accompanying Coulomb peaks. In order to be able to measure the relative peak heights, this plateau current should not exceed the Coulomb peak current and therefore its mechanism should be understood. The mechanism can be most easily explained when the number of occupied electron states on island 2 is limited to two and under the assumption that the tunnel rates in SSET1 are much

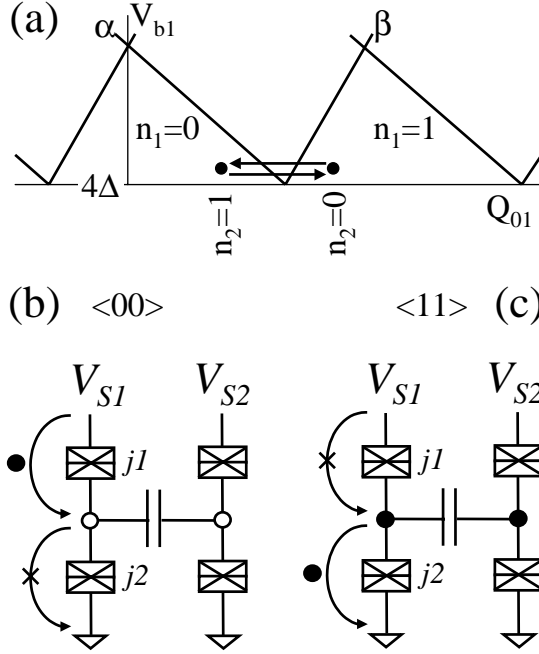


Figure 4.6: (a) Schematic of the quasiparticle thresholds of SSET1 above $V_{b1} = 4\Delta/e$, shown as thick lines. The positions of the dots denote the effective background charge induced by the absence or presence of an extra electron on island 2. (b) Visualization of the possible tunnelling events on island 1. When the system is in charge state $\langle 00 \rangle$ it will decay to $\langle 10 \rangle$ by an electron tunnelling through junction $j1$. Electron tunnelling through junction $j2$ is energetically unfavorable, just like electrons tunnelling upward. (c) In a similar way charge state $\langle 11 \rangle$ decays to $\langle 01 \rangle$.

larger than those in SSET2. Figure 4.6a schematically displays the quasiparticle thresholds for SSET1. The position of the dots denotes the effective background charge when the charge state of island 2 is $\langle 0 \rangle$ (right dot) and $\langle 1 \rangle$ (left dot). The position of the dots relative to each other is fixed. The bias voltage V_{b1} and hence the dots lie just above $4\Delta/e$. With the gate voltage V_{g1} the position of both dots can be shifted along the Q_{01} axis. If the gate voltage positions one of the two dots above both quasiparticle thresholds α and β this leads to current in the form of a Coulomb peak. If the dots are positioned as depicted in Fig. 4.6a there is an additional mechanism that will carry current.

The charge states with the lowest energy are now $\langle 10 \rangle$ and $\langle 01 \rangle$. If a current is forced to flow through SSET 2 by biasing it above its quasiparticle threshold,

the following current cycle is most probable: If we start with charge state $\langle 00 \rangle$ it is only favorable for electrons to tunnel onto islands 1 or 2 via the top junctions. Because we assume that the tunnel rates in SSET1 are much larger than those in SSET2, an electron will most probably tunnel through junction j_1 first, as shown in Fig. 4.6b. Now the system is in the charge state $\langle 10 \rangle$ which is stable for electron tunnelling in SSET1. After some time the bias voltage V_{b2} forces an electron on island 2 and the system is in state $\langle 11 \rangle$. As can be seen in Fig. 4.6c this state decays to $\langle 01 \rangle$ through junction j_2 , again assuming the tunnel rates are much higher in SSET1. This charge state is also stable for electron tunnelling in SSET1. The cycle is completed when the electron is forced off island 2 and the system is back in charge state $\langle 00 \rangle$. The cycle of one electron tunnelling through SSET2 has transported another electron through SSET1 making $I_1 = I_2$. This cycle is possible for all gate voltages where both the position of $n_2 = \langle 1 \rangle$ lies below quasiparticle threshold α and position of $n_2 = \langle 0 \rangle$ lies below quasiparticle threshold β . This gives rise to a current plateau exactly in between the Coulomb peaks attributed to the both charge states.

In this sample the resistances of SSET1 and SSET2 and hence the tunnel rates differ by only a factor of two. This means that cycles can be missed, for example if state $\langle 00 \rangle$ decays to $\langle 01 \rangle$, the system is forced to $\langle 00 \rangle$. An electron has been transported through SSET2, without giving rise to current in SSET1. The general equation for the relation between I_1 and I_2 can be deduced by analytically solving the master equation under the assumption that only the four charge states $\langle 00 \rangle$, $\langle 10 \rangle$, $\langle 01 \rangle$ and $\langle 11 \rangle$ need to be considered. If we assume that the tunnel rates through junction j_1 and j_2 are equal and called Γ_1 , as well as those through j_3 and j_4 are equal and called Γ_2 this yields

$$I_1 = \frac{\Gamma_1}{\Gamma_1 + 2\Gamma_2} I_2. \quad (4.6)$$

By deriving the expressions for the Coulomb peak current, it can be shown that the peak currents are always sufficiently larger than the plateau current, making it possible to adequately determine the relative peak heights. When the number of occupied charge states on island 2 is larger than two, the mechanism leading to the current plateaus is similar, but different combinations of charge states might be stable and Eq. 4.6 will be modified. Again though, the plateau current is always smaller than the Coulomb peaks adjacent to the particular current plateau.

To check the validity of Eq. 4.6, we deduced the values of Γ_1 and Γ_2 from the peak heights of single Coulomb peaks, for example from Fig. 4.2a. The bias dependent ratio $\frac{I_1}{I_2}$ that follows from Eq. 4.6 agreed with the experimentally measured current values.

Normal state

We also studied the performance of the electrometer in the normal state. In the normal state, however, the Coulomb peaks are very sensitive to thermal fluctuations. The thermal broadening of the Coulomb peaks at 70 mK was enough to merge the adjacent Coulomb peaks, making an accurate determination of the relative peak heights impossible. Additionally, due to a mechanism similar to the one leading to the current plateau in the superconducting state, the adjacent Coulomb peaks merged at 30 mK in the normal state, making the normal state operation of this electrometer impractical.

4.4 Experimental results; the quantum SSET

When the resistance of a normal state single-electron transistor is of the order of the quantum resistance, quantum fluctuations of the island charge will suppress single-electron effects. In this regime, quasiparticle transport has been studied in both experiments and simulations and predictions are in good agreement with the data [11, 12]. In the superconducting state, a combination of Cooper pair and single-electron tunnelling determines the transport at low bias ($V_b < 4\Delta/e$). This has been studied extensively in the regime where $E_J \ll E_C$ [14, 15, 16]. In this sample $E_J/E_C = 0.8$ and charge fluctuations are large. To our knowledge, there are no adequate calculations of the current through a SSET in this regime.

Using the same set-up as shown in Fig. 4.1, we measured on a quantum SSET with a total resistance of 21 k Ω . The circuit parameters are given in Table 4.3, the total capacitance of the quantum SSET is hard to determine because of the small resistance and relatively large capacitance. Figure 4.7 shows the current-voltage characteristic of the quantum SSET. It was voltage biased and shows a peak in the current at a voltage of 490 μ V. The peak position does not move with the gate voltage and the peak current is only weakly modulated (≤ 0.25 nA) by the gate voltage. Also, no clear Coulomb blockade effects are visible above 800 μ V; the current is only weakly modulated (≤ 0.12 nA) by the gate voltage. Other SSETs with similar resistances (10 – 50 k Ω) showed the same current-voltage characteristics and charging effects were also greatly suppressed [13]. In samples with resistances larger than 50 k Ω there are usually two separate peaks, whose

	C_m	$C_{\Sigma 1}$	$C_{\Sigma 2}$	C_{g1}	C_{g2}		$R_{\Sigma 1}$	$R_{\Sigma 2}$
C (fF)	0.22	1.1	~ 2	0.036	0.038	R (k Ω)	21	85

Table 4.3: Circuit parameters of the electrometer coupled to a quantum SSET.

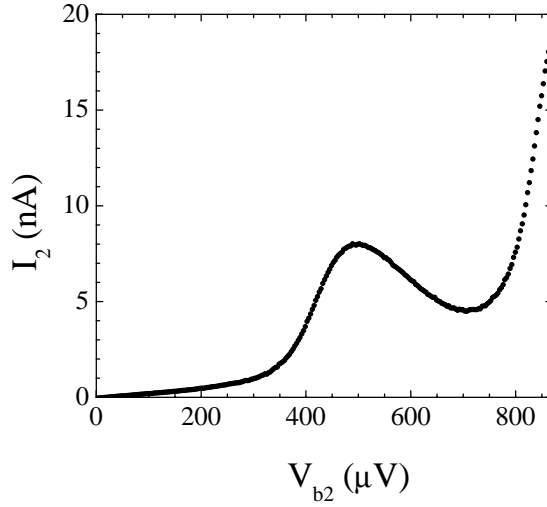


Figure 4.7: The current-voltage characteristic of the quantum SSET at 25 mK. The maximum gate modulation is 0.25 nA at 420 μV .

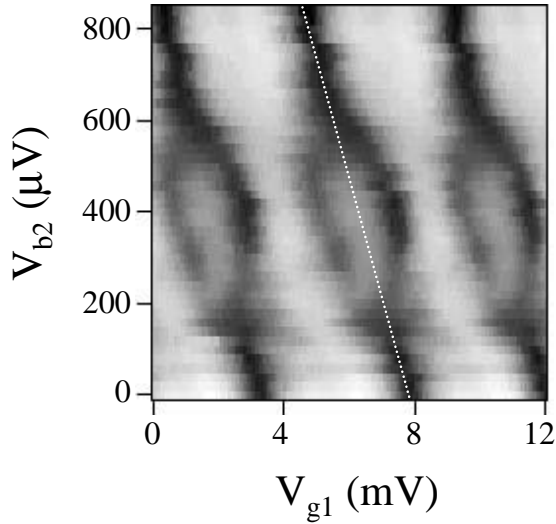


Figure 4.8: The gate traces of the electrometer versus the bias voltage of the quantum SSET at $V_{g2} = 200 \text{ mV}$. White indicates no current, black indicates a current of 1.4 nA. The white dotted line represents the regular shift of the peaks due to cross talk of the bias voltage V_{b2} to island of the electrometer.

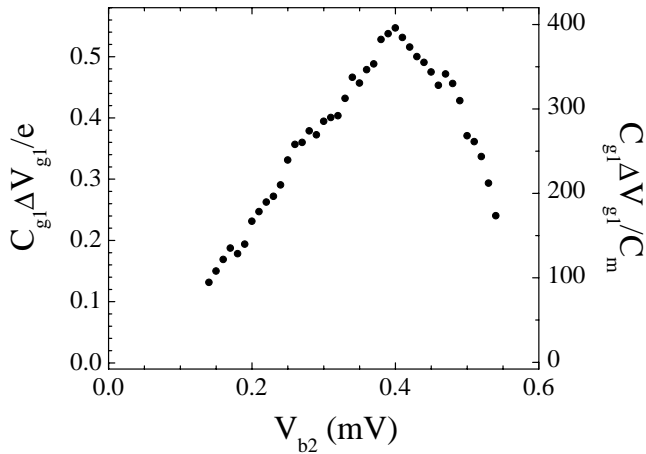


Figure 4.9: Distance between accompanying Coulomb peaks versus V_{b2} as obtained from the traces in Fig. 4.8. The splitting could only be determined in a limited range of V_{b2} , as the two peaks merge into one if their splitting is equal to their width, $\sim 0.2e$.

position depends on the gate voltage. These peaks are the regular Josephson quasiparticle cycle peaks and the peaks are located at bias voltages between $2\Delta/e + E_C/e$ and $2\Delta/e + 3E_C/e$. The peak of Fig. 4.7 is located in the middle of this range at $490 \mu\text{V}$, close to $2\Delta/e + 2E_C/e = 480 \mu\text{V}$ for this particular sample.

The electrometer had a resistance of $85 k\Omega$, high enough to reasonably suppress cotunnelling effects, and a total capacitance of 1.1 fF , small enough to exhibit clear charging effects like the Coulomb blockade. It was biased at $810 \mu\text{V}$, just above the quasiparticle threshold and gate traces were recorded versus the voltage bias V_{b2} of the quantum SSET. Figure 4.8 shows the electrometer current in grayscale. As the bias V_{b2} was increased, the electrometers' Coulomb peak splits in two, reaching a maximum splitting of $C_{g1} \Delta V_{g1} / e = 0.55e$ at $V_{b2} = 400 \mu\text{V}$. In contrast with the experiments described in the first part of this chapter, the splitting is not constant, but depends on the bias of the quantum SSET. Because charge fluctuations on the island of the quantum SSET are large, the peaks might not reflect two distinct charge states, but rather two states with a different potential of the quantum SSETs' island. If we call the potentials of these two states ϕ_0 and ϕ_1 , the charge both states induce on capacitor C_m differs by $(\phi_1 - \phi_0)C_m$. For example, at $V_{b2} = 400 \mu\text{V}$ the splitting of $0.55e$ translates to a potential difference of around $400 \mu\text{V}$. If we assume the average potential on the island of the quantum SSET is $V_{b2}/2$, $\phi_0 \approx 0 \mu\text{V}$ and $\phi_1 \approx 400 \mu\text{V}$. This suggests that the quantum SSET switches between two states where either the

voltage is very small over the top junction while almost all the bias voltage drops across the bottom junction, or vice versa. Figure 4.9 shows the splitting as a function of the bias voltage V_{b2} . As the splitting increases almost linearly with V_{b2} , the above argument holds for $0 \leq V_{b2} \leq 400 \mu\text{V}$.

At very small voltage bias, transport through a single Josephson junction is dominated by coherent or incoherent tunnelling of Cooper pairs. The current-voltage characteristics depend non-trivially on the environmental impedance and the ratio E_J/E_C [17, 18]. In the case of the quantum SSET, the environmental impedance that one junction 'sees' is dominated by the impedance of other junction, which on its turn depends on the voltage bias over this junction. At higher bias, transport through a single junction will be dominated by tunnelling of quasiparticles. Theoretical calculations have to be performed to understand how these two processes influence each other and how they are combined in a SSET in this specific regime of E_J/E_C .

4.5 Conclusions

First we have used a SSET as an electrometer to measure the charge distribution on a neighboring island. The presence of an extra electron on a neighboring island split the Coulomb peaks of the SSET. The relative height of these peaks directly translates to the occupation of the associated charge state. In between the neighboring Coulomb peaks the current is carried by correlated tunnelling of electrons through both SSETs. If the electrometer is coupled to a SSET with a low resistance, the Coulomb peaks seem to reflect states with a different potential. A better understanding of the processes in such a quantum SSET is needed to fully understand the data.

4.6 Acknowledgements

We thank K. K. Likharev for illuminating the basic mechanism leading to the current plateau and David Dixon for assistance with the experiments.

References

- [1] V. A. Krupenin, D. E. Presnov, A. B. Zorin, and J. Niemeyer, *J. Low Temp. Phys.* **118**, 287 (2000).

-
- [2] E. H. Visscher, J. Lindeman, S. M. Verbrugh, P. Hadley, J. E. Mooij and W. van der Vleuten, *Appl. Phys. Lett.* **68**, 2014 (1996).
- [3] J. Petterson, P. Wahlgren, P. Delsing, D. B. Haviland, T. Claeson, N. Rorsman and H. Zirath, *Phys. Rev. B* **53**, 13272 (1996).
- [4] R. J. Schoelkopf, P. Wahlgren, A. A. Kozhevnikov, P. Delsing, D. E. Prober, *Science* **280**, 1238 (1998).
- [5] C. P. Heij, D. C. Dixon, P. Hadley, and J. E. Mooij, *Appl. Phys. Lett.* **74**, 1042 (1999).
- [6] J. M. Martinis, M. H. Devoret and J. Clarke, *Phys. Rev. B* **35**, 4682 (1987).
- [7] See for example M. Tinkham, *Introduction to Superconductivity* (McGraw-Hill, New York, 1996), p. 77, second edition.
- [8] Using Fermi's golden rule we numerically calculate the rate assuming the BCS density of states that is proportional to $\frac{E}{(E^2 - \Delta^2)^{\frac{1}{2}}}$.
- [9] D. V. Averin, A. N. Korotkov and Yu. V. Nazarov, *Phys. Rev. Lett.* **66**, 2818 (1991).
- [10] M. Matters, J. J. Versluys and J.E. Mooij, *Phys. Rev. Lett.* **78**, 2469 (1997).
- [11] P. Joyez, V. Bouchiat, D. Esteve, C. Urbina, and M. H. Devoret, *Phys. Rev. Lett.* **79**, 1349 (1997).
- [12] J. König, H Schoeller, and G. Schön, *Phys. Rev. Lett.* **78**, 4482 (1997).
- [13] Measurements on single SSETs with junction capacitances similar to this quantum SSET.
- [14] A. Maassen van den Brink, Gerd Schön, and L. J. Geerligs, *Phys. Rev. Lett.* **67**, 3030 (1991).
- [15] J. Siewert and Gerd Schön, *Phys. Rev. B* **54**, 7421 (1996).
- [16] Y. Nakamura, C. D. Chen, and J. S. Tsai, *Phys. Rev. B* **53**, 8234 (1996).
- [17] D. V. Averin, Yu. V. Nazarov, and A. A. Odintsov, *Physica B* **165&166**, 945 (1990).
- [18] G. -L. Ingold, H. Grabert, and U. Eberhardt, *Phys. Rev. B* **50**, 395 (1994).

Chapter 5

Superposition of charge states in a system of two capacitively coupled superconducting islands

C. P. Heij, D. C. Dixon, C. H. van der Wal,
P. Hadley and J.E. Mooij

We investigate the ground state properties of a system containing two superconducting islands. The islands are capacitively coupled by an underlying superconductor that is electrically isolated from the islands. We show that the ground state of the system is a superposition of charge states, even though the islands cannot exchange charge carriers. The ground state of the system is probed by measuring the switching current of a Bloch transistor containing one of the islands. Simulations based on superpositions of charge states on both islands show good agreement with the experiments. The ability to coherently couple different circuit elements is one of the prerequisites necessary for quantum computation in this kind of system.

5.1 Introduction

Quantum coherence in artificially fabricated structures has received much attention lately largely due to the interest in performing quantum computation in such systems. If quantum states can be manipulated in a artificially fabricated circuit, there is hope that the circuit could be increased in complexity to a size where it may be able to perform useful functions. Quantum coherence in fabricated structures has been discussed for the charge states in quantum dots [1] and for nuclear spin states of impurity atoms embedded in silicon [2]. Measurements

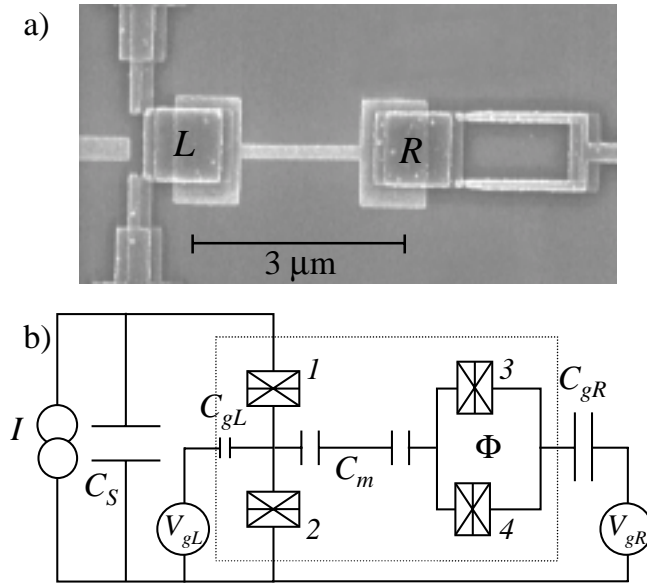


Figure 5.1: (a) A scanning electron microscope photograph of the device shows the Bloch transistor on the left and on the right the Cooper pair box in the form of a superconducting loop. (b) The schematic circuit diagram shows how the sample was embedded in the circuit. The dotted line in the diagram indicates the part of the circuit that can be seen in the SEM photo.

have been performed using charge states on a single superconducting island [3, 4] and flux states in a circuit containing a superconducting loop [5, 6, 7]. In this chapter, we show that the ground state of a system containing *two* capacitively coupled superconducting islands is a superposition of spatially distinct charge states. Quantum fluctuations of the charge on both islands are coupled through a micrometer-sized wire. Such a coupling is a prerequisite for a controlled-NOT gate in this type of circuit.

5.2 Experimental details

Figure 5.1 shows a scanning electron microscope (SEM) photo of the sample and the circuit schematic. The two square superconducting islands labelled L and R play a central role in this circuit. They are spaced $3 \mu\text{m}$ apart and are coupled by two capacitors in series. There is no exchange of charge carriers between

the two superconducting islands; the interaction between the islands is purely electrostatic. Each island can exchange charge with its superconducting leads through small capacitance Josephson junctions. Together with the leads and the left gate electrode the island L forms a Bloch transistor that was current-biased by an external current source. Single Bloch transistors have been studied in detail and their behavior is well understood [8, 9, 10, 11]. The leads of island R are joined in a small loop, transforming the island into a Cooper pair box with tunable Josephson energy, one of the promising candidates for the realization of a charge qubit [3, 12].

The quantum state of a Bloch transistor and a Cooper pair box can be described by the number of excess Cooper pairs n on the island. The ground state of these devices is a superposition of charge states $|n\rangle$. The ground state depends on the charging energy of the island and the Josephson coupling to the leads. The effective charging energy can be tuned by the gate potential and for two parallel junctions, the effective Josephson energy can be tuned by the magnetic flux threading the loop. If the islands of a Bloch transistor and a Cooper pair box are coupled, the state of the circuit can be described by the charge states of the two islands, $|n_L n_R\rangle$. Here n_L is the number of excess Cooper pairs on the left island and n_R is the number of excess Cooper pairs on the right island. Our results demonstrate that the ground state is a superposition of charge states $|n_L n_R\rangle$.

The switching current of a Bloch transistor is related to the quantum fluctuations of the charge on that island; The larger the fluctuations of the charge, the higher the switching current will be. Due to Coulomb repulsion, the charge fluctuations of both devices are correlated and the switching current depends on the state of both islands. We studied the switching current as a function of both gates charges and the flux threading the loop, and compare this to a model where one assumes a single collective ground state for the combined macroscopic system.

The device was fabricated on a thermally oxidized silicon substrate using a high-resolution electron beam pattern generator at 100 kV. Each layer of the circuit was defined using a double layer resist and was aligned to prefabricated Pt markers. The bottom layer of the circuit consisted of a 25 nm thick aluminum film that was patterned to form the lower electrodes of the coupling capacitors and the shunt capacitor C_S . The aluminum was then oxidized by heating it to 200°C in an O_2 plasma at 100 mTorr for 5 minutes. The resulting Al_xO_y formed an 8 nm thick dielectric layer for the capacitors. The insulating properties of this oxide were tested by fabricating a 1×1 mm² Al/ Al_xO_y /Al overlap capacitor which showed no leakage ($R > 10$ G Ω) for voltages up to 6 V. The islands deposited

in the second aluminum layer form the top electrodes of the capacitors. The coupling capacitors can be seen in the SEM photo where the two square islands overlap the dumbbell-shaped structure in the middle of the photo. The total capacitance C_m of the two coupling capacitors in series was 2 fF. A 120 pF shunt capacitor C_S parallel to the Bloch transistor and a 5 pF capacitor connected to the loop were similarly defined but are not visible in the SEM photo. The shunt capacitor C_S protects the device against electrostatic discharge and suppresses voltage fluctuations across the transistor. The tunnel junctions were formed by shadow evaporation. All the junctions were defined to be equal. The series resistance of the two junctions in the transistor was 18 k Ω . From the current-voltage characteristics and the size observed in the SEM photos, the junction capacitances were estimated to be $C = 1$ fF. The area of the loop was $1.7 \mu\text{m}^2$, giving rise to a magnetic field periodicity of 1.2 mT. The product of the inductance of the loop times the critical current of the junctions is much less than a flux quantum, $LI_c \ll \Phi_0$, so that quantum fluctuations of the flux in the loop were very small and could be neglected. Furthermore, $C_{gL} = 40$ aF and the effective gate capacitance C_{gR} to island R was 2 fF; the effective gate capacitance is the series capacitance of the two Josephson junctions and the 5 pF gate capacitor. The normalized gate charge is defined as $n_g = C_g V_g / 2e$.

The sample was mounted in a microwave tight copper box connected to the mixing chamber of a dilution refrigerator with a base temperature of 5 mK. All of the measurement leads were filtered using π -filters at room temperature and copper-powder low-pass filters at the mixing chamber. The current through the sample was ramped with a rate of 1.6×10^{-5} A/s. The voltage over the sample was measured in a four-probe configuration using dedicated electronics.

5.3 Experimental results

The current-voltage characteristics of the Bloch transistor SET show a supercurrent branch around zero voltage. When the Bloch transistor was current biased, the system remained on the supercurrent branch until a certain bias current was exceeded. There was then a discontinuous jump in the voltage from nearly zero voltage on the supercurrent branch to a voltage of about $2\Delta/e$, where Δ is the superconducting gap of aluminum, 200 μeV . The switching current was defined as the current where the voltage over the sample exceeded 1 μV . A sample-and-hold circuit read out the switching current at a rate of 20 Hz. The supercurrent was $2e$ periodic in the induced gate charges at temperatures below 190 mK. The latter temperature being the critical odd-even temperature. Figure 5.2 shows the

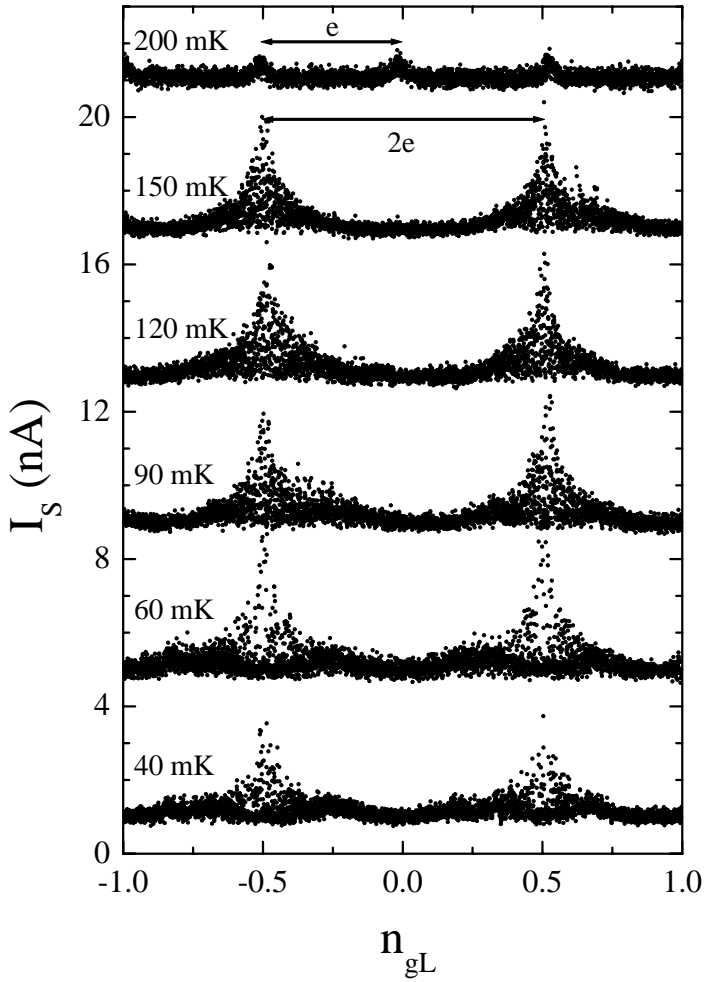


Figure 5.2: The switching current versus n_{gL} for different temperatures. The curves are offset 4 nA for clarity. The odd-even transition temperature was 190 mK, while the main peaks partly collapse below ~ 80 mK.

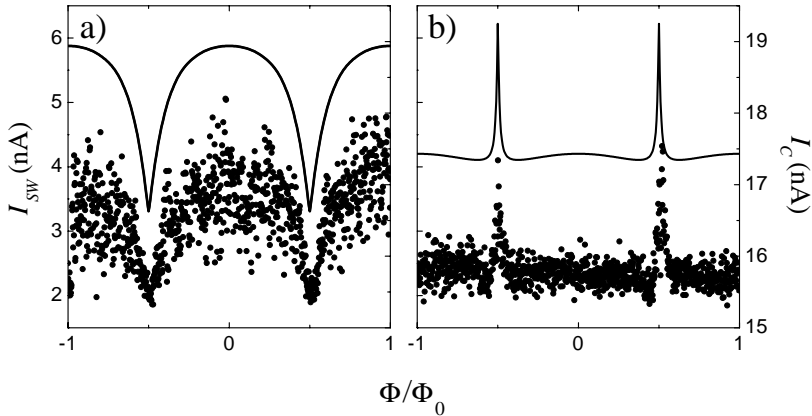


Figure 5.3: The measured switching current (dots) and the calculated critical current (solid lines) are plotted as a function of the magnetic flux for two gate configurations. The scale for the switching current measurements is on the left, the scale for the critical current simulations is on the right. The gates were tuned to (a) $n_{gL} = 1/2$, $n_{gR} = 1/2$ and (b) $n_{gL} = 0.75$, $n_{gR} = 0.44$.

switching current versus n_{gL} for various temperatures, the traces are offset 4 nA for clarity. Below 80 mK the main switching current peak partly collapses, an effect that has been observed in other samples, but that is not understood at this moment [13]. All of the measurements reported here were done at 110 mK, where the traces had the highest critical current at $n_{gL} = 0.5 \text{ mod } 1$.

The measurements of Fig. 5.3 show that the switching current of the Bloch transistor depends on the magnetic flux threading the loop. The black squares represent single switching current events. The modulation of the switching current is periodic in the applied flux with a periodicity of Φ_0 . The behavior depends non-trivially on the combination of gate charges. There are sharp dips in the switching current as a function of flux for induced charges $n_{gL} = 1/2$, $n_{gR} = 1/2$ (Fig. 5.3a) while sharp peaks appear in the switching current behavior for induced charges $n_{gL} = 0.75$, $n_{gR} = 0.44$ (Fig. 5.3b). The dependence of the switching current on the gate voltages and flux through the loop is closely related to the dependence of the critical current attained from simulations, shown as solid lines. The simulations are based on a model that describes the circuit in terms of a single quantum mechanical wave function.

The model used to describe this system was arrived at by quantizing the macroscopic current conservation equations for the circuit shown in Fig. 5.1. In

general, the dynamics of circuit can be described in terms of the four gauge invariant phases γ_i , of the junctions. However there are two restrictions on the four phases. The flux quantization condition relates the phases of junctions in the loop to the externally applied flux Φ , $\gamma_3 + \gamma_4 = 2\pi\Phi/\Phi_0$, where $\Phi_0 = h/2e$ is the superconducting flux quantum. As long as there is no voltage across the Bloch transistor, the phases of the two junctions of the Bloch transistor are related to a time independent external phase θ , $\gamma_1 + \gamma_2 = \theta$. With these two restrictions on the four junction phases, two independent variables can be defined. We take these variables to be $\phi_L = (\gamma_1 - \gamma_2)/2$ and $\phi_R = (\gamma_3 - \gamma_4)/2$. We assume that all the junctions have identical capacitances and critical currents ($C = C_i$, $I_c = I_{ci}$). The Hamiltonian $H = H_{el} + H_J$ that follows from this analysis is the sum of the electrostatic Hamiltonian and the Josephson Hamiltonian. When expressed in the charge basis they are

$$\begin{aligned}
 H_{el} &= \sum_{n_L, n_R} [E_C (n_L - n_{gL})^2 + E_C (n_R - n_{gR})^2 \\
 &\quad + E_m (n_L - n_{gL})(n_R - n_{gR})] |n_L, n_R\rangle \langle n_L, n_R|, \\
 H_J &= -\frac{E_J}{2} \sum_{n_L, n_R} \left[\cos\left(\frac{\theta}{2}\right) (|n_L, n_R\rangle \langle n_L - 1, n_R| + |n_L + 1, n_R\rangle \langle n_L, n_R|) \right. \\
 &\quad \left. + \cos\left(\frac{\pi\Phi}{\Phi_0}\right) (|n_L, n_R\rangle \langle n_L, n_R - 1| + |n_L, n_R + 1\rangle \langle n_L, n_R|) \right],
 \end{aligned} \tag{5.1}$$

where n_L and n_R are the number of excess Cooper pairs on the left and the right island, C_Σ is the sum of all capacitors connected to an island, $E_C = e^2 C_\Sigma / (2(C_\Sigma^2 - C_m^2))$ is the charging energy, $E_m = e^2 C_m / (C_\Sigma^2 - C_m^2)$ is the electrostatic interaction energy and $E_J = \hbar I_c / 2e$ is the Josephson coupling energy. For this circuit $C_\Sigma = 3fF$, $E_C = E_m = 27 \mu\text{eV}$ and $E_J = 70 \mu\text{eV}$. To determine the ground state, a trial wave function was expressed in terms of the 25 charge states $|n_1, n_2\rangle$ with the lowest charging energies. This trial wave function was substituted into the Schrödinger equation and the resulting matrix equation was solved numerically. Once the ground state $|\Psi_0\rangle$ was determined, the expectation value of the Josephson supercurrent flowing through the Bloch transistor was evaluated using the expression,

$$\langle I_S \rangle = \left\langle \Psi_0 \left| \frac{2e}{\hbar} \frac{dH}{d\theta} \right| \Psi_0 \right\rangle. \tag{5.2}$$

The maximum supercurrent, or critical current, is $I_C = \max I_s(\theta)$. Calculations of I_C are shown as solid lines in Fig. 5.3. For other combinations of gate charges, there is also good qualitative agreement between the model and the experiments. The quantitative difference between the theory and the experiment is due to the

dissipative environment that has not been included in this model. Joyez et al. have shown that the low impedance environment of the Bloch transistor reduces the measured switching current below the critical current that is calculated with this simple theory [14]. The differences between the calculated critical current and the measured switching current with the specified junction resistances are similar to values reported by Flees et al. [10].

The flux threading the loop effectively changes the Josephson energy of the Cooper pair box and hence the ratio E_J/E_C . The expectation value of the charge on island R strongly depends on this ratio. Consequently, changing the flux also changes the expectation value of the charge on island R . Part of this charge is induced on island L via the mutual capacitance C_m . Thus one can expect a modulation of the switching current when changing the flux. This does not hold however at a gate charge of $n_{gR} = 1/2$. At this gate charge, the expectation value of the charge on the island is always e , independent of the ratio E_J/E_C [12]. The measurements of Fig. 5.3 were taken at gate charge $n_{g2} = 1/2$, but still show a modulation of the switching current. Consequently the data cannot be explained by simply assuming that the average charge on island R "gates" the Bloch transistor.

The data of Fig. 5.3a can be qualitatively understood with the following argument, assuming a collective ground state for the whole system. When both gates of our system are tuned to half a Cooper pair, the states $|0, 1\rangle$ and $|1, 0\rangle$ have the lowest electrostatic energy. When the Josephson energy is small ($\Phi = \Phi_0/2$) compared to the electrostatic energy, the ground state will be close to $\frac{1}{2}\sqrt{2}(|0, 1\rangle + |1, 0\rangle)$, resulting in relatively small charge fluctuations on both islands. When the Josephson energy is maximum ($\Phi = 0$) compared to the electrostatic energy it will mix in other charge states like $|0, 0\rangle$ and $|1, 1\rangle$, increasing the charge fluctuations on both islands. In general, the charge fluctuations are strongly coupled through capacitor C_m and when sweeping the flux from 0 to 1, the charge fluctuations will be minimal at $\Phi/2$, resulting in a minimal switching current, as confirmed in Fig. 5.3a.

Figure 5.4 shows measurements of the switching current I_{SW} and calculations of I_C as a function of the induced charges on the islands at an enclosed magnetic flux of 0 and $\Phi_0/2$. Because of the gate cross capacitances, it was necessary to tune both gates simultaneously to sweep orthogonally through induced charge space. Figure 5.4a shows that the switching current is $2e$ -periodic in both n_{gL} and n_{gR} , confirming that quasiparticle poisoning is absent on both islands. When $\Phi = 0$, both I_{SW} and I_C are almost independent of n_{gR} . An intuitive explanation is that for $\Phi = 0$ the effective Josephson energy $E_J \cos\left(\frac{\pi\Phi}{\Phi_0}\right) = 70 \mu\text{eV}$ is larger

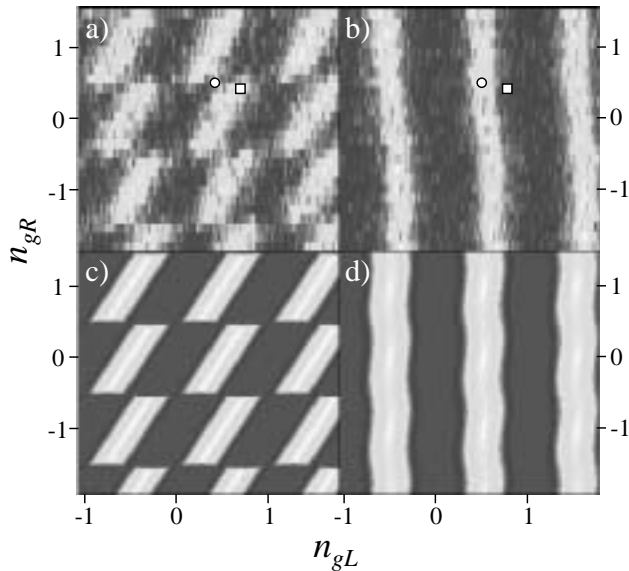


Figure 5.4: The measured switching current (Fig. 5.4a,b) and the calculated maximum supercurrent (Fig. 5.4c,d) are plotted as a function of the charge induced on the two gates for $\Phi = 0$ (Fig. 5.4a,c) and $\Phi = 1/2\Phi_0$ (Fig. 5.4b,d). The symbols denote the gate voltages where the data of Fig. 5.3a (o) and Fig. 5.3b (\square) was extracted.

than the charging energy $E_C=27 \mu eV$ on island R . Cooper pairs are not localized on island R and the circuit behaves as a single Bloch transistor with a capacitance to ground formed by C_m and $2C$ in series. The remaining small wiggles in the simulation indicate that some charging effects should still remain, but they are outside the resolution of our switching current measurements. When $\Phi = \Phi_0/2$, E_J is very small and Cooper pairs are localized on the island R . The saw-tooth like dependence of I_{SW} on n_{gR} indicates the dominance of charging effects on island R . The dots indicate the gate voltages where the data shown in Fig. 5.3a and 5.3b was extracted. These are the points where the flux modulation is most pronounced.

5.4 Conclusions

In conclusion, all switching current measurements have the same gate voltage and flux dependence as a model in which we calculate the maximum supercurrent of the ground state of the combined system. The ground state is a superposition

of spatially distinct charge states, where the coupling capacitor not only couples charge but also strongly correlates the quantum mechanical charge fluctuations on both islands. The good agreement between this model and the experiment implies that it was possible to prepare the circuit in a superposition of charge states. Macroscopic superposition of this sort is necessary to achieve the entanglement used in a controlled-NOT gate in quantum computation. In principle it should also be possible to measure entanglement in such systems of coupled superconducting islands.

5.5 Acknowledgements

We thank Hannes Majer and Raymond Schouten for technical assistance.

References

- [1] T. H. Oosterkamp, T. Fujisawa, W. G. van der Wiel, K. Ishibashi, R. V. Hijman, S. Tarucha, and L. P. Kouwenhoven, *Nature* **395**, 873 (1998).
- [2] B. E. Kane, *Nature* **393**, 133 (1998).
- [3] Yu. Makhlin, G. Schön, and A. Schnirman, *Nature* **398**, 305 (1999).
- [4] Y. Nakamura, Yu. A. Pashkin, J. S. Tsai, *Nature* **398**, 786 (1999).
- [5] J.E. Mooij, T.P. Orlando, L. Levitov, Lin Tian, Caspar H. van der Wal, and Seth Lloyd, *Science* **285**, 1036 (1999).
- [6] Jonathan R. Friedman, Vijay Patel, W. Chen, S. K. Tolpygo, J.E. Lukens, *Nature* **406**, 43 (2000).
- [7] Caspar H. van der Wal, A. C. J. ter Haar, F. K. Wilhelm, R. N. Schouten, C. J. P. M. Harmans, T. P. Orlando, Seth Lloyd, and J. E. Mooij, *Science* **290**, 773 (2000).
- [8] K. A. Matveev, M. Gisselält, L. I. Glazman, M. Jonson, and R. I. Shekhter, *Phys. Rev. Lett.* **70**, 2940 (1993)
- [9] M. T. Tuominen, J. M. Hergenrother, T. S. Tighe, and M. Tinkham, *Phys. Rev. Lett.* **69**, 1997 (1992).
- [10] Daniel J. Flees, Siyuan Han, and J. E. Lukens, *Phys. Rev. Lett.* **78**, 4817 (1997).
- [11] M. Matters, W. J. Elion, and J. E. Mooij, *Phys. Rev. Lett.* **75**, 721 (1995).

-
- [12] V. Bouchiat, D. Vion, P. Joyez, D. Esteve, and M. H. Devoret, *Phys. Scr.* **T76**, 165 (1998); *Journ. Supercond.* **12**, 789 (1999).
- [13] See for example, C. H. van der Wal, Ph.-D thesis, Delft University of Technology, 2001.
- [14] P. Joyez, P. Lafarge, A. Filipe, D. Esteve, and M. H. Devoret, *Phys. Rev. Lett.* **72**, 2458 (1994).

Chapter 6

Design and fabrication of an on-chip microwave generator and detector

C. P. Heij, E. V. Eijkelenboom,
P. Hadley and J.E. Mooij

6.1 Introduction

Studying dynamics of mesoscopic systems requires an accurate control of the system parameters in time. The characteristic energy scales in mesoscopic systems are of the order of $1 - 200 \mu\text{eV}$ or $0.5 - 100 \text{ GHz}$. This means that the systems have to be extremely well decoupled from these modes in the environment, but at the same time they have to be manipulated at these sub-nanosecond timescales. Usually the control electronics is located at room temperature and is connected to the systems via cabling that has to be carefully filtered and anchored to the various temperature stages in the cryostat. As the complexity of the circuits is increased, more cables have to be mounted, increasing the amount of noise coupled in and the heat load of the cryostat.

A way to circumvent this problem is to fabricate part of the control electronics on-chip. In these last two chapters we study the performance of a microwave frequency generator that is fabricated on-chip. We show that a damped Josephson junction is a suitable radiation source. We demonstrate the ability to turn the generator on and off on a sub nanosecond timescale. This control is still provided by pulses made outside the cryostat, but in the future techniques like Rapid Single Flux Quantum (RSFQ) electronics [1] could be used to make the pulses on-chip.

We choose to manipulate an artificial two level quantum system in the form of a Cooper Pair Box (CPB), where quantum coherent dynamics like Rabi oscillations can be studied. Because of experimental difficulties that will be explained in the next chapter, so far the CPB was only used as a detector to quantify the performance of the generator and the coupling circuitry. With further improvements of the design the study of quantum phenomena in mesoscopic circuits like a CPB should be possible.

In this chapter, we will first discuss the basics of a Josephson junction as a microwave generator and the CPB as a microwave detector. Then we will consider the general design constraints, sample fabrication and the measurement setup. In chapter 7 the performance of the on-chip microwave generator will be discussed with measurements on two different samples.

6.2 The Josephson generator

As described in paragraph 1.4, the dynamics of a single shunted Josephson junction is described by the second order differential Eq. 1.7, an equation similar to that of a damped pendulum. The McCumber parameter β_C quantifies the amount of damping. If β_C is smaller than 1, the dynamics of the Josephson junction resemble that of an overdamped pendulum. For this case, the time evolution of the quantum mechanical phase difference ϕ can be solved analytically. Using the second Josephson relation 1.10, the voltage over the junction can be written as

$$V(t) = V + \tilde{V}(t) = \bar{V}\sqrt{i^2 - 1} + \bar{V} \sum_{n=1}^{\infty} \alpha_n \cos 2\pi n f t, \quad (6.1)$$

$$\alpha_n = 2\sqrt{i^2 - 1} \left(\sqrt{i^2 - 1} - i \right)^n, \quad (6.2)$$

where $\bar{V} = I_C R_T$, i is the bias current normalized to the critical current, $i = I_{SQ}/I_C$ and R_T is the total resistance of the damped junction. The voltage signal consists of a DC part and a fundamental frequency f with its harmonics. The frequency f is the Josephson frequency $2eV/h$. Figure 6.1 shows the amplitude of the fundamental frequency and the first three harmonics as a function i . The harmonics disappear for higher values of i where α_1 approaches unity. Experimentally feasible frequencies f lie between 1 and 200 GHz, the lower limit set by noise, the upper limit by heating of the junction above T_C . The line width is limited by thermal noise of the shunt resistor and is usually in the range of 10-100 MHz [2]. The maximum amplitude of the signal at the fundamental frequency, $I_C R_T$, is the $I_C R_J$ product [3], 310 μV for unshunted aluminum tunnel

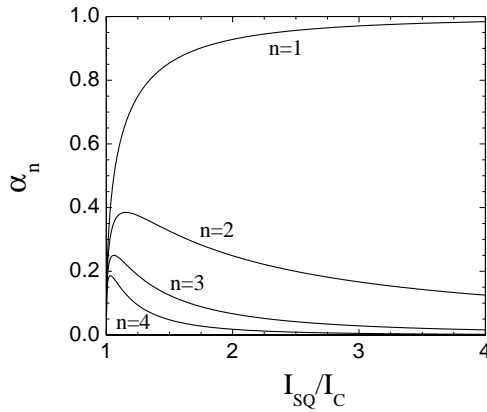


Figure 6.1: Amplitude of the harmonics of an overdamped Josephson junction as given by Eq. 6.2.

junctions. Unshunted junctions usually have a McCumber parameter much bigger than one, and for experimentally accessible oxide thicknesses, we need a shunt resistance of the same order or smaller than the junction resistance to get $\beta_C < 1$. This yields a maximum amplitude of $\sim 150 \mu\text{V}$ for overdamped aluminum tunnel junctions. Larger amplitudes could be obtained by using superconducting tunnel junctions made of material with a larger $I_C R_J$ product, like niobium.

Because the shunted junctions are overdamped, the IV-characteristics are non-hysteretic, and setting the bias current will unambiguously determine the DC-voltage and hence the frequency f . To change the amplitude of the signal, we need control over the critical current of the junction. This is possible in a Superconducting QUantum Interference Device (SQUID) [4]. The single junction is replaced by two Josephson junctions in parallel, and the critical current of this system can be controlled by the magnetic flux Φ_{SQ} threading the loop. If the loop is small, the effect of self inductance can be ignored and the critical current of the SQUID is

$$I_C = \sqrt{I_{C1}^2 + I_{C2}^2 + 2I_{C1}I_{C2} \cos \frac{2\pi\Phi_{SQ}}{\Phi_0}}, \quad (6.3)$$

where I_{C1} and I_{C2} are the critical currents of the individual junctions [5, 6]. The effective critical current I_C varies between $|I_{C1} - I_{C2}|$ and $I_{C1} + I_{C2}$, the junctions should be made as symmetrical as possible to maximize the attainable amplitude swing. Figure 6.2 shows a close-up of the completed Josephson generator coupled to the detector. The two SQUID junctions are visible on the left.

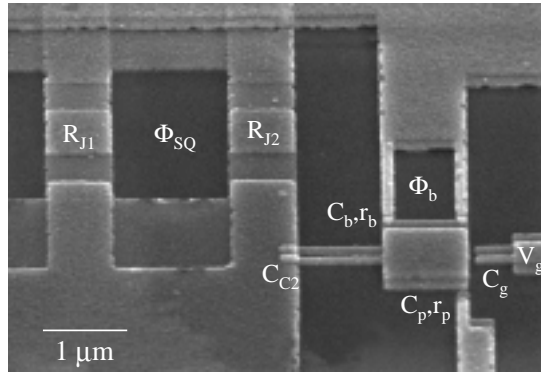


Figure 6.2: Scanning electron microscope photograph of the SQUID and the CPB. They are coupled via overlap capacitors C_{C1} , partly visible at the top, and C_{C2} .

Because the SQUID generator is current biased in the resistive regime, heat will be generated by the SQUID. Most of the heat is generated in the resistive shunt, as its impedance is usually lower than the junctions resistances in the overdamped regime. To minimize the effects of heating, the shunt is placed $20 \mu\text{m}$ to the left of the junctions and is not visible in Fig. 6.2. Apart from placing the shunt further away, a cooling fin was also attached, to cool the electrons passing through it. The electron temperature in the shunt depends on the volume V of the cooling fin as $V^{-\frac{1}{5}}$ [7]. Consequently the shunt should be made as large as possible, within the general design constraints as formulated in paragraph 6.4.

6.3 The Cooper pair box as microwave detector

Although the ultimate goal is to study quantum dynamics in an artificial two-level system like the CPB, we will first use the CPB as a microwave detector to test the performance of the Josephson generator and the coupling circuit. The CPB consists of a central island coupled to leads by a Josephson junction. The electrostatic energy of the island can be controlled by a gate. To obtain a two-level system where 0 and 1 excess Cooper pair are the only occupied charge states, the Josephson energy E_J should be sufficiently smaller than the charging energy which is typically $100 \mu\text{eV}$. We aim at a resistance of $10 - 20 \text{ k}\Omega$, resulting in a Josephson energy of $30 - 60 \mu\text{eV}$. In order to be able to control the Josephson energy, the box junction is replaced by two parallel junctions. The magnetic flux Φ_b threading the loop determines the effective Josephson energy, just like the flux Φ_{SQ} determines the critical current of the SQUID. In order to be able to

control E_J and I_C separately, the size of the loops are made different. Figure 6.2 shows the two loops. Although the fabricated size only differs by a factor of 4, the actual flux periodicities differ by a factor of 10. Presumably this is caused by the large superconducting SQUID leads, that focus the flux differently on the SQUID and the CPB.

To detect the quantum state of the system, a small probe junction (C_p, r_p) is also attached to the island. The resistance of this probe junction should be high enough not to disturb the coherent evolution of the quantum state of the system. In this so-called coherent regime, $\hbar\Gamma_{qp} \ll E_J(\Phi_b)$, where Γ_{qp} is the quasiparticle escape rate through the probe junction. For the experimental parameters mentioned above this means that the probe junction should have a resistance of at least several $M\Omega$.

The radiation of the Josephson generator is coupled to the CPB junction by capacitors C_{C1} and C_{C2} . To couple through the maximum amount of radiation to the CPB junction, both capacitors have to be as large as possible. Because C_{C2} is connected directly to the island, the charging energy of the island depends on its capacitance. Because $k_B T$ has to be substantially smaller than the charging energy E_C , 1 fF is about the upper limit for C_{C2} .

To detect the radiation we use a resonant process, the Josephson Quasi Particle (JQP) cycle. As explained in paragraph 1.6, this involves the destruction of coherent tunnelling of a Cooper pair through one junction (the box junction), by a quasiparticle tunnelling through the other junction (the probe junction). The tunnelling of a second quasiparticle resets the system to its original state. If the Cooper pair tunnelling is aided by the absorption or the emission of a photon with energy $hf > E_J$, this will show up as side peaks of the main JQP peak. The height of the peaks is determined by the amplitude of the radiation field. The position and the height of these peaks, combined with bias of the SQUID, will be used to calculate the efficiency of the generator and the coupling circuit.

6.4 General design considerations

The performance of an on-chip frequency generator not only depends on the quality of the signal that the generator can produce, but also on the surrounding circuitry that controls the generator and focusses the radiation on the object of interest. Not only should the maximum amount of signal be coupled through, but resonances should also be avoided in these circuits. Figure 6.3 shows a schematic of the Josephson generator, the CPB as detector and the surrounding circuitry. First we will discuss the role of the lead resistors R_L , second we will look at the

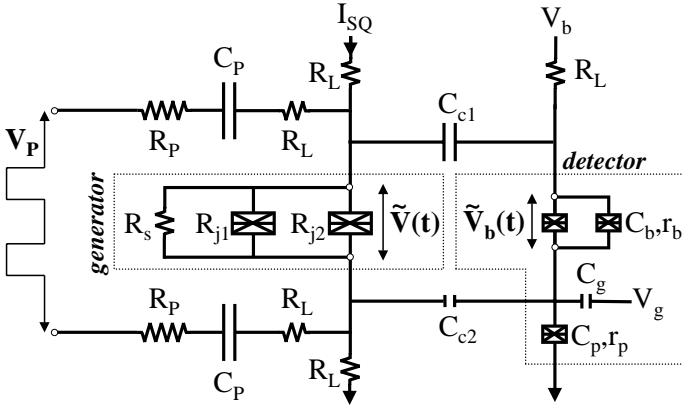


Figure 6.3: Schematic of the circuit elements that are fabricated on-chip. The SQUID and the CPB are coupled via two coupling capacitors and a pulse signal V_P can be coupled from the launchers to the SQUID capacitively.

requirements of the circuitry that couples the SQUID and the CPB and finally we will discuss the coupling of pulses to the SQUID.

The generator produces a time dependent signal $\tilde{V}(t)$ that has to be coupled to the detector as efficiently as possible. Bias leads are attached to the generator to control the frequency content of the signal and to switch the generator on and off. The impedance of these leads will be frequency dependent as they run to the top of the cryostat and are approximately 2 meters long. To prevent the environmental impedance from shunting the generator, the leads are shielded from the generator by an on-chip resistors R_L close to the generator. On one hand R_L should be considerably larger than the total resistance of the generator, but on the other hand they should not be too large because of the dissipation ($I^2 R_L$) in the resistor. Because of the heat dissipation, the lead resistors in the DC-bias leads are placed at a distance of $150 \mu\text{m}$ from the generator. This is the maximum distance where build-up of standing waves in the leads is still avoided. As a rule of thumb, all our circuit components have to be smaller than, or located within $\frac{1}{10}$ th of the smallest wavelength generated to be able to treat them as lumped elements [8]. This corresponds to $\frac{1}{10} \frac{c}{\sqrt{\epsilon_r} f} \sim 150 \mu\text{m}$ for 100 GHz, when a dielectric constant of 5 is used for SiO, the top layer of the substrate.

To detect the radiation the SQUID generates, the SQUID is coupled to a detector in the form of a Cooper pair box. As can be seen in Fig. 6.3, the leads of the SQUID are capacitively coupled to the lead electrode of the Cooper pair box by capacitor C_{C1} and to the island of the Cooper pair box via a gate capacitance

C_{C2} . We used purely capacitive coupling to electrically isolate the two circuits for DC signals, avoiding grounding problems. Capacitor C_{C1} should be made big enough so that its impedance is small compared to the other impedances in the circuit at the lowest frequencies that are used. For typical sample parameters this requires a capacitance of ≥ 10 pF. If we assume that C_p and C_g are small with respect to C_b and C_{C2} , the fraction of $\tilde{V}(t)$ that now arrives at the box junction C_b is

$$\tilde{V}_b(t) = \frac{C_b}{C_b + C_{AC}} \tilde{V}(t), \quad (6.4)$$

Because of the small capacitance of the detector (~ 1 fF) the LC resonance of the coupling circuit will be at frequencies far outside the range of use of the generator. If the typical size of the coupling circuit is a few micrometers (~ 1 pH/ μm) the LC resonance occurs at THz frequencies.

6.5 A generator with nanosecond control

To be able to switch the generator on and off at nanosecond timescales, a special substrate holder was designed. A photograph of the sample holder is shown on the left of Fig. 6.4. The sample was clamped to the copper holder and wire-bonded to the gold pads which are connected to the measurement wires. A custom made rf-probe (PicoprobeTM [9]) was mounted on the sample holder such that its gold forked probe touched the rf-launchers that are fabricated on-chip. All rf-cabling, from the top of cryostat to the rf-probe, is made of standard 50 Ω HP 2.4 mm technology and is specified to 50 GHz [10]. The on-chip launchers were co-planar wave guides which were also designed to have 50 Ω characteristics. With this setup, 50 Ω characteristics were defined from the top of the cryostat until 300 μm from the actual generator. Reflections were minimized and the distortion of the resulting pulse shape at the generator was as small as technically possible. Figure 6.5 shows the form of a typical pulse at the pulse generator output and at the end of 2 meters of coaxial cable. Because of dispersion inherent to the long cabling, the rise time has increased from 100 ps to 300 ps. Although a fast rise time is not crucial for Rabi-type experiments, it should not become too large.

Figure 6.3 shows the circuitry connected to the on-chip rf-launchers. Essentially the structure is a voltage divider which also decouples the signal capacitively. The signal was decoupled for DC signals because the coax cable uses a different (cold) ground than the SQUID's current source (grounded in the room temperature electronics). To assure that the voltage signal over the SQUID was stable in time, the RC time of the pulse circuitry had to be much larger than

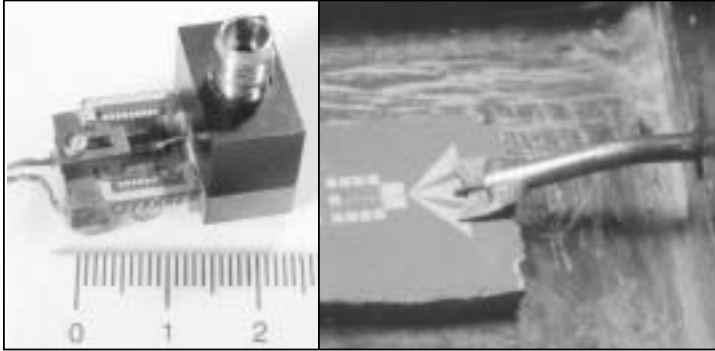


Figure 6.4: On the left a picture of the sample holder with the rf-probe attached. Usually the small sample is wire bonded to the pads, but the bonding wires have been removed for clarity. Wires connecting the sample to the filtering are soldered to the back of the pads. The scale is in centimeters. On the right a zoom of the rf-probe touching the on-chip $50\ \Omega$ launchers. On the sample the 9 square bonding pads ($200 \times 200\ \mu\text{m}^2$) and the two coupling capacitors (in between the launchers and the bonding pads) are clearly visible.

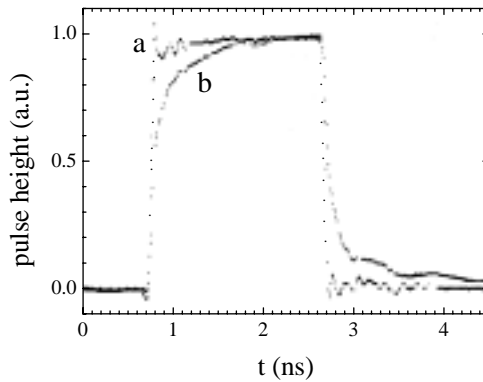


Figure 6.5: (a) Pulse signal measured directly at the output of the pulse generator and (b) same pulse measured at the end of the coaxial cable, at the point where the Pico-probe was connected.

the maximum pulse length of 10 ns. Because $R_P + R_L \gg R_T$, where R_T is the total resistance of the SQUID, the constraint is $2\pi(R_P + R_L)C_P \leq 10^{-8}$ ns. For a typical SQUID resistance of 10Ω this means that C_P had to be at least 0.1 nF. If this condition is satisfied, we can calculate the voltage signal over the SQUID when a pulse with height V_P at the launchers is applied. With help of Eq. 6.1 the height of the pulse at the SQUID $V_{P,SQ}$ is,

$$V_{P,SQ} = I_C R_T \sqrt{\frac{(I_{P,SQ} + I_{SQ})^2}{I_C^2} - 1} \quad (6.5)$$

where $I_{P,SQ} = \frac{V_P}{(2R_L + 2R_P)}$. This equation is only valid when the pulse is short with respect to the repetition time. Because the signal is coupled in capacitively, the average signal over the capacitors is zero and the general equation is more complicated, and depends on the pulse length and the repetition time.

6.6 Sample fabrication

The circuit was fabricated on a thermally oxidized silicon substrate in three layers using standard electron beam lithography. For each layer, the evaporation mask was defined in a double layer resist with a high resolution electron beam pattern generator at 100 kV. In the first layer a 3 nm Ti sticking layer was followed by 25 nm of Pt, both evaporated perpendicular to the substrate. In this layer markers were defined to align subsequent layers, as well as a resistive shunt with a $30 \times 250 \mu\text{m}^2$ planar cooling fin attached and lead resistors in both the SQUID and CPB leads. Before spinning the next layer of resist, the sample was dipped in fuming nitric acid to clean the Pt surface and assure a small contact resistance between the Pt layer and the subsequent Al layer.

For fabrication of the large SQUID junctions, we used a thick double layer resist (800 nm+200 nm) to get a large undercut. The SQUID was fabricated in aluminum using shadow fabrication under angles of $+30^\circ$ (30 nm) and -30° (50 nm) with the substrate normal. In between the two evaporations, the aluminum was oxidized for 5 minutes in 25 mTorr of O_2 . To form the dielectric for the overlap capacitors, after lift-off of the second Al layer, the sample was heated to 150°C and the top layer of aluminum was oxidized in an O_2 plasma at 150 mTorr for 90 seconds. The resulting Al_xO_y layer was 4 nm thick [11].

In the final layer, the overlap capacitors were completed and the CPB was formed by two angle shadow evaporation under angles of $+11^\circ$ and -11° . In between the evaporation steps the Al was oxidized at 50 mTorr for 5 minutes. The probe junction should have a high resistance and a very small capacitance, so

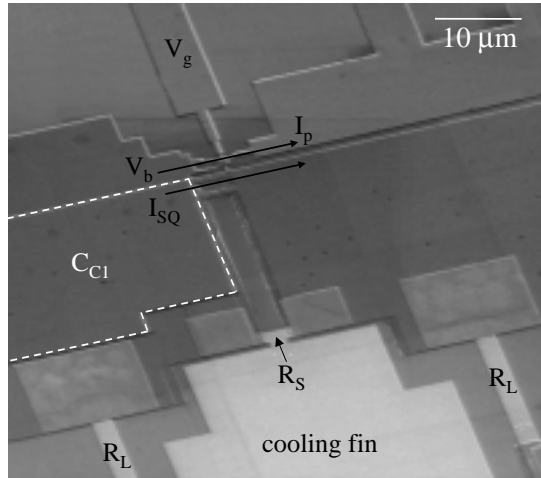


Figure 6.6: Overview of the completed three-layer sample. The contours of the coupling capacitor C_{C1} are shown with the white dashed line. At the sides of the cooling fin the lead resistors of the pulse circuitry are visible, as well as a small part of the pulse capacitor C_P at the bottom right hand.

the bottom lead barely touches the island. The island was capacitively connected to the SQUID's bottom lead by the small overlap capacitor C_{C1} . This capacitance should be of the same order as C_b , in order to transfer a substantial part of the Josephson radiation to the CPB junction. Just visible at the top of Fig. 6.2 is the overlap between the CPB's top lead and the SQUID's top lead, forming the capacitor C_{C1} .

An overview of the completed sample is shown in Fig. 6.6. At the bottom, part of the cooling fin is visible. Next to the cooling fin lie the resistors R_{P2} , necessary to block the Josephson radiation from disappearing into the pulse capacitors C_P (partly visible at the bottom right hand). The area denoted by the white dashed line is the overlap capacitor C_{C1} .

6.7 Measurement set-up

The sample holder with the Pico-probe was mounted in a microwave tight copper box connected to the mixing chamber of a dilution refrigerator with a base temperature of 8 mK. All of the measurement leads were filtered using π -filters at room temperature and copper-powder low-pass filters at the mixing chamber. We used dedicated room temperature low-noise electronics to measure the cur-

rents through and voltages over the generator and the detector. The SQUID was current biased, and a four probe measurement determined the DC-voltage V over the SQUID. The CPB was biased by a voltage V_b and the current I_P was measured with an I-V converter. The rf-probe was connected to a semirigid coaxial cable running from the sample can to room temperature. The coaxial cable was thermally anchored and attenuated at room temperature (-20 dB), the dilution refrigerators 1 K pot (-20 dB) and the mixing chamber (-3 dB). A HP 8133A pulse generator was used to switch the SQUID on and off. This pulse generator can produce pulses of 0.1-10 ns with a rise time of 50 ps, a repetition rate of 0.01-3 GHz and a maximum amplitude of 3 V.

In this chapter we discussed the desired specifications of the generator and the detector. A general constraint is that all the on-chip circuitry should be made smaller than $\sim 150 \mu\text{m}$ to avoid the build-up of standing waves. Guiding the pulses from outside the cryostat to the generator, requires cabling and a rf-probe that are impedance matched to 50Ω and the use of 50Ω on-chip rf-launchers. In the next chapter we will discuss the measurements performed on two different samples.

References

- [1] For a review see P. Bunyk, K. Likharev, and D. Zinoviev, *RSFQ Technology: Devices and Circuits*, Int. J. on High Speed Circuits and Systems **11**, No.1, 257 (2001).
- [2] K. K. Likharev, *Dynamics of Josephson junctions and circuits* p. 107 (Gordon and Breach, Philadelphia, 1986), second edition.
- [3] Often called the $I_C R_n$ product, V. Ambegaokar and A. Baratoff, Phys. Rev. Lett. **10**, 486 (1963); erratum, **11**, 104 (1963).
- [4] J. Clarke, *Superconducting electronics*, edited by H. Weinstock and M. Nisenson, NATO ASI series, Vol. F-59, 1989.
- [5] T. P. Orlando en K. A. Delin, *Foundations of Applied Superconductivity* p. 419 (Addison-Wesley, Reading, 1991), first edition.
- [6] M. Tinkham, *Introduction to Superconductivity* pp. 224-226 (McGraw-Hill, New York, 1996), second edition.
- [7] See for example, W. Hoogeveen, Graduation report, Delft University of Technology, 1996.

- [8] P. A. Rizzi, *Microwave engineering, passive circuits* (Prentice-Hall, London, 1988).
- [9] Partnumber P-10-5770 sold by GGB Industries, Inc., Florida, USA.
- [10] See www.agilent.com.
- [11] See Fig. 1.10 for the Al_xO_y thickness for other oxidation parameters.

Chapter 7

An on-chip Josephson generator with nanosecond control

C. P. Heij, E. V. Eijkelenboom,
P. Hadley and J.E. Mooij

We discuss the performance of a shunted Josephson junction as a local on-chip microwave generator. The microwaves are coupled into the detector circuit by overlap capacitors formed in the multilevel fabrication process. The signal was detected using Photon Assisted Tunnelling (PAT) of the Josephson QuasiParticle (JQP) cycle in a Cooper Pair Box (CPB) with an attached probe junction. By carefully designing the coupling circuitry as described in the last chapter, we succeeded in transmitting 75% of the generated signal, unlike the 10% achieved in earlier experiments [1]. Using an external pulse generator, we were able to control the SQUID on a sub-nanosecond timescale. Because of a faulty DC-blocking capacitor it was not possible however to conduct coherence measurements on the CPB. An improved design should circumvent these problems in the future.

The experiments described in this chapter were performed on two different samples, named sample 1 and sample 2. The measurements in paragraph 7.2 were performed with sample 1, while the measurements in paragraph 7.3 were performed with sample 2. All measurements were done in a dilution refrigerator with a base temperature of 10 mK. First we discuss the SQUIDS' parameters, than we focus on the CPB and finally we present the results of pulse experiments on the SQUID.

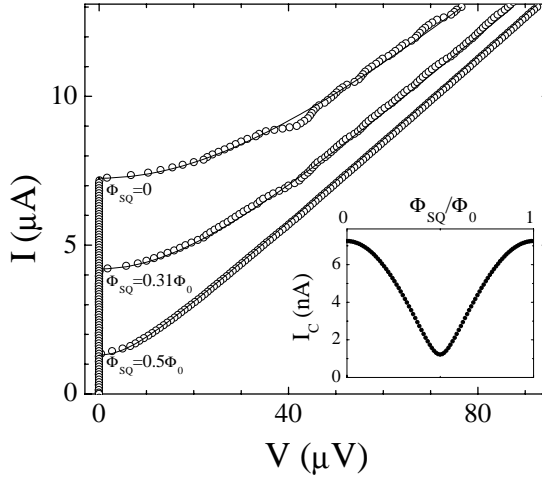


Figure 7.1: The current-voltage characteristics of SQUID 2 for three values of the magnetic flux. The solid lines are theoretical fits according to Eq. 6.3. The inset shows the magnetic flux dependence of the critical current.

7.1 The SQUID as a microwave generator

The SQUIDs' parameters can be fully determined by analyzing its current-voltage (IV) characteristics. The circles in Fig. 7.1 represent the IV characteristics of SQUID 2 for three different values of the magnetic flux threading the SQUID loop. The solid lines are theoretical fits using Eq. 6.1 with the following parameters, $R_{J1} = 73 \Omega$, $R_{J2} = 102 \Omega$, $R_S = 8.4 \Omega$ and $R_T = 7.1 \Omega$. Using $1 \text{ fF}/\mu\text{m}^2$, the total capacitance of the SQUID junctions is 100 fF , yielding $\beta_C = 0.11$. The best fit is obtained for minimal I_C . The middle curve, taken at $\Phi = 0.31\Phi_0$, shows some tiny steps, most noticeably around $V = 40 \mu\text{V} = 19.3 \text{ GHz}$. As I_C increases further the steps become more pronounced. Because the step height scales with I_C , we speculate that they are self-induced Shapiro steps, due to an internal resonance of the SQUID [2]. Despite the small steps, the IV-curves are non-hysteretic and can be current biased to obtain an arbitrary voltage V_{SQ} , one of the important requirements of an on-chip frequency generator.

The inset shows the dependence of the critical current on the magnetic flux. The dependence follows Eq. 6.3, confirming that the self inductance of the SQUID is sufficiently small. The magnetic flux periodicity of the critical current was a factor of 9 smaller than was theoretically calculated from the lithographically designed area and the magnetic field. We think the flux was heavily focussed onto

the SQUID by the large capacitor plates in the leads directly next to SQUID. The lead resistors R_L were 32Ω a piece at base temperature, making the effect of shunting by the leads maximally 10% of the total SQUID resistance. The resistance of the pulse resistors R_P was 128Ω , yielding an on-chip attenuation of the pulse height of $47\times$ for frequencies higher than $(2\pi(R_P + R_L)C_P)^{-1}$. Fabrication parameters of SQUID 1 and SQUID 2 were similar and the IV-characteristics of SQUID 1 also show similar behavior as described above. The sample parameters of SQUID 1 were $R_{J_1} = 83 \Omega$, $R_{J_2} = 113 \Omega$, $R_S = 9.9 \Omega$, $R_T = 8.2 \Omega$ and $\beta_C = 0.13$.

7.2 The Cooper pair box as microwave detector

Before looking at Photon Assisted Tunnelling (PAT) experiments with the CPB in sample 1, we first determined the parameters of the CPB, the probe junction and the coupling capacitors. The high bias resistance of the CPB and the attached probe junction was $985 \text{ k}\Omega$. With help of the stability diagram (see Fig. 7.3) the following parameters could be calculated $\Delta = 200 \mu\text{eV}$, $E_C = 32 \mu\text{eV}$, $C_g = 80 \text{ aF}$, $C_p = 0.1 \text{ fF}$ and $C_b = 1.2 \text{ fF}$, where C_b is the total capacitance of the CPB junctions. By varying the lead potential of the SQUID, a value of $C_{C_2} = 1.1 \text{ fF}$ could be deduced from the Coulomb oscillations induced in the detector. By comparing the capacitor plate sizes we estimated C_{C_1} at 16 pF , satisfying the design criterion $C_{C_1} > 10 \text{ pF}$.

The JQP cycle is stable in the bias voltage range $432 \mu\text{V} < V_b < 496 \mu\text{V}$. In Fig. 7.2a, the solid circles represent a gate trace at $V_b = 460 \mu\text{V}$. Each point is averaged over 0.5 s to filter out the interference present during the measurements. In general, the quality of the IV characteristics of the CPB was poor and heavy filtering was needed to obtain a reasonable signal. Because of the high resistance of the probe junction, Cooper pair tunnelling through this junction can be neglected and only one JQP peak is observed per Coulomb period $e/C_g = 2 \text{ mV}$. According to Eq. 1.19, the peak height is dependent on the Josephson energy, in this case the effective Josephson energy of the CPB. To determine the Josephson energy, the magnetic field was swept and the peak height I_{pmax} was recorded. The magnetic flux periodicity of the critical current was now a factor of 4 smaller than is theoretically calculated from the lithographically designed area and the magnetic field. The flux was also focussed by the large capacitor plates, but it is located more remotely from the leads than the SQUID itself.

Figure 7.2b shows the JQP peak height as a function of the flux threading the loop of the CPB. The solid line is a fit of Eq. 1.19 for $\delta = 0$, since the detuning δ

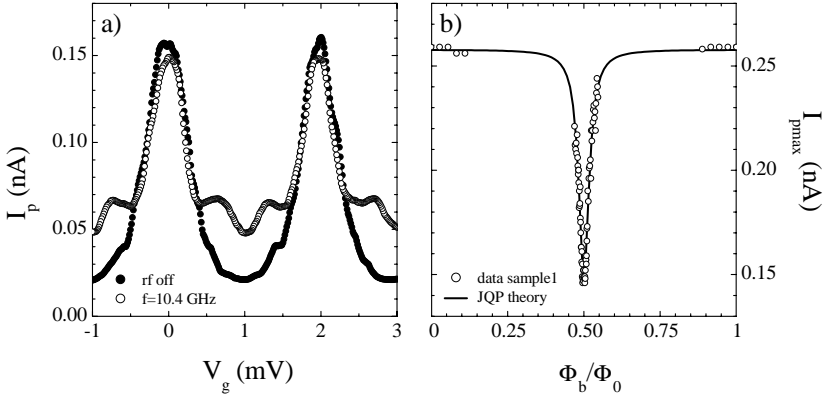


Figure 7.2: (a) The JQP cycle peak at $V_b = 460 \mu\text{V}$ without radiation and with the SQUID biased at 10.4 GHz. (b) The JQP peak current versus the magnetic flux. The solid line provides the best fit using Eq. 1.19.

of the CPB from the Cooper pair resonance is zero at the top of the JQP peak. As fitting parameters we used $R_{b1} = 60 \text{ k}\Omega$ and $R_{b2} = 54 \text{ k}\Omega$. At $\Phi_b = \Phi_0/2$ the effective Josephson energy is minimal, $E_J = 1.1 \mu\text{eV}$. At this value of E_J , $\hbar\Gamma_{p1} > E_J$ and the CPB is in the incoherent regime. The level broadening due to quasiparticle decay is larger than the gap between the ground state and the 1st excited state. One should now observe a linear dependence between the distance of the PAT JQP peak to the main peak and the applied frequency, simplifying the analysis of the SQUID's performance. The data of Fig. 7.2a and the rest of the data shown in this chapter have been taken at $\Phi_b = \Phi_0/2$. To observe the quantum coherent dynamics in the CPB, experiments have to be performed in the coherent regime $\hbar\Gamma_{p1} \ll E_J$, where the decoherence rate due to quasiparticle tunnelling is much smaller than the coherent oscillations of the charge on the CPB.

Using Eq. 1.19 the expected width of the JQP peaks can be calculated. Using the sample parameters determined above, it can be calculated that the peaks are a factor 4 too wide in comparison to the data of Fig. 7.2. Part of this broadening is caused by the interference picked up by the wiring (especially the wires connected to the gate), smearing out the signal. Apart from this, JQP peak broadening has also been observed by others and is not well understood [3]. The SQUID was then tuned to maximum I_C and current biased to obtain a Josephson frequency of 10.4 GHz. The solid circles in Fig. 7.2a represent a gate trace at this SQUID bias. The PAT JQP side peaks can be clearly observed both at the absorption and

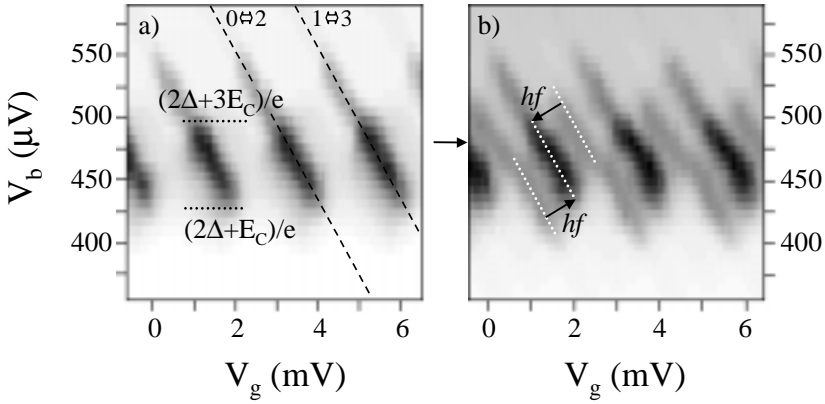


Figure 7.3: Stability diagram of CPB with the attached probe junction (a) without SQUID radiation and (b) with the SQUID biased at 12.2 GHz. Black indicates a maximum current of 0.15 nA, white indicates zero current. The dashed lines in (a) indicate the position of the Cooper pair resonances. The white dotted lines in (b) indicate the expected position of the JQP peak and the PAT side peaks.

the emission side. Measurements at other frequencies confirm that the distance between the PAT peaks and the main peak scales linearly with frequency. Using the previously determined sample parameters it can be shown that the location of the PAT peaks corresponds to the absorption or emission of a single photon by a Cooper pair.

The stability diagram of the highly asymmetric SSET formed by the CPB and the probe junction is shown in Fig. 7.3a. The JQP peaks are visible along the black dashed lines, where the Cooper pair can resonantly tunnel into the CPB. Although a third quasiparticle transition should suppress the JQP peak above $2\Delta/e + 3E_C/e = 496 \mu\text{eV}$, we still observe a faint peak here. This is probably due to the sub-gap quasiparticle currents in the CPB junctions, resetting the third quasiparticle transition and bringing the system into the Cooper pair resonance again. Figure 7.3b shows the stability diagram when the SQUID generates a frequency of 12.2 GHz. The PAT side peaks are clearly visible along both sides of the JQP resonance.

To follow the PAT JQP peaks as a function of the generator frequency, gate traces of the JQP peak were taken for increasing current bias of the SQUID. Figure 7.4 shows that how the peaks move outward as the frequency increases. For frequencies higher than 20 GHz, the PAT JQP peak disappears into the neighboring JQP peak, obscuring the observation of the PAT JQP peak. As also

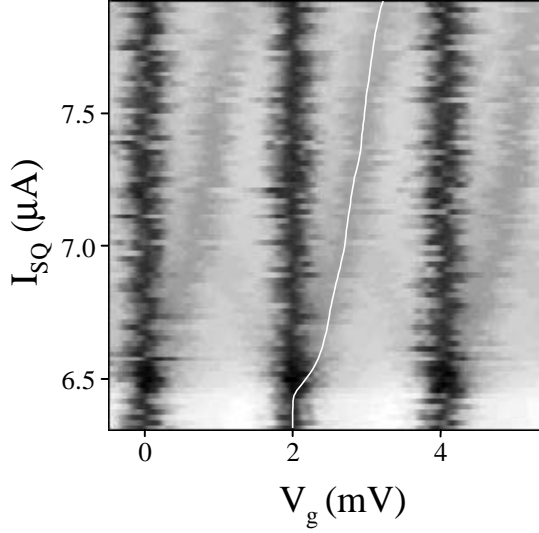


Figure 7.4: JQP current at $V_b = 480 \mu\text{V}$ versus V_g and the current bias I_{SQ} of the SQUID. As the SQUID voltage is proportional to the splitting of PAT and main JQP peak, the IV of the SQUID can be scaled on top.

indicated by the arrow in Fig. 7.3b, the bias voltage is $480 \mu\text{V}$ and consequently one only observes the emission peak. The IV of the SQUID is projected on Fig. 7.4 with a scaling that is calculated with the sample parameters. The PAT peak exactly follows the SQUID characteristics. Also, the peak height shows no major changes as a function of the frequency. It can be concluded that the SQUID generates the expected frequencies and that there are no major resonances in the coupling circuit.

To quantify the efficiency of the coupling circuitry, we studied the JQP and PAT JQP peak height as a function of amplitude of the applied radiation. Equation 1.19 can be easily modified to include the effects of radiation. For the main peak current, the E_J term is replaced by $E_J J_0\left(\frac{2e\tilde{V}_b}{hf}\right)$, where J_0 is the zeroth order Bessel function. For the 1st photon assisted tunnelling peaks, the PAT current is:

$$I_P = \frac{2e\Gamma_{p1}}{\frac{4(\delta \pm hf)^2 + \hbar^2 \Gamma_{p1}^2}{E_J^2 J_1^2\left(\frac{2e\tilde{V}_b}{hf}\right)} + 2 + \frac{\Gamma_{p1}}{\Gamma_{p2}}} \quad (7.1)$$

where J_1 is the first order Bessel function, and where the sign denotes the ab-

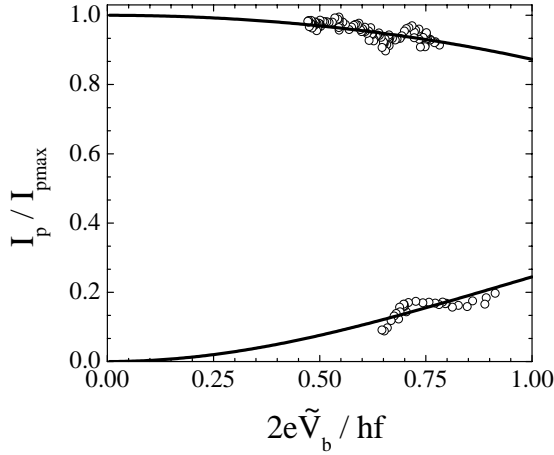


Figure 7.5: The peak height of the main JQP peak and the PAT JQP peak, normalized to the maximum main peak height. The solid lines denote the theoretical fits according to Eq. 7.1 with an rf transmission efficiency of 75%.

sorption (+) or the emission (-) peak. The main JQP peak height and the PAT peak height were now compared with these theoretical expressions. In order to measure the PAT JQP peak current, first the curves without PAT had to be subtracted. The circles in Figure 7.5 shows the normalized peak height of the main JQP peak and the PAT JQP peak versus the argument of the Bessel function. The argument $\frac{2e\tilde{V}_b}{hf}$ is calculated with Eqs 6.1, 6.2 and 6.4. The solid lines represent a theoretical fit using an transmission efficiency of 75%, much higher than the usual efficiencies of $\sim 10\%$ obtained in earlier experiments [1]. Because of the interference problems mentioned earlier, it was very difficult to measure the exact peak heights and further experiments are needed to measure the efficiency more carefully and over a larger parameter range.

7.3 Nanosecond control of the SQUID

First we characterized the rf-cabling mounted from the top of the cryostat to the SQUID. To determine the voltage that arrives at SQUID, we make use of Shapiro steps. When a Josephson junction is irradiated, the Josephson frequency locks onto the external signal causing steps in the IV characteristics at fixed voltage. Apart from these steps, the critical current is also suppressed. The height of the steps and the critical current depends on the impedance of the radiation source

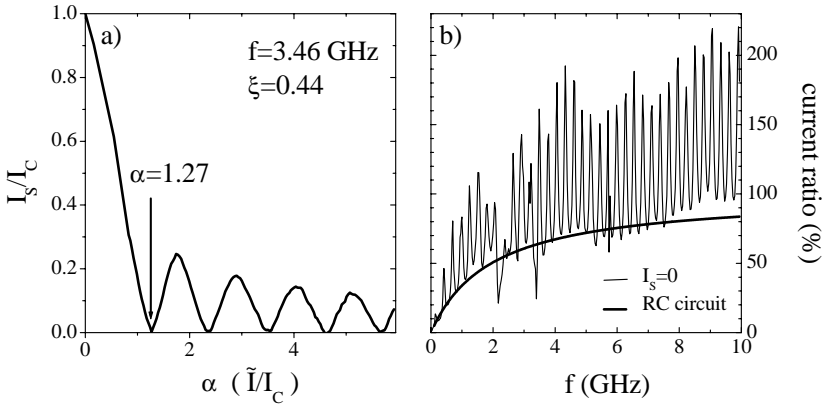


Figure 7.6: (a) The maximum supercurrent of the SQUID versus the applied radiation at $f=3.49$ GHz. The critical current was $2.4 \mu\text{A}$ and was completely suppressed at $\tilde{I}/I_C = 1.27$. (b) The ratio of the current through the SQUID, determined as in Fig. 7.6a, over the applied current as a function of the frequency. Clear resonances are spaced in frequency by 280 MHz.

and the magnitude of the applied radiation. For an ideal voltage bias of $\tilde{V} \cos \omega t$ over the junction, the height of the n th step is given by $I_C J_n(2e\tilde{V}/\hbar\omega)$, where J_n is the n th order Bessel function [4]. The resistance of our SQUID is much lower than the bias resistance $2(R_L + R_P)$, so we have to assume a rf-current bias of the form $\tilde{I} \cos \omega t$ where $\tilde{I} = \tilde{V}/2(R_L + R_P)$ and \tilde{V} is the magnitude of the signal when it arrives on-chip. The step height now has to be solved numerically, yielding Bessel-type functions.

To gauge the voltage that arrives at the SQUID, we recorded the magnitude of the radiation needed to suppress the critical current to zero. Figure 7.6a shows the measured supercurrent versus α , the applied rf-current normalized to I_C . The measured supercurrent is also normalized to I_C . The applied current \tilde{I} is calculated using the total attenuation mounted in the cabling, 20 dB at room temperature, 20 dB at 4 K, 3 dB at the mixing chamber and a frequency dependent cable loss, measured at room temperature. Figure 7.6a shows that the first zero of the supercurrent appears at $\alpha = 1.27$. The position of the first zero as found in simulations depends on the parameter $\xi = \hbar\omega/2eI_C R_T$, 0.44 for the depicted measurement. Theoretically the first zero for this ξ should lie at $\alpha = 1.6$, yielding a current ratio of 126%, suggesting the presence of a resonance in the system.

The current ratio was also calculated for measurements at other frequencies and is shown as the thin line in Figure 7.6b. One can clearly see resonance peaks with a spacing of 280 MHz. In vacuum this would correspond to $\lambda/2 = 54$ cm. Since the size of the copper can encasing the sample is of the order of 10 cm, the resonances do not occur in the sample cavity. Resonances could occur in the piece of coax between the mixing chamber and the sample, since the coax is not properly terminated by 50Ω , but by the sample with a resistance of 327Ω . Also, the attenuation at the mixing chamber was only 3 dB, too small to absorb all the reflections, causing the appearance of resonances. Because the dielectric constant of the insulator used in the coax cable was 2, $\lambda/2 = 38$ cm. Because this is exactly the length of the piece of coax cable mounted between the mixing chamber and the rf-probe, we conclude that the resonances occur in this piece of cabling.

Apart from the resonances, the transmission clearly decreases towards zero for decreasing frequencies. This is caused by the combination of the lead resistors (R_L and R_P) and DC-blocking capacitors C_P , forming a high-pass filter. The thick line shows a theoretical fit of the transmission of a RC-circuit to the data. As a fit parameter a capacitance of $C_P = 0.25$ pF is used in combination with the actual resistance values. This is much smaller than the designed value of ~ 0.1 nF. The cause of this problem might be in the fabrication of the parallel plate capacitor. Most probably there is a problem with the step coverage of the capacitor plates, effectively resulting in a small parasitic capacitance, in this case 0.25 pF, in series with the large parallel plate capacitors.

To test the pulse response of the SQUID, we measured the SQUID voltage for pulses with a varying length, height and repetition frequency f_r . The RCSJ model predicts that a voltage $f_r * \Phi_0$ will appear at the SQUID when $\int V_{P,SQ} dt \geq \Phi_0$. At these conditions, a single flux quantum will move through the SQUID per pulse. When $\int V_{P,SQ} dt \geq 2\Phi_0$ two flux quanta move through the SQUID per pulse and so on. For rectangular pulses, the SQUID voltage versus the pulse voltage at fixed length should show a staircase like behavior, just like the SQUID voltage versus the pulse length at fixed length. Figure 7.7a shows such a staircase for measurements with a pulse length of 300 ps and a repetition rate of 500 MHz. As expected, the staircase step height scales with the repetition rate as $f_r * \Phi_0$.

The steps appear at multiples of $50 \mu V$ and with a pulse length of 300 ps the integral $\int V_{P,SQ} dt$ is $7.3 \Phi_0$. This points to a strong attenuation and/or deformation of the pulse shape that arrives at the SQUID. The influence of the on-chip RC-circuit with the above estimate of C_P was simulated with a transient analysis in the software package MicroCap [6]. Simulations with a pulse shape as measured in Fig. 6.5b show that the pulse shape is strongly deformed by the

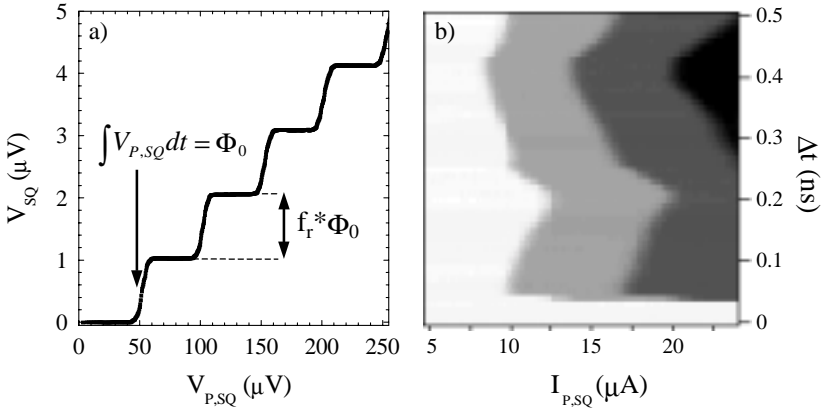


Figure 7.7: (a) Voltage over the SQUID in response to a pulse with a length of 300 ps and a varying pulse height. The pulse height $V_{P,SQ}$ at the SQUID was calculated with Eq. 6.5. The repetition frequency was 500 MHz, resulting in steps of height $f_r * \Phi_0 = 1.03 \mu\text{V}$. The SQUID was tuned at $I_C = 7 \mu\text{A}$ and biased at $4 \mu\text{A}$. (b) Voltage over the SQUID in grayscale as a function of the pulse height and the pulse length for $f_r = 1.4 \text{ GHz}$, $I_C = 7.2 \mu\text{A}$ and $I_{SQ} = 4.2 \mu\text{A}$. Black indicates $8.6 \mu\text{V}$, white indicates zero voltage.

RC-circuit. The effects on a variation of the pulse length are most dramatic. The RC-circuit formed by the blocking capacitors and the lead resistance has a very small time constant ($\sim 0.6 \text{ ns}$), acting as a differentiator for frequencies sufficiently lower than 0.6^{-1} GHz . In our case, the signal arriving at the SQUID looks like a positive bump located at the rising flank of the original pulse, and a negative bump at the falling flank. Changing the length of the original pulse merely changes the delay between these two bumps. Figure 7.7b shows the voltage over the SQUID versus the pulse length and the pulse height. Changing the pulse length indeed has little or an irregular effect on the voltage over the SQUID. Because the pulse shape was irregular and not constant over a period of time, it was not possible to turn the SQUID on and let it generate a fixed frequency. We also double checked this by applying a square wave to the SQUID, and looking at JQP gate traces of the CPB. Instead of showing PAT JQP peaks, broad shoulders appeared, indicating that the generated frequency was not constant, a prerequisite for doing coherence measurements on the CPB.

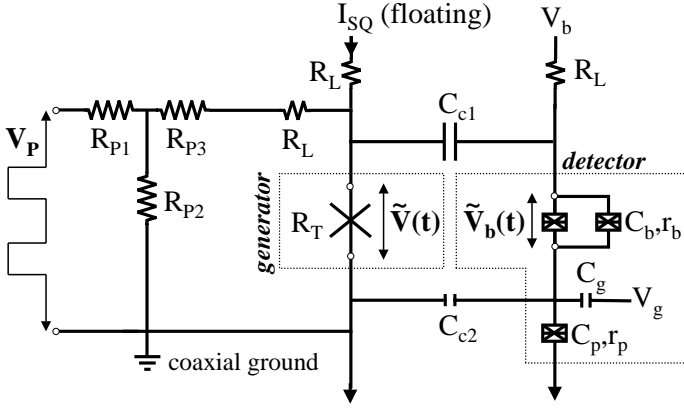


Figure 7.8: Schematic of the circuit with T-shaped voltage divider attached. The resistances R_{P1} , R_{P2} and R_{P3} can be chosen such that the impedance as seen from the coax cable is 50Ω . The bottom lead of the generator is connected to the coaxial ground, requiring a floating current source to avoid ground loops, but avoiding the use for DC-blocking capacitors.

7.4 Discussion

The decoherence time due to tunnelling of the first quasiparticle in the JQP cycle is $\Gamma_{p1}^{-1} = 400$ ps for sample 1. Because we aim at measuring Rabi-oscillations with an oscillation time of the order of nanoseconds, the resistance of the probe junction needs to be at least 10 M Ω . It is not possible to make CPB junctions and a probe junction with such asymmetric resistances with conventional two angle shadow evaporation. A more complicated three angle shadow evaporation process like used by Nakamura et al. [3] can resolve this problem. Another problem is the interference coupling into the CPB leads. To obtain a better current resolution, the shielding of the wiring of the dilution refrigerator needs to be improved.

The generator itself performs very well, but the design of the pulse circuitry has to be improved. To circumvent future problems with the DC-blocking capacitors and the cable resonances we propose the design shown in Fig. 7.8. The RC-circuit is replaced by a T-shaped voltage divider as is also used the rf-attenuators. The impedance as seen from the coax cable can be made 50Ω by carefully choosing the resistance values R_{P1} , R_{P2} and R_{P3} . If the series resistance of R_{P3} , R_L and R_T is called R_{P3}^* the requirement is $R_{P1} + R_{P2} // R_{P3}^* = 50 \Omega$. This will avoid the built up of resonances in the last piece of cable. The attenuation of the signal that arrives at the SQUID can also be chosen and is $\frac{R_T}{R_{P3}^*} \frac{R_{P2} // R_{P3}^*}{R_{P2} // R_{P3}^* + R_{P1}}$.

For example, with the parameters of sample 1 and $R_{P1} = 39 \Omega$, $R_{P2} = 13 \Omega$ and $R_{P3} = 30 \Omega$ one satisfies the 50Ω criterion and the total attenuation is $45\times$. Because the bottom lead of the SQUID is connected to the coaxial cable's ground, the current source has to be floating. A floating current source that is compatible with our dedicated measurement electronics has recently been developed.

7.5 Conclusions

We succeeded in fabricating an on-chip frequency generator with continuously tunable frequency and output voltage. The generator was fabricated in the form of a shunted overdamped SQUID. Because of the limitations of the detector, we were able to only test frequencies up to 20 GHz, but it has been proven before that the generator works up to frequencies of 200 GHz [1]. By carefully designing the coupling circuitry we estimated that 75% of the signal is coupled through to the detector. We also tested the cabling used for pulsing the SQUID, consisting of standard rf-cabling, a custom made rf-probe, on-chip rf-launchers and a on-chip RC-circuit. Resonances were detected in the last piece of cabling connecting the attenuator at the mixing chamber to the rf-probe. Also the DC-blocking capacitance was too small, probably due to a fabrication problem, resulting in a severe distortion of the pulse shape. Because the voltage over the SQUID during the pulse was not constant, we could not yet perform measurements of coherent quantum dynamics in the CPB. However, in the last paragraph, some crucial improvements were proposed, that are relatively easy to implement. In future experiments, this should make it possible to study the quantum coherent dynamics in a CPB with the use of an on-chip microwave generator.

References

- [1] E. Visscher, Ph.-D thesis, Delft University of Technology, 1996.
- [2] The step height of Shapiro steps scales linearly with I_C .
- [3] Y. Nakamura and J. S. Tsai, *Journ. of Sup.* **12**, 799 (1999)
- [4] S. Shapiro, *Phys. Rev. Lett.* **11**, 80 (1963)
- [5] P. Russer, *Jour. Appl Phys.* **43**, 2008 (1973)
- [6] See www.spectrum-soft.com

Summary

Single-charge transport in coupled nanostructures

This thesis is focussed on the development of strongly coupled single-charge devices. Single-charge devices are sub-micrometer sized electronic circuits that use the fact that charge is quantized. Their main component is the tunnel junction, a resistive element that can be made as small as one nanometer. In the past, many different circuits have been designed with the tunnel junction such as ultra-sensitive electrometers, logical gates and memory, where information is coded as the absence or presence of a single electron. To make more complex single-charge devices, a multi-layer technology is needed to couple the circuit elements. A special multi-layer technology was developed using heavily oxidized aluminum gates. In the first part of this thesis various different systems consisting of two coupled single-charge devices have been investigated.

In the first experiment, the islands of a Single-Electron Box (SEB) and a Single-Electron Transistor (SET) were coupled capacitively. Because of the strong coupling, the addition of one extra electron to the island of the SEB switched the SET from a conducting to an insulating state. The device thus acted as a switch that is activated by a single electron. In the second experiment, two SETs were fabricated in series with a common gate strongly coupled to both islands. Each island also had its own tuning gate, such that the conduction of the SETs could be tuned independently. This device acted as a logic inverter with voltage gain. The device could be tuned such that a low gate input resulted in a high output voltage, and a high output voltage resulted in a low output voltage. The gain, the ratio of the change in input voltage versus the change in output voltage, was measured versus temperature. The normal state gain decreased from 2.6 at base temperature to unity at 140 mK. In the superconducting state the gain stayed constant at 5.2 up to 250 mK. The vulnerability to thermal energy is a common problem of normal state single-electron devices. In the third experiment, the islands of two superconducting SETs were strongly coupled and their characteristics were measured in parallel. Because of the strong coupling, the first SET could be used to measure the charge distribution on the island of the second SET.

The measurements are the first to directly measure the charge distribution and are consistent with the orthodox theory of single-electron tunnelling. If the resistance of the second SSET was lowered to the quantum resistance, the total charge on the island is not quantized anymore and instead of charge one measures the potential distribution of the island. In the fourth experiment the quantum mechanical ground state was studied of a system of two coupled islands, connected to leads with superconducting Josephson junctions. The important charge carriers are now Cooper pairs instead of electrons, and it was shown that the separate islands are in a single combined ground state. Quantum mechanical fluctuations of the charge are coupled and the ground state is a superposition of different combinations of excess Cooper pairs on both islands.

In the second part of this thesis the design of a pulsed on-chip microwave generator and its coupling to a SEB has been described. The generator was fabricated in the form of a shunted SQUID. The circuitry that coupled the SQUID to the SEB was carefully designed to couple the maximum amount of signal and to avoid resonances in the coupling circuit. With a special sample holder and an attached rf-probe it was possible to turn the generator on and off on a nanosecond timescale. By measuring the photo-response of the SEB, it could be estimated that 75% of the generated signal was coupled to the SEB. This is much higher than has been achieved in similar experiments.

It can be concluded that the new multi-layer technique performs extremely well. The technique has been used to couple various single-charge devices, demonstrating the feasibility of even more complex single-charge devices.

Pieter Heij
Delft, July 2001.

Samenvatting

Enkel-ladingstransport in gekoppelde nanostructuren

Dit proefschrift is gefocust op de ontwikkeling van sterk gekoppelde enkel-ladings devices. Enkel-ladings devices zijn sub-micrometer elektronische circuits, die het effect benutten dat lading gequantiseerd is. De hoofdcomponent is de tunneljunctie, een element met elektrische weerstand, die enkele nanometers klein gemaakt kan worden. In het verleden zijn vele verschillende circuits ontworpen met de tunneljunctie zoals een supergevoelige ladingsmeter, logische poorten en geheugen, waar de aan- of afwezigheid van een enkel elektron de informatie codeert. Om complexere enkel-ladings devices te maken is een speciale meerlaagstechniek nodig, die verschillende circuitelementen koppelt. Een speciale meerlaagstechniek is ontwikkeld die gebruik maakt van zwaar geoxideerde aluminium regelcapaciteiten. In het eerste deel van dit proefschrift zijn verschillende systemen onderzocht die bestaan uit twee gekoppelde enkel-ladings devices.

In het eerste experiment werden de eilanden van een Enkel-Elektron Box (EEB) en een Enkel-Elektron Transistor (EET) capacitief aan elkaar gekoppeld. Vanwege de sterke koppeling schakelde de toevoeging van één extra elektron op het eiland van de EEB de EET van een geleidende naar een niet-geleidende toestand. Het device werkte dus als een schakelaar die geactiveerd wordt door een enkel elektron. In het tweede experiment waren twee EETs in serie gefabriceerd met een gezamenlijke invoercapaciteit gekoppeld aan beide eilanden. Elk eiland had een aparte afstemcapaciteit zodat de geleiding van beide EETs onafhankelijk geregeld kon worden. Dit device werkte als een logische inverter met spanningsversterking. De inverter kon zo afgeregeld worden dat een lage ingangsspanning resulteerde in een hoge uitgangsspanning en een hoge ingangsspanning in een lage uitgangsspanning. De versterking, de ratio van de verandering van de ingangsspanning over de verandering van uitgangsspanning, werd gemeten als functie van de temperatuur. De versterking in de normale toestand ging omlaag van 2.6 bij de laagste temperaturen tot één bij 140 mK. In de supergeleidende toestand bleef de versterking constant 5.2 tot 250 mK. De kwetsbaarheid voor thermische energie is een algemeen probleem van enkel-ladings devices in de nor-

male toestand. In het derde experiment werden de eilanden van twee EETs sterk gekoppeld terwijl hun karakteristieken parallel werden gemeten. Vanwege de sterke koppeling kon de eerste EET gebruikt worden om de ladingsverdeling op het eiland van de tweede EET te meten. De metingen zijn de eerste die direct de ladingsverdeling kunnen meten en zijn consistent met de orthodoxe theorie van enkel-elektron tunnelen. Toen de weerstand van de tweede EET verlaagd werd tot de quantumweerstand, was lading niet meer gequantiseerd en in plaats van lading werd de potentiaal verdeling van het eiland gemeten. In het vierde experiment werd de quantummechanische grondtoestand bestudeerd van een systeem van twee gekoppelde eilanden, die verbonden waren aan de toevoerdraden met supergeleidende Josephson juncties. De ladingsdragers zijn nu Cooperparen in plaats van elektronen en er werd gedemonstreerd dat de afzonderlijke eilanden in een gezamenlijke grondtoestand zitten. Quantummechanische fluctuaties van de lading zijn gekoppeld en de grondtoestand was een superpositie van verschillende combinaties van extra Cooperparen op beide eilanden.

In het tweede deel van dit proefschrift wordt het ontwerp van een gepulste on-chip microgolfgenerator en de koppeling naar een EEB besproken. De generator werd gefabriceerd in de vorm van een geshuntte SQUID. Het circuit dat de generator koppelde aan de SEB is zorgvuldig ontworpen om de maximale hoeveelheid straling door te koppelen en om resonanties te vermijden in het circuit. Met een speciale houder waarop een microgolf probe werd aangesloten was het mogelijk om de generator op nanoseconde tijdschalen aan en uit te schakelen. Door de fotorespons van de EEB te meten kon geschat worden dat 75% van het gegenereerde signaal werd doorgekoppeld aan de EEB. Dit is veel meer dan in vergelijkbare experimenten.

Er kan geconcludeerd worden dat de nieuwe meerlaagstechniek uitstekend werkt. De techniek werd gebruikt om verschillende enkel-ladings devices aan elkaar te koppelen, en laat zien dat de fabricage van nog complexere schakelingen mogelijk is.

Pieter Heij
Delft, juli 2001.

Curriculum Vitae

Cornelis Pieter Heij

- 2 May 1973 Born in Amsterdam, The Netherlands.
- 1985-1991 Gymnasium β at 'Het Vossius Gymnasium' in Amsterdam.
- 1991-1997 M.Sc. Applied Physics at the Delft University of Technology. Graduate research in the Quantum Transport group of Prof. dr. ir. J. E. Mooij. Subject: Electrical transport in thin films of the charge-density-wave compound $\text{Rb}_{0.30}\text{MoO}_3$.
- 1997 Visiting researcher at the Massachusetts Institute of Technology, Cambridge, USA.
- 1997-2001 Ph.D research at the Delft University of Technology in the Quantum Transport group of Prof. dr. ir. J.E. Mooij. Subject: Single-Charge Transport in Coupled Nanostructures.
- 2002- Fellow at McKinsey & Company

List of publications

1. *Charge spectroscopy with a strongly coupled single-electron transistor*,
C. P. Heij, P. Hadley, and J. E. Mooij, accepted for publication in Phys. Rev. B.
2. *Single-Electron Effects in Metals and Nanotubes for Nanoscale Circuits*,
P. Hadley, C. P. Heij, G. Lientschnig, T. Teepen, H. Postma, and C. Dekker,
Proceedings of the MIOP 2001.
3. *Single-electron inverter*,
C.P. Heij, P.Hadley, and J.E. Mooij, Applied Physics Letters **78**, 1140 (2001).
4. *Enhancement of Josephson quasiparticle current in coupled superconducting single-electron transistors*,
D.C. Dixon, C.P. Heij, P. Hadley, and J.E. Mooij, Journal of Low Temperature Physics **118**, 325 (2000).
5. *Negative differential resistance due to single-electron switching*,
C.P. Heij, D.C. Dixon, P. Hadley, and J.E. Mooij, Applied Physics Letters **74**, 1042 (1999).
6. *Interactions of topological kinks in two coupled rings of non-linear oscillators*,
A.E. Duwel, C.P. Heij, J.C. Weisenfeld, M.K.S. Yeung, E. Trias, S.J.K. Vardy,
H.S.J. van der Zant, S.H. Strogatz, and T.P. Orlando, Physical Review B **13**, 8749 (1998).
7. *Photolithographic patterning of the charge-density-wave conductor $Rb_{0.30}MoO_3$* ,
H.S.J. van der Zant, O.C. Mantel, C.P. Heij, and C. Dekker, Synthetic Metals **86**, 1781 (1997).

